

Naturally Derived Biocompatible Photoinitiators for 3D Printing

Di Zhu

January 2024

A thesis submitted for the degree of Doctor of Philosophy of
The Australian National University.



© Copyright by Di Zhu 2024

All Rights Reserved

Author's declaration

I declare that this thesis contains no material which has been accepted for the award of any other degree or diploma in any university. All results are obtained during my Ph.D. program in Research School of Chemistry at the Australian National University from 2018 to 2023.

To the best of my knowledge, it contains no material previously published or written by another person, except where due reference is made in the text.

Di Zhu

January 2024

Acknowledgements

The completion of the Ph.D. program is not the end of life, but only a new start of the next stage. During the program, my mind was reshaped in a scientific context, which allowed me to run faster towards the next goal in the future. Meanwhile, I also made a lifelong friend and understood myself more than I thought.

I am exceedingly appreciative of my primary supervisor, Professor Pu Xiao first. He gave me absolute 100% support for my health and research from beginning to end. Throughout my Ph.D. program, Pu has guided me into this attractive field with his professional and scientific background. He encouraged me to broaden my research interest. Therefore, he also offered support to conferences. Lectures at conferences delivered plenty of fresh points of view and inspiration.

I also feel grateful to a few individual professionals, Professor Michelle Coote, Professor Mark Humphery, and Professor Yun Liu. They are my supervisory panel members. At critical milestones, they provided suggestive comments, thus improving my research and keeping my progress on track.

I am deeply grateful to everyone who has supported me during my academic journey. They have guided me, encouraged me, and unconditionally believed in my abilities, so I am grateful for their unwavering support.

A special thanks to my family and friends. They always offer me unconditional support for either science or life.

Abstract

Photopolymerization is a technology that fulfills the requirements of instant production, especially when meeting medical emergencies. Recently, considerable biocompatible materials (e.g., poly(ethylene glycol), cellulose, etc.) have been involved in photopolymerization-based manufacturing. To achieve this, photoinitiator is a crucial component. Commercial photoinitiators, however, are synthetic and eco-unfriendly, causing potential health concerns due to their migration effect. Therefore, natural photoinitiators have drawn tremendous research interest due to their known bioactivities and nature-derived origin. In this regard, this thesis mainly concentrates on 1) the development of naturally occurring photoinitiators demonstrating excellent photoinitiation abilities, 2) the formulation of the investigated photoinitiators involved conventional commercial resins (i.e., dental resin and epoxy) or 3D resins for shape memory hydrogels. In the present thesis, four natural plant extracts are investigated as photoinitiator candidates, extracted from berries, citrus, pomegranate, and Indigofera, respectively. Moreover, the innovative designed functional materials have been successfully 3D printed.

Before the discussion of the aforementioned four photoinitiator candidates, Chapter 1 introduces the recent naturally derived photoinitiators applied to medical applications (e.g., regenerative medicines, antibacterial coatings, dental restoration, etc.). Specifically, riboflavin, hyaluronan-modified commercial photoinitiators, carbazole derivatives, anthraquinone derivatives, β -Carotene, cyclic acetals, chalcone derivatives, and an indigo derivative are enclosed in this chapter. Among the mentioned photoinitiators, carbazole derivatives, anthraquinone derivatives are big families of efficient photoinitiators, and their structural effect on photoinitiation ability has been also discussed.

Chapter 2 investigates berries-extracted flavones, morin and quercetin, as photoinitiators for free radical, cationic, and thiol-ene polymerizations. Both morin and quercetin exhibit visible light sensitivity and demonstrate their photoinitiation abilities under the irradiation of visible light. However, their photoinitiation ability differences are observed in all kinds of photopolymerizations. Specifically, morin exhibits no photoinitiation ability in all but cationic polymerization of a vinyl, tri(ethylene glycol) divinyl ether (DVE-3). In contrast, quercetin demonstrates its versatile photoinitiation ability in all the mentioned photopolymerization categories. Its versatility enhances its involvement frequency in photocurable resin formulations.

Chapter 3 introduces citrus-extracted naringin as a water-soluble natural photoinitiator. Naringin demonstrates its excellent visible light absorption in alkali environments and rapid photoreaction with the addition of a coinitiator upon exposure to visible light. Subsequently, a high-fidelity 3D printing is achieved. Meanwhile, the degree of alkalinity manipulates the

degree of crosslinking, reflected by the mesh sizes of the resultant polymer, and the mesh size influences the water uptake, thus determining the degree of shape transformation. Moreover, an additional monomer, sodium acrylate is introduced to endow the resulting materials with electro-active behavior. Crosslinked with sodium acrylate, the 3D-printed designed objects can transform their shape in the indicated direction in an applied electric field. In recent decades, few natural photoinitiator has been developed as a water-soluble photoinitiator. Considering the lack of natural water-soluble photoinitiators, the development of naringin offers an environmentally friendly option for light-based 3D printing of waterborne materials.

Chapter 4 demonstrates a pomegranate-extracted ellagic acid as a water-soluble photoinitiator. Ellagic acid exhibits its light absorption in violet-cyan light range in alkali environments. Even though this finding is similar to the one of naringin, in identical conditions, ellagic acid can reach its best photoinitiation ability with less amount in photocurable resins. Furthermore, the water content is determined in terms of sufficient shear elasticity, ensuring successful bottom-up 3D printing without deficiency. With the optimized formula, a 3D-printed figurine with obvious facial texture is obtained. In addition, with the help of a bilayer multi-material motif, a programmed water-driven actuator can play a role in a smart switch. The developed ellagic acid-based photocurable formula can therefore be used in the protection of water-sensitive devices in an environmentally friendly manner.

Chapter 5 focuses on *Indigofera* extract, indigo carmine. Indigo carmine exhibits its light sensitivity and photoinitiation ability to violet-green light. This is the only organic salt natural compound among the ones mentioned in the present thesis. Because it's a sodium salt, the excessive introduction of NaOH decelerates the photoinitiation ability of indigo carmine due to the common-ion effect inducing reduced water solubility of indigo carmine. After we further screen the chain length of PEGDA and water content, the optimized formula is developed, and a complex surface structure is successfully 3D printed. A water-driven shape memory polymer is thereafter fabricated and exhibits reversible shape transformation in the presence and the absence of aqueous NaCl solution. In addition, the optimized formula also affords the indigo carmine with sufficient photoinitiation abilities under irradiation of both violet and green LEDs. The wide spectrum of its light sensitivity endows indigo carmine with expanded applications in safer scenarios under long-wavelength irradiations, considering the healthy concerns of (near) UV irradiation.

Table of Contents

Author's declaration.....	iii
Acknowledgements.....	v
Abstract.....	vii
Table of Contents.....	ix
List of Tables.....	xiii
List of Figures.....	xv
Chapter 1 Literature Review.....	1
1.1 Abstract.....	1
1.2 Introduction.....	1
1.3 Photoinitiators for regenerative medicines.....	3
1.3.1 Regenerative medicines photoinitiated by hyaluronan-modified derivatives....	4
1.3.2 Regenerative medicines photoinitiated by riboflavin.....	6
1.3.3 Regenerative medicines photoinitiated by carbazole Derivatives.....	11
1.4 Photoinitiators for Antibacterial or Antifouling Coatings.....	15
1.4.1 Anthraquinone derivatives.....	17
1.4.2 β -Carotene.....	27
1.5 Photoinitiators/coinitiators for Dental Restoration.....	28
1.5.1 Cyclic acetals as coinitiators.....	29
1.5.2 Substituent effect on photoinitiation ability.....	31
1.6 Photoinitiator Candidates for Other Medical Applications.....	32
1.6.1 Microneedle initiated by riboflavin.....	33
1.6.2 Shape memory polymers initiated by chalcone derivatives and an indigo derivative.....	35
1.7 Conclusion and current challenges.....	38
1.8 Objectives and thesis outline.....	39
1.9 References:.....	40
Chapter 2 Flavones: natural photoinitiators extracted from berries.....	49
2.1 Preface.....	49
2.2 Statement of contribution.....	50
2.3 Publication status.....	50
2.4 Abstract.....	50
2.5 Introduction.....	50
2.6 Experimental.....	51

2.6.1	Materials.....	51
2.6.2	Irradiation Sources	52
2.6.3	Steady-State Photolysis	52
2.6.4	Electron Paramagnetic Resonance Spin Trapping	52
2.6.5	Photopolymerization Experiments.....	53
2.7	Results and Discussion.....	53
2.7.1	Light Absorption Properties of Morin and Quercetin	53
2.7.2	Photochemistry of Morin and Quercetin	54
2.7.3	Photopolymerization Kinetics in the Presence of Morin- and Quercetin-Based PISs under Blue LEDs	56
2.8	Conclusion	60
2.9	References:	60
2.10	Supporting Information	64
Chapter 3 Naringin: a naturally occurring flavonoid as a photoinitiator for 3D printed electro-active actuator.....		
3.1	Preface.....	67
3.2	Abstract.....	67
3.3	Introduction.....	68
3.4	Experimental.....	70
3.4.1	Materials.....	70
3.4.2	Steady-state photolysis	70
3.4.3	Electron Paramagnetic Resonance Spin Trapping (EPR-ST).....	71
3.4.4	Photopolymerization kinetics	71
3.4.5	Crosslinking network characteristics.....	71
3.4.6	Photorheology.....	72
3.4.7	Three-point bending tests.....	72
3.4.8	3D printing.....	72
3.4.9	Electro-mechanical actuation	72
3.5	Results and discussion	73
3.5.1	Photophysical and photochemical characterization of naringin	73
3.5.2	Photoinitiation ability of naringin in alkane formulas	75
3.5.3	Development of naringin-based photoinitiating system for 3D printing of electro-active actuator	77
3.5.4	3D-printed actuator.....	79
3.6	Conclusion	82
3.7	References:	83

3.8	Supporting Information	86
Chapter 4	Ellagic acid: a natural photoinitiator extracted from pomegranate for the 3D printing application of smart switch	93
4.1	Preface	93
4.2	Abstract.....	93
4.3	Introduction	94
4.4	Experimental.....	96
4.4.1	Materials.....	96
4.4.2	Light absorption and steady-state photolysis	96
4.4.3	Electron paramagnetic resonance spin trapping (EPR-ST) technique	97
4.4.4	Photopolymerization kinetics	97
4.4.5	Swelling kinetics	97
4.4.6	Photorheology.....	98
4.4.7	Three-point bending tests.....	98
4.4.8	3D printing.....	98
4.5	Results and Discussion.....	98
4.5.1	Photophysical properties and photochemical reactions	98
4.5.2	Photoinitiation ability of ellagic acid and the potential for 3D printing	100
4.5.3	Development of a smart switch	104
4.6	Conclusion	108
4.7	References:	108
4.8	Supporting Information	111
Chapter 5	Indigo carmine: a natural photoinitiator extracted from Indigofera for the 3D printing application of shape memory hydrogel.....	113
5.1	Preface.....	113
5.2	Author contributions to the published article.....	113
5.3	Publication status	113
5.4	Abstract.....	114
5.5	Introduction	114
5.6	Experimental.....	116
5.6.1	Materials.....	116
5.6.2	Irradiation sources	117
5.6.3	Steady-state photolysis	117
5.6.4	Electron Paramagnetic Resonance Spin Trapping (EPR-ST).....	117
5.6.5	Photopolymerization kinetics	117

5.6.6	Photorheology.....	118
5.6.7	3D printing.....	118
5.7	Results and discussion	118
5.7.1	Light absorption properties of IDGCM	118
5.7.2	The effect of the amount of NaOH, PEGDA, and IDGCM in formulation on photopolymerization of PEGDA	120
5.7.3	The effect of chain length of PEGDA, LED and electrolyte on photopolymerization of PEGDA	122
5.7.4	3D Printing.....	124
5.8	Conclusion and outlook	126
5.9	References	127
5.10	Supporting Information	132
	Conclusions.....	139

List of Tables

Table 1.1. The biocompatibility indicators comparison of collagen-treated and collagen-untreated scaffold fabricated by riboflavin-induced 3D printing. ^{49, 50}	10
Table 1.2. The binding interaction parameters and photophysical properties of CBZ1 and CBZ2. ^{51, 52}	12
Table 1.3. The photophysical properties of CBZs and the final functional group conversions of TMPAT or EPOX in the presence of CBZ/Iod (0.5%/1%, wt). Adapted with permission from ^{71, 72} . Copyrights 2017 American Chemical Society.	15
Table 1.4. The composition of prepolymers for the fabrication of antibacterial coatings. ⁸⁶⁻⁸⁸	17
Table 1.5. The irradiation sources for the investigated AQDs. ^{30-32, 91-95}	20
Table 1.6. Final conversions of Bis-GMA/TEGDMA (70%/30%, wt), EPOX, and DVE-3 in the presence of AQD-OH-based photoinitiating systems upon exposure to LED@455 nm and/or LED@518 nm. (AQD-OH: 0.5 wt %; TEAOH, R-Br, or Iod1: 2 wt %; NVK: 3 wt %) ^{32, 95}	21
Table 1.7. Final conversions of (a) EPOX and DVE-3, (b) TPGDA, (c) TMPTA, and (d) EB605 in the presence of AQD-NH ₂ -based photoinitiating systems upon exposure to LED@455 nm and LED@518 nm. (AQD-NH ₂ : 0.5 wt %; TEAOH, R-Br, or Iod1: 2 wt %; NVK: 3 wt %) ^{30, 31}	25
Table 1.8. The composition of dental restorative formulas and their corresponding light intensity, double bond conversions, and maximum rates of photopolymerization of Bis-GMA/TEGDMA (70%/30%, wt). ¹¹¹⁻¹¹⁴	30
Table 2.1. Light absorption properties of morin and quercetin in ethanol: maximum absorption wavelengths λ_{max} , extinction coefficients at λ_{max} and at the maximum emission wavelengths of the different LED bulbs.	54
Table 2.2. Photopolymerization rates and double bond conversions of photopolymerization of Bis-GMA/TEGDMA blend (70%/30%, w/w) in the presence of quercetin-based PISs (quercetin: 0.5 wt%; Iod: 2 wt%; NPG: 2 wt%) upon exposure to the LED@410 nm (110 mW cm ⁻²) or the LED@445 nm (80 mW cm ⁻²) for 300 s.	57
Table 5.1. The extinction coefficients of IDGCM in neutral and alkaline solution at their absorption maxim, 410 nm, and 530 nm.	119
Table 5.2. Gel points of the photopolymerization of the blend of PEGDA 700/water (80%/20%, wt) at diverse thicknesses in the presence of IDGCM/Iod (0.5%/2%, wt) upon the exposure of LED@410 nm (110 mW cm ⁻²) and LED@530 nm (25 mW cm ⁻²). (25 mM NaOH)	123
Table 5.3. Gel points of the photopolymerization of the blend of PEGDA 700/water (80%/20%, wt) with 25 mM NaCl or 25 mM NaOH at diverse thicknesses in the presence of IDGCM/Iod (0.5%/2%, wt) upon the exposure of LED@410 nm (110 mW cm ⁻²).	124
Table S3.1. Light absorption properties of naringin in diverse [NaOH] _{aq} : maximum absorption wavelengths λ_{max} , extinction coefficients at λ_{max} and at the maximum emission wavelengths of the investigated LED@400 nm.	87
Table S3.2. The stability of developed formulations in the presence of diverse naringin concentrations. (Iod: 2 wt%; PEGDA/DI water: 8/2, w/w; [NaOH] = 100 mM)	89
Table S3.3. The stability of developed formulations in the presence of diverse PEGDA 700/DI water ratios. (Naringin: 0.5 wt%; Iod: 2 wt%; [NaOH] = 100 mM).....	90

Table S3.4. The stability of developed formulations in the presence of diverse sodium acrylate concentrations. (Naringin: 0.5 wt%; Iod: 2 wt%; [NaOH] = 100 mM)	90
Table S5.1. Summary of sample composition for 3D printing.....	137
Table S5.2. Cat coin (39 × 39 × 2 mm, L × W × H) print cured using the PEGDA 700/water (80%/20%, wt) in the presence of IDGCM/Iod (0.5%/2%, wt) and 25 mM NaOH under diverse settings.....	138

List of Figures

Figure 1.1. (A). a)3D model of a yin-yang structure and the cell-laden two-photon printed yin-yang structure after b) 24 hours and c) 5 days photoinitiated by HA-PI1; ⁴⁸ (B) In vivo degradation of HA-PI2 implanted in TA muscles for 2-8 days. ⁴⁷ Adapted with permission from ^{47, 48} . Copyright 2011 FASEB and Copyright 2017 The Royal Society of Chemistry used under a Creative Commons Attribution 3.0 Unported License.	6
Figure 1.2. Scheme of (a) the formation of MeGC hydrogel and (b) the 3D printing of MeGC hydrogel scaffolds. Reproduced with permission from ⁴⁹ . Copyright 2022 Elsevier Ltd.....	8
Figure 1.3. (a-d) SEM images of two-photon microfabricated structures in (a, c) top view and (b, d) side view, and (e-h) confocal fluorescence images of (e, g) hydrogel scaffold and (f, h) cell-laden hydrogel scaffold; (a-b, e-f) CBZ1/CB7 complex or (c-d, g-h) CBZ2/CB7 complex as two-photon photoinitiators. Adapted with permissions from ^{51, 52} . Copyright 2019 American Chemical Society and Copyright 2021 American Chemical Society.....	12
Figure 1.4. The reduction rate of bacterial count on the coatings fabricated by AQD1, AQD2, and β -carotene under irradiations. ⁸⁶⁻⁸⁸	19
Figure 1.5. Final conversions of (a) EPOX and Bis-GMA/TEGDMA (70%/30%, wt) in the presence of AQD-NH2-based photoinitiating systems and (b) EPOX DVE-3, TMPTA and Bis-GMA/TEGDMA (70%/30%, wt) in the presence of AQD-NH2-8-based photoinitiating systems upon exposure to LED@636 nm; (c) EPOX and Bis-GMA/TEGDMA (70%/30%, wt) in the presence of AQD-NH2-8/Iod1/NVK under irradiation from UV to IR bulb. (AQD-NH2: 0.5 wt %; Iod1: 2 wt %; NVK: 3 wt %) ⁹⁴ . 27	27
Figure 1.6. The synthesis of antibacterial coatings via photopolymerization of epoxy limonene and eugenol in the presence of a β -carotene-based photoinitiating system and the structure of interpenetrating polymer network. Adapted with permission from ⁸⁸ . Copyright 2019 American Chemical Society.....	28
Figure 1.7. Photographs of (A) the fabricated microneedle patch via 3D printing of silk fibroin in the presence of riboflavin, and swine skin (B) before and (C) after penetration, and (D) fluorescence of rhodamine B in the swine skin under UV illumination. Reproduced with permission from ¹²⁸ . Copyright 2020 The Korean Society of Industrial and Engineering Chemistry.	35
Figure 1.8. (A-B)Cross-shape structure (1) mold and (2-6) shape memory behavior upon stimuli: (2) after 1-min photopolymerization, (3) after 1-min immersion into water, (4) after 1-min dehydration at 100 °C, (5) after 10-min dehydration at 100 °C, and (6) after 10-min exposure to open air under ambient condition; cross-shape structure fabricated using (A) chalcone 1/Iod (1.5%/1.5%, wt) and (B) chalcone 2/Iod/EDB (1.5%/1.5%/1.5%, wt). (C) The (a) design and (b) the shape memory behavior of the 3D printed seashell structure upon hydration and dehydration under ambient conditions. Adapted with permission from ¹³⁷⁻¹³⁹ . Copyright 2020 The Royal Society of Chemistry, Copyright 2021 The Royal Society of Chemistry and the Chinese Chemical Society, and Copyright 2022 Elsevier B.V.	37
Figure 2.1. UV-vis absorption spectra of morin and quercetin in ethanol.	54
Figure 2.2. Steady state photolysis of (a) morin/Iod and (b) quercetin/Iod in ethanol ([Iod] = 8 mM); UV-vis spectra recorded at different irradiation time; UV LED at 394 nm irradiation (4 mW·cm ⁻²).	55

Figure 2.3. EPR spectra of the radicals generated in quercetin/Iod combination upon LED@374 nm exposure and trapped by PBN in *tert*-butylbenzene: (a) experimental and (b) simulated spectra. PBN/phenyl radical adducts formed in quercetin/Iod system: $a_N = 14.3$ G, $a_H = 2.2$ G., reference values in refs.^{41, 42} 55

Figure 2.4. Photopolymerization profiles (double bond conversions vs time) of Bis-GMA/TEGDMA blend (70%/30%, w/w) in laminate in the presence of NPG- and quercetin-based PISs (quercetin: 0.5 wt%; NPG: 2 wt%; Iod: 2 wt%) upon exposure to (a) LED@410 nm (110 mW cm⁻²) and (b) LED@445 nm (80 mW cm⁻²)..... 57

Figure 2.5. Photopolymerization profiles (double bond conversions vs time) of TMPTA in laminate in the presence of NPG- and quercetin-based PISs (quercetin-based PIS: quercetin: 0.5 wt%, NPG: 2 wt%, Iod: 2 wt%; NPG-based PISs: NPG: 0.5 wt% or 2 wt%, Iod: 2 wt%) upon exposure to (a) LED@410 nm (110 mW cm⁻²) and (b) LED@445 nm (80 mW cm⁻²)..... 58

Figure 2.6. Cationic photopolymerization profiles (double-bond conversions vs time) of DVE-3 in laminate in the presence of morin- and quercetin-based PISs (quercetin or morin: 0.5 wt%; Iod: 2 wt%) upon exposure to LED@410 nm..... 59

Figure 2.7. Thiol-ene photopolymerization profiles (a) (double-bond conversions vs time) of DVE-3 and (thiol bond conversions vs time) of TriThiol and (b) (double-bond conversions vs time) of Trione and (thiol bond conversions vs time) of TriThiol in the presence of PIS quercetin/Iod (0.5%/2%, wt) in laminate upon exposure to LED@410 nm. (Double-bond conversions: black curves; thiol bond conversions: red curves; ene:thiol = 1:1)..... 60

Figure 3.1. The UV-vis absorption of naringin in the aqueous media at diverse [NaOH]. 74

Figure 3.2. The interaction between naringin and Iod: (a) the steady-state photolysis of naringin/Iod in aq. NaOH upon exposure to LED@400 nm; UV-vis spectra were recorded at different irradiation time. ([NaOH] = 100 mM; [Iod] = 4.4 mM) and (b) EPR spectra of the radicals generated in naringin/Iod combination upon exposure to LED@400 nm and trapped by PBN in *tert*-butylbenzene: PBN/phenyl radical adducts formed in naringin/Iod system: $a_N = 14.3$ G, $a_H = 2.2$ G.⁵⁸ 74

Figure 3.3. (a) Photopolymerization profiles (double bond conversions vs time) of PEGDA/DI water (8/2, w/w) in laminate in the presence of naringin/Iod (0.5%/2%, wt) with diverse [NaOH] upon the exposure to LED@400 nm (6.4 mW cm⁻²) and (b) mesh sizes of the corresponding polymerized hydrogels.⁴⁶⁻⁵⁰ 76

Figure 3.4. Photopolymerization profiles (double bond conversions vs time) of (a) PEGDA/DI water (8/2, w/w) blend in the presence of naringin/2 wt% Iod, (b) PEGDA/DI water in the presence of naringin/Iod (0.5%/2%, wt), and (c) PEGDA/DI water in the presence of naringin/Iod (0.5%/2%, wt) and sodium acrylate, with 100 mM NaOH in laminate upon exposure to the LED@400 nm (6.4 mW cm⁻²). 78

Figure 3.5. The front view of the STL model file and the Groot 3D printed using the PEGDA/DI water (8/2, w/w) in the presence of naringin/Iod (0.5%/2%, wt) and 100 mM NaOH. (40 × 23 × 33 mm, L × W × H; layered exposure time: 10 s)..... 79

Figure 3.6. The actuation distance (distance vs time) of the electro-stimulated strips fabricated by (a) PEGDA/DI water (8/2, w/w) (red) and PEGDA/DI water (4/6, w/w) in the presence of 4 wt% sodium acrylate (blue), with 100 mM NaOH in an electric field (30 V) and (b) PEGDA/DI water (4/6, w/w) in the presence of 4 wt% sodium acrylate with 100 mM NaOH at set and reverse directions of the electric field..... 80

Figure 3.7. 3D printed electro-activated (a) hand-like actuators: (a1) before and (a2) after electro-stimulation; and (b) hook (PEGDA/DI water (6/4, w/w) in the presence of

2 wt% sodium acrylate with 100 mM NaOH): (b1) before, (b2) after electro-stimulation in an electric field (voltage = 30 V), and their loading of (b3) 2.2 g and (b4) 6.6 g... 82

Figure 4.1. (a) UV-vis absorption profiles of ellagic acid in aq. NaOH; (b) O.D. decreases of ellagic acid/Iod (Δ O.D. vs time) at 355 nm in 1 mM aq. NaOH; at 420 nm in 10 mM aq. NaOH; at 425 nm in 100 mM and 500 mM aq. NaOH under irradiation of LED@400 nm; and (c) EPR-ST spectra of the radicals generated in ellagic acid/Iod combination upon exposure to LED@400 nm and trapped by PBN in tert-butylbenzene: PBN/phenyl radical adducts formed in ellagic acid/Iod system: $a_N = 14.3$ G, $a_H = 2.2$ G.⁵³ 100

Figure 4.2. (a) Photopolymerization profiles (double bond conversions vs time) of PEGDA 700/water (8/2, w/w) and (b) their maximum rates in laminate in the presence of different concentrations of ellagic acid, 2 wt% Iod, and 100 mM NaOH upon exposure to LED@400 nm (6.4 mW cm⁻²)..... 101

Figure 4.3. (a) Photopolymerization profiles of (double bond conversions vs time) of PEGDA 700/water in diverse ratios and (b) the corresponding in-situ photorheological profiles in the presence of ellagic acid/Iod (0.3%/2%, wt) and 100 mM NaOH upon exposure to LED@400 nm (6.4 mW cm⁻²)..... 103

Figure 4.4. The 3D printed Gandalf figurine using the PEGDA 700/water (8/1, w/w) in the presence of ellagic acid/Iod (0.3%/2%, wt) and 100 mM NaOH. (9 × 10 × 13 mm, L × W × H; layered exposure time: 10 s)..... 104

Figure 4.5. (a) Simulated smart hydrogel; (b) swelling kinetics (swelling uptake vs time) of the resultant polymers of PEGDA/water (8/1, w/w) blends in the presence of ellagic acid/Iod (0.3%/2%, wt) and 100 mM NaOH upon exposure to the LED@400 nm (6.4 mW cm⁻²); and (c) the proposed process of 3D printing. 105

Figure 4.6. (a) In situ photorheology profiles (storage moduli (G') vs time) of PEGDA/water (8/1, w/w) in laminate in the presence of ellagic acid/Iod (0.3%/2%, wt) and 100 mM NaOH upon exposure to the LED@400 nm (6.4 mW cm⁻²) and (b) three-point bending tests (force vs centered displacement) of the corresponding resultant polymers. 106

Figure 4.7. (A) The water-driven self-folding assembly process of 3D printed leaves (a) before and (b) after immersion in deionized water for 5 min at ambient temperature at its (1) front and (2) back views; (B) 3D printed water-sensitive smart switch (a) before and (b) after stimulated by deionized water. 107

Figure 5.1. UV-vis absorption of IDGCM in water (black), 25 mM aq. NaCl (red), and 25 mM aq. NaOH (blue). 119

Figure 5.2. EPR spectra of the radicals generated in IDGCM/Iod combination upon exposure to LED@410 nm and trapped by PBN in the aqueous solution of 25 mM NaOH: PBN/phenyl radical adducts formed in IDGCM/Iod system: $a_N = 16$ G, $a_H = 4.23$ G.⁷⁵ 120

Figure 5.3. Photopolymerization profiles (double bond conversions vs time) of PEGDA 700/water (80%/20%, w/w) in laminate in the presence of IDGCM/Iod (0.5%/2%, wt) with 1.25 mM – 50 mM NaOH upon exposure to the LED@410 nm (110 mW cm⁻²). 121

Figure 5.4. Photopolymerization profiles (double bond conversions vs time) of diverse PEGDA/water (80%/20%, wt) in laminate in the presence of IDGCM/Iod (0.5%/2%, wt) upon exposure to the LED@410 nm (110 mW cm⁻²). (NaOH: 25 mM)..... 122

Figure 5.5. The top view of STL model file and the topography print cured using the PEGDA 700/water (80%/20%, wt) in the presence of IDGCM/Iod (0.5%/2%, wt) and 25 mM NaOH. (30 × 30 × 15 mm, L × W × H)..... 125

Figure 5.6. (a) The design of the seashell and (b) the transition of the seashell print cured using the PEGDA 700/water (80%/20%, wt) in the presence of IDGCM/Iod (0.5%/2%, wt) and 25 mM NaOH. (38 × 20 × 0.6 mm, L × W × H) 126

Figure S2.1.. Steady state photolysis of (a) Morin, (b) Quercetin, (c) Morin/EDB, (d) Quercetin/EDB, (e) Morin/NPG and (f) Quercetin/NPG in ethanol ([EDB] = 18 mM, [NPG] = 2 mM); UV-vis spectra recorded at different irradiation time; UV LED@394 nm irradiation (4 mW cm⁻²). 64

Figure S2.2. Photopolymerization profiles (double bond conversions vs time) of Bis-GMA/TEGDMA blend (70%/30%, w/w) along with storage time in laminate in presence of Quercetin/Iod/NPG (0.5%/2%/2%, w/w/w) PIS upon exposure of LED@410 nm (110 mW cm⁻²). 65

Figure S3.1. The relationships between mesh sizes, curing thicknesses, and C=C conversions of polymerized PEDGA 700/DI water (8/2, w/w) in the presence of naringin/Iod (0.5%/2%, wt) with diverse [NaOH] upon exposure of LED@400 nm (6.4 mW cm⁻²). 89

Figure S3.2. Photopolymerization profiles (double bond conversions vs time) of PEGDA 700/DI water (8/2, w/w) blends in the presence of naringin/Iod (0.5%/2%, wt) in laminate with diverse ratio of (a) NaOH/KOH and (b) NaOH/NaCl upon exposure to LED@400 nm (6.4 mW cm⁻²). 89

Figure S3.3. Photopolymerization profiles (double bond conversions vs time) of PEGDA 700/DI water (8/2, w/w) blends in the presence of naringin/Iod (0.5%/2%, wt) or naringin/SFO (0.5%/2%, wt) with 100 mM NaOH in laminate upon exposure to LED@400 nm (6.4 mW cm⁻²). 89

Figure S3.4. Electro-stimulated actuation of the strips (40 × 10 × 2 mm) fabricated by (a) PEGDA 700/DI water (8/2, w/w) and (b) PEGDA 700/DI water (4/6, w/w) in the presence of 4 wt% sodium acrylate, with 100 mM NaOH under irradiation of LED@400 nm; (a, b1) in the set electric field direction (anode → cathode: left → right), and (b2) in the reversed electric field direction (cathode → anode: left → right). (Voltage = 30 V); (naringin: 0.5 wt%; Iod: 2 wt%) 91

Figure S3.5. Three-point-bend test loading results of a strip structure (20 mm × 3 mm × 2 mm, L × W × H): PEGDA 700/DI water (8/2, w/w), PEGDA 700/DI water (8/2, w/w) in the presence of 2 wt% sodium acrylate, PEGDA 700/DI water (6/4, w/w) in the absence and the presence of 2 wt% sodium acrylate, and PEGDA 700/DI water (4/6, w/w) in the presence of 4 wt% sodium acrylate with 100 mM NaOH. 92

Figure S4.1. The steady-state photolysis of ellagic acid/Iod in (a) 1 mM, (b) 10 mM, (c) 100 mM, and (d) 500 mM aq. NaOH upon exposure to LED@400 nm; UV-vis spectra were recorded at different irradiation times. ([Iod] = 4.7 mM) 112

Figure S5.1. Steady-state photolysis of IDGCM/Iod in (a) water, (b) the presence of 25 mM aq. NaOH, and (c) the presence of 25 mM aq. NaCl upon exposure to LED@410 nm ([Iod] = 3.86 mM); UV-vis spectra recorded at different irradiation time. 133

Figure S5.2. Steady-state photolysis of IDGCM/Iod in water in the presence of 25 mM aq. NaOH ([Iod] = 3.86 mM) upon exposure to (a) LED@400 nm (6.4 mW cm⁻²) and (b) LED@530 nm (25 mW cm⁻²); UV-vis spectra recorded at different irradiation time. 133

Figure S5.3. Photopolymerization profiles (double bond conversions vs time) of HEA/water (50%/50%, w/w) in laminate in the presence of IDGCM/Iod (0.5%/2%, wt) with 1.25 mM – 750 mM NaOH upon exposure to the LED@410 nm (110 mW cm⁻²). 134

Figure S5.4. Photopolymerization profiles (double bond conversions vs time) of PEGDA 700/water in diverse ratios in laminate in the presence of IDGCM/Iod (0.5%/2%, wt) upon exposure to the LED@410 nm (110 mW cm ⁻²). (NaOH: 25 mM)	134
Figure S5.5. Photopolymerization profiles (double bond conversions vs time) of PEGDA 700/water (80%/20%, w/w) in laminate in the presence of IDGCM/Iod (0.05-0.5%/2%, wt) and 25 mM NaOH upon exposure to the (a) LED@410 nm (110 mW cm ⁻²) and (b) LED@400 nm (6.4 mW cm ⁻²); (c) and (d) final bond conversion of PEGDA 700/water blend and R _{p,max} as a function of IDGCM weight percentage.....	135
Figure S5.6. Photorheology profiles (storage moduli (G'), loss moduli (G'') and loss factors vs time) of photopolymerization of (a) PEGDA 700/water blend (80%/20%, wt) and (b) PEGDA 575/water blend (80%/20%, wt) in the presence of IDGCM/Iod (0.5%/2%, wt) upon exposure to LED@410 nm (110 mW cm ⁻²). (25 mM NaOH) ..	135
Figure S5.7. (a) Photobleaching of photopolymerization of PEGDA 700/water (80%/20%, wt) in presence of IDGCM/Iod (0.2%/2%, wt) upon exposure to LED@410 nm (110 mw cm ⁻²), recorded at different irradiation time (t _{ir}) and (b) photoinitiator leakage via immersion of cured rectangle at t _{ir} = 10 s in water (at immersion time, t _{im}). (25 mM NaOH)	136
Figure S5.8. Gel points of the photopolymerization of the blend of PEGDA 700/water (80%/20%, wt) at diverse thicknesses in the presence of IDGCM/Iod (0.5%/2%, wt) upon the exposure of LED@410 nm (110 mW cm ⁻²). (25 mM NaCl or 25 mM NaOH)	136
Figure S5.9. Photopolymerization profiles (double bond conversions vs time) of the PEGDA 700/water (80%/20%, wt) blend in laminate in the presence of IDGCM/Iod (0.5%/2%, wt) upon exposure to the LED@400 nm (6.4 mW cm ⁻²) and LED@410 nm (110 mW cm ⁻²). (25 mM NaCl).....	137

Chapter 1 Literature Review

1.1 Abstract

Rapid manufacturing of precise medical devices during unforeseen pandemics is imperative. In striving for shape-specific manufacturing efficiency, photopolymerization has emerged as a viable method for diverse healthcare applications in recent decades. Photopolymerization-based 3D printing offers significant potential with a range of biocompatible materials (e.g., poly(ethylene glycol), cellulose, etc.), while minimizing waste generation. However, prevalent commercial photoinitiators used in this process are synthetic and environmentally unfriendly. Therefore, the naturally occurring and derived photoinitiators have drawn tremendous research interests due to their bioactivities and inherent environmental safety. This review comprehensively outlines the medical applications implemented by these photoinitiators, highlighting their inherent photoinitiation abilities. Moreover, it delves into the impact of substituent effects on the photoinitiation abilities of naturally derived photoinitiators.

1.2 Introduction

Immediate response to the escalating need of medical devices during recent pandemics has underscored the indispensability of rapid fabrication processes. Photopolymerization-based 3D printing has evolved as a pivotal rapid fabrication technique across diverse fields, spawning extensive medical applications. Thanks to 3D printing technique in layer-by-layer manner, 3D constructs fabrication from 3D digital model including cancer tissue models, soft tissues, and more,¹⁻¹⁷ becomes facile. Given the criticality of the medical applications for health and safety, extra features (e.g., biocompatibility, degradability, etc.) should be carefully considered. Biocompatible monomers and bio-sourced monomers have been intensively investigated in the preceding years.² Photopolymerization is a strategy using light as energy to initiate polymerization. Therefore, a component, known as photoinitiator, takes responsibility for absorption of light and the bridge of active species generation. Specifically, photoinitiators absorb light, subsequently the excited photoinitiators either generate active species or facilitate reactions with coinitiators or monomers to form active species (i.e. free radicals or cations) that initiate polymerization. However, concerns persist regarding the potential adverse effects of commonly used synthetic photoinitiators such as lithium phenyl-2,4,6-trimethylbenzoylphosphinate (LAP) and bisacylphosphane oxide (BAPO), despite the presence of a catalytic quantity of photoinitiator in the composition.^{13, 14, 18} The biocompatibility and side effect concerns of these commonly used photoinitiators for medical applications were either negative or rarely evaluated.¹⁹ For instance, BAPO exposure has demonstrated

significant cytotoxicity in human oral keratinocytes and V79 fibroblasts.²⁰ While photopolymerization boasts energy-saving and solvent-free properties, the environmental impact of 3D resin formulas- particularly regarding the migration of small molecular photoinitiators and the potential for increased environmental pollution-requires careful consideration.^{19, 21}

To address the abovementioned biocompatibility issues and environmental concerns, the exploration of naturally occurring biocompatible photoinitiators is a streamlined approach to broaden the applicability of photoinitiators for medical purposes, thanks to their inherent biocompatibilities and environmental friendliness.²²⁻²⁸ Nevertheless, limited biocompatibility assessment significantly restricts the potential medical applications of these naturally occurring photoinitiators. An exception is curcumin, and it has undergone cell viability assessment. Specifically, curcumin is a versatile natural photoinitiator thereof sensitive to a broad band of the light absorption spectrum and demonstrated excellent photoinitiation ability under various light sources (from violet to red lights).²⁶ The biocompatibility evaluation of curcumin photoinitiated material was conducted. Even though the cell adhesion ability to the curcumin photoinitiated polymer impaired cell proliferation, the produced polymer demonstrated nontoxicity to human cells. Therefore, the development of naturally occurring photoinitiators for medical devices (e.g., microneedles, etc.) was considerably inspired.

Besides, the derivation of photoinitiators from naturally occurring compounds offers a complementary approach. The abundance of natural products offers diverse parent structures for the design of promising biocompatible photoinitiators tailored to specific objectives. For example, modifications incorporating macromolecular moieties can mitigate migration issues, thus ease the contact with unfavourable residual photoinitiators.²⁹ Extensive research has been conducted on naturally derived photoinitiators due to their notable advantages.³⁰⁻³⁴ These compounds, originating from nature, offering promising benefits, not only in their reduced environmental impact But also in their well-evaluated photoinitiation abilities. Moreover, some naturally derived photoinitiators have found applications in cutting-edge fields like regenerative medicines. Despite their potential in medical applications, there remains a noticeable gap in the discourse surrounding these specific areas of research. This paper aims to address this gap by shedding light on the underexplored domain of medical applications of naturally derived photoinitiators.

In response to the escalating demands for rapid medical device manufacturing, this review aims to comprehensively examine the utilization of photopolymerization in medical applications,

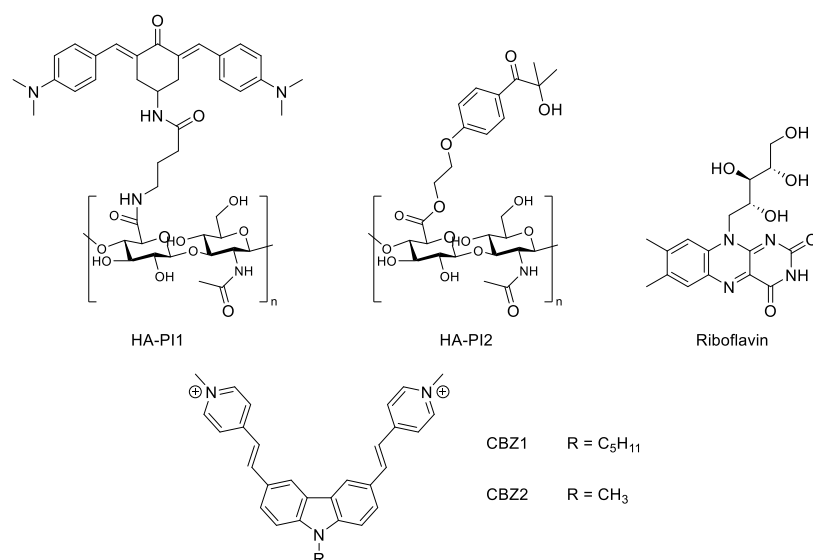
employing either naturally occurring or naturally derived photoinitiators. The realization of the prospective applications utilizing photopolymerization technology and these specific photoinitiators in the production of functional medical devices stands as a crucial goal. To this end, this review summarizes and compares the functionality evaluations of the manufactured medical devices across the included research studies. Moreover, by delving into the typical correlation between chemical structure and photoinitiation ability, this review seeks to offer insights that could guide the future structural design of naturally derived photoinitiators possessing desired photophysical properties. Specifically, the discussion explores the impact of the substituent effect on the photoinitiation ability among the naturally derived photoinitiators with identical parent structures. This review endeavours to serve as a valuable resource, providing guidance for healthcare researchers in their selection or design of appropriate naturally occurring or naturally derived photoinitiators.

1.3 Photoinitiators for regenerative medicines

Regenerative medicines rely significantly on scaffolds that facilitate the treatment of damaged tissue.³⁵ The advent of 3D printing technology has enabled the fabrication of complex structures crucial for regenerative medicines,^{36, 37} including 3D printed organ-on-a-chip and customizable artificial organs.³⁸⁻⁴² Photopolymerized scaffolds, among 3D printed materials, play a pivotal role in supporting cell proliferation. As a result, the photosensitive resin components must meet specific criteria such as biocompatibility, high porosity, and adequate mechanical strength.³⁵ In recent decades, commercialized photoinitiators like BAPO, LAP, TPO and others have been employed in tissue engineering without definitive biocompatibility assessments.^{18, 35, 43} Consequently, there has been a growing focus on the development of naturally occurring and derived photoinitiator to enhance their suitability for fabricating regenerative medicines.

Notably, certain chemicals and their derivatives have showcased exceptional photoinitiation abilities while promoting cell survival for the production of regenerative medicines. Hyaluronan, a well-known component of extracellular matrix in tissues, inherently exhibits non-toxic properties towards cells.⁴⁴ Riboflavin, recognized as vitamin B and naturally water-soluble, is an essential nutrient for humans.⁴⁵ Carbazole, found in coal tar and used in the treatment of psoriasis, has also demonstrated its efficacy.⁴⁶ The compounds, or their derivatives, have demonstrated excellent photoinitiation abilities and promising biocompatibility profiles for the production of regenerative medicines. In particular, photoinitiator substituted hyaluronan (HA-PI), riboflavin, and carbazole derivatives (CBZ) have been well-investigated as efficient either

one-photon or two-photon photoinitiators (Scheme 1.1) in the field of tissue engineering, and their biocompatibilities were also confirmed.⁴⁷⁻⁵²



Scheme 1.1. Chemical structures of HA-PIs, riboflavin, and CBZs for the application of regenerative medicines.

1.3.1 Regenerative medicines photoinitiated by hyaluronan-modified derivatives

As aforementioned, hyaluronan naturally exists in extracellular matrix, making it inherently biocompatible with cells. In addition, this macromolecule also demonstrates inherent low migration through polymer networks.⁵³ Specifically, covalent bridged hyaluronan substituted photoinitiator could considerably reduce potential hazard of the sole photoinitiator due to migration. This strategy has been applied for the commercial photoinitiator, BAPO. The macromolecule used was poly (ethylene glycol) (PEG) and cellulose nanocomposite (CNC).^{29, 54} These two developed macromolecular photoinitiators were incorporated into 3D inks, and their potential for broader applications remained unexplored. In contrast, hyaluronan was selected as the carrier for photoinitiator development for regenerative medicines due to its natural origin,^{47, 48} with the added advantage of its hydrophilic nature allowing for the inclusion of hydrophobic photoinitiators in water-rich formulas. This led to the synthesis of HA-PI1 and HA-PI2 (Scheme 1.1) via condensation, demonstrating two-photon and one-photon photoinitiation abilities, respectively. The resulting scaffolds from photopolymerization were subjected to biocompatibility assessments using both a cell line (MC3T3-E1 Subclone 4) and wild-type mice (strain C57BL/6).

HA-PI1 (Scheme 1.1) was a macromolecular photoinitiator bridged by amide bond between a designed two-photon photoinitiator and hyaluronan.⁴⁸ Utilizing the two-photon absorption

(2PA) ($\lambda_{2P} = 840$ nm) and the 2PA cross-section of 400 GM of the two-photon photoinitiator, two-photon-polymerization-based 3D printing was successfully achieved encapsulating a MC3T3 cells within a 3D resin (Figure 1.1A-a)). Excellent cell viability was observed after 24 hours and 5 days since two-photon printing (Figure 1.1A-b) and c)). Specifically, the cells in the cavity of the yin-yang structure exposed to laser exhibited proliferation and spindle morphology, while those embedded inside the yin-yang structure were protected from laser exposure and also maintained high viability. These findings underscored the exceptional biocompatibility of the selected two-photon photoinitiator, both in the presence and absence of laser exposure. Moreover, due to its large molecular size, HA-PI1 exhibited significantly reduced membrane migration compared to small molecular reference photoinitiator. Additionally, HA-PI1 demonstrated outstanding performance in the cytotoxicity assay. Specifically, the metabolic activity of HA-PI1-treated cells is the same as that of untreated cells. With confirmed biocompatibility and photoinitiation ability, HA-PI1 emerged as a promising two-photon photoinitiator for the micrometer structuring in cell media with concentrated initial cell loading.

Expanding from the cell line investigations, the hyaluronan-modified photoinitiator was further investigated in mice (strain C57BL/6) to assess the feasibility of photopolymerization technology in living organisms.⁴⁷ Considering the complexities in design and synthesis, the known efficient photoinitiator, 2-hydroxy-4'-(2-hydroxyethoxy)-2-methylpropiophenone (Irgacure 2959), was selected and incorporated into the hyaluronan-photoinitiator complex (Scheme 1.1). Despite the potential cytotoxicity of Irgacure 2959, the photopolymerization mechanism of HA-PI2 itself eliminated the residual free radicals, preventing their escape. Interestingly, the recombination of free radicals of Irgacure 2959 moieties induced crosslinking networks under the irradiation of UVA light at 366 nm. Specifically, as Irgacure 2959 was substituted onto hyaluronan, the recombination of radicals from Irgacure 2959 moieties on random hyaluronan chains formed crosslinks.⁴⁷ Therefore, HA-PI2 played dual roles as a photoinitiator and monomer simultaneously. The one-component photocurable formula ensures the homogenous phase, and the radical recombination motif prevents the potential harm of unreacted radicals to cells. In addition, given the size of hyaluronan, migration of unreacted HA-PI2 was significantly reduced, alleviating concerns of cytotoxicity associated with Irgacure 2959. Furthermore, the biocompatibility of HA-PI2 hydrogel was confirmed through implantation studies in tibialis anterior (TA) muscles. The hydrogel facilitated muscle recovery and exhibited gradual degradation within 8 days (Figure 1.1B). Hydrogel content was gradually replaced by growing muscles. This *in vivo* degradation of HA-PI2 obviated the need for scaffold removal, reducing the risk of surgical infection.

Bridging an effective photoinitiator to a natural macromolecular compound stands as a feasible and common strategy to minimize or eliminate cytotoxicity to living cells. In addition to post-modification, the investigation and development of intrinsically biocompatible photoinitiators for regenerative medicine represents an intriguing avenue. The subsequent section delves deeper into the specifics of a naturally biocompatible photoinitiator.

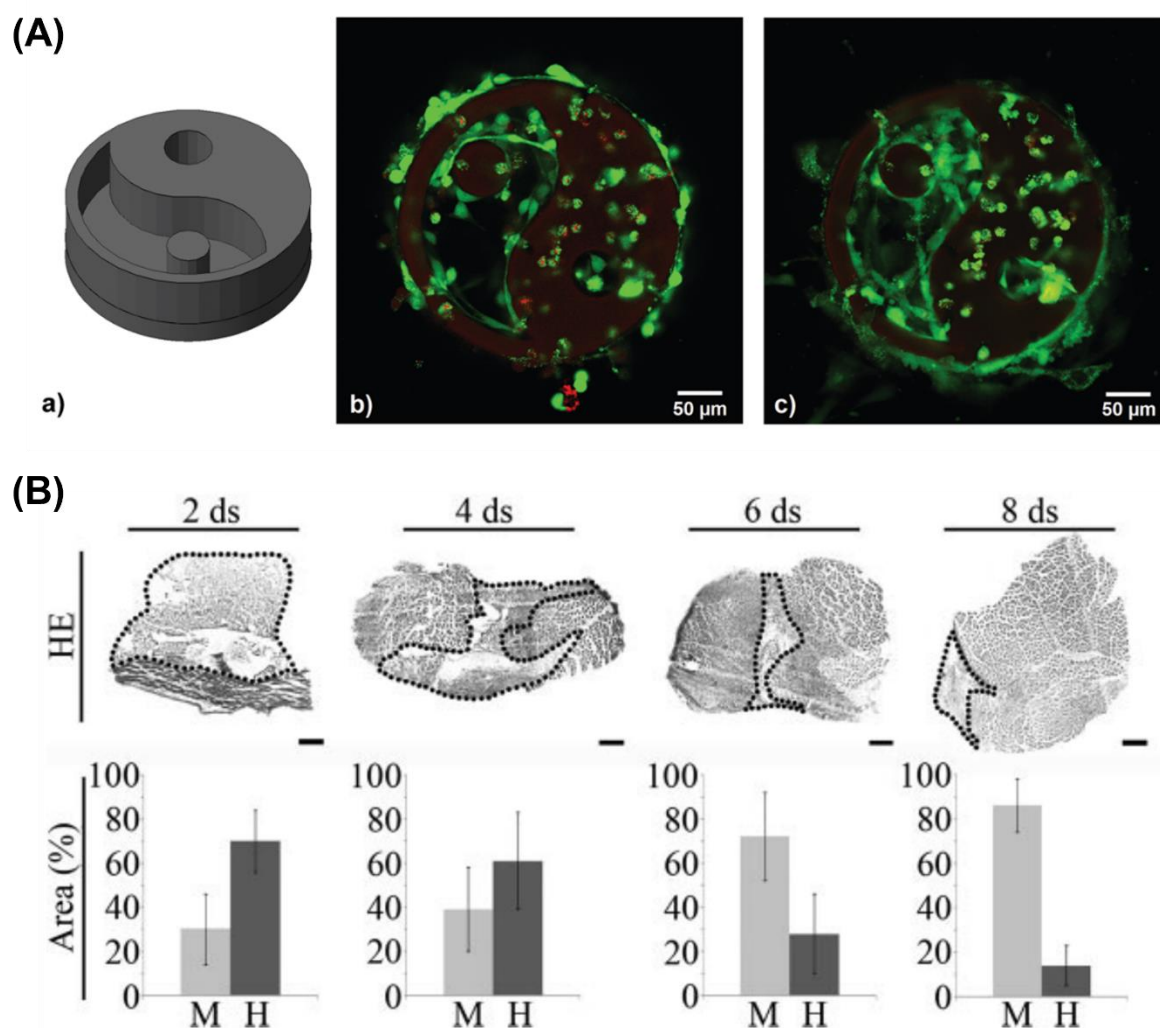


Figure 1.1. (A). a) 3D model of a yin-yang structure and the cell-laden two-photon printed yin-yang structure after b) 24 hours and c) 5 days photoinitiated by HA-PI1;⁴⁸ (B) In vivo degradation of HA-PI2 implanted in TA muscles for 2-8 days.⁴⁷ Adapted with permission from ^{47, 48}. Copyright 2011 FASEB and Copyright 2017 The Royal Society of Chemistry used under a Creative Commons Attribution 3.0 Unported License.

1.3.2 Regenerative medicines photoinitiated by riboflavin

As previously mentioned, the exploration of non-toxic natural compounds stands as a promising avenue to mitigate the risk of photoinitiator migration. Several naturally derived

compounds have demonstrated their efficacy as long-wavelength-sensitive photoinitiators.^{45, 55} Notably, riboflavin (Scheme 1.1), a well-known member of the vitamin B family, has been well-investigated as a photoinitiator. Its photoinitiation ability has been evaluated in conjunction with various coinitiators.^{25, 56-61} Leveraging its effective photoinitiation ability and naturally occurring biocompatibility, riboflavin has found widespread use in biocompatible formulas for tissue engineering.

The riboflavin-based photoinitiating system proved efficient when exposed to light within the range of 430-482 nm for the photopolymerization of a photocurable polymer, methacrylated glycol chitosan (MeGC) (Figure 1.2a). Synthesis of the photocurable polymer involved the incorporation of methacrylate groups (Figure 1.2a). Specifically, glycidyl methacrylate was grafted onto glycol chitosan to yield MeGC. The riboflavin and MeGC 3D bioink, facilitated the polymerization of MeGC upon irradiation, resulting in the production of a crosslinked MeGC hydrogel. This concept was further employed to design a cell-laden scaffold for 3D printing (Figure 1.2b). Initial confirmation of 3D printability using riboflavin as the photoinitiator involved printing mesh-shape scaffolds.⁴⁹ The resolution of the designed shape served as an assessment criterion for printability, which was modulated by varying the irradiation time. Insufficient irradiation might cause uncured damp materials, whereas excessive irradiation could lead to unnecessary shrinkage due to overcuring. Among a series of designated cure times, the 3D printed mesh-shaped scaffold exhibited the highest fidelity and precision after a 70-second irradiation, striking a balance between under- and over-irradiation.

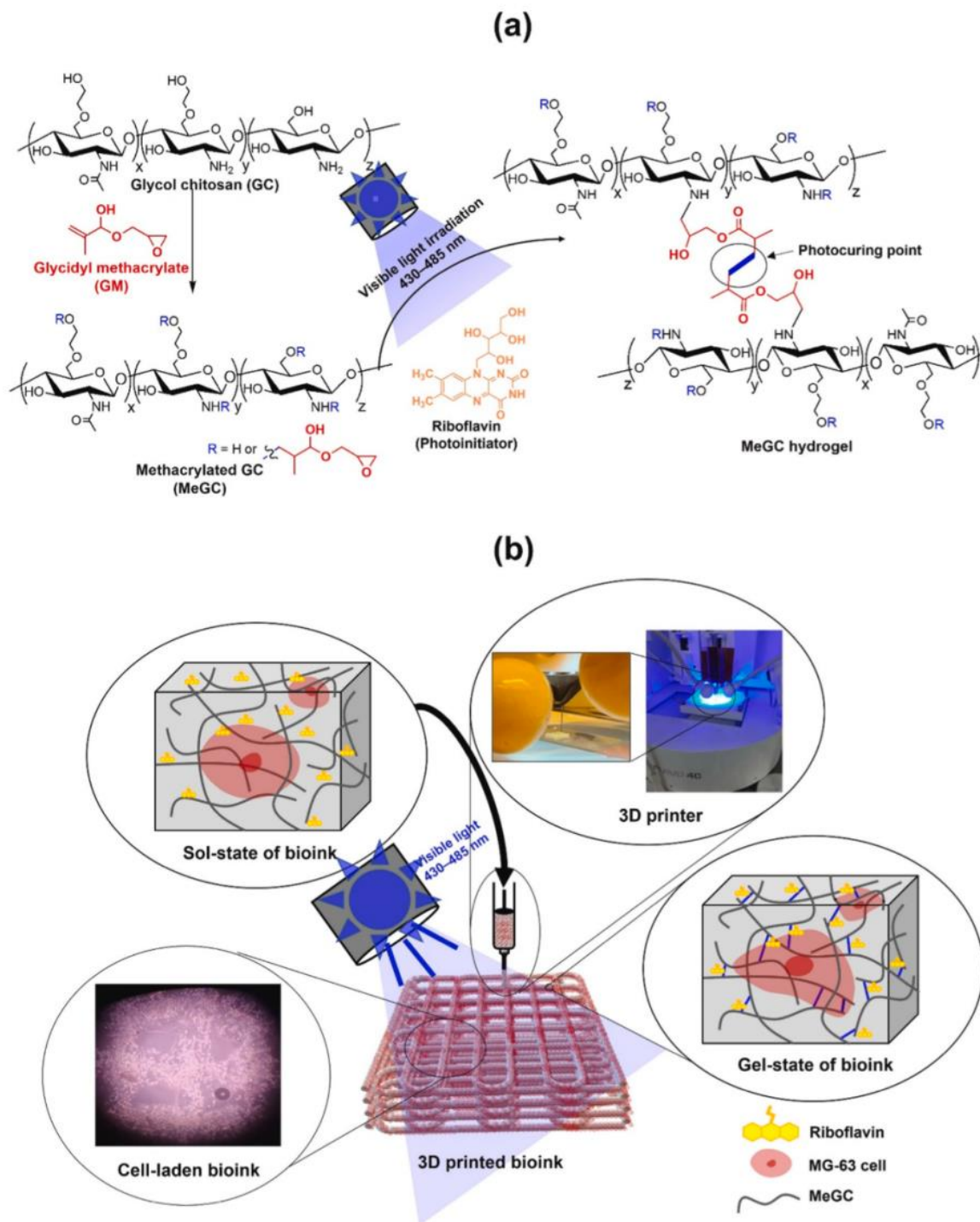


Figure 1.2. Scheme of (a) the formation of MeGC hydrogel and (b) the 3D printing of MeGC hydrogel scaffolds. Reproduced with permission from ⁴⁹. Copyright 2022 Elsevier Ltd.

The demonstrated remarkable photoinitiation ability of riboflavin under blue lights led to notable advancements in the development of corresponding 3D printed scaffolds for regenerative medicines. For example, scaffolds were successfully 3D printed using riboflavin integrated 3D ink.^{49, 50} The scaffolds of MeGC hydrogels both with and without collagen were 3D printed. The

biocompatibility of the 3D printed scaffold was evaluated through degradation studies, cell proliferation, ALP activity, and mineralization in cell-laden (MG-63 or BMSCs) hydrogels fabricated from MeGC photoinitiated by riboflavin under blue-cyan light (400-500 nm).

Expanding on Section 2.1, the incorporation of biodegradable bonds endowed the scaffold with a removal-free feature. Both collagen-treated and untreated MeGC demonstrated excellent biodegradability upon exposure to 3 mg/mL lysozyme in a PBS solution. Specifically, only 25%-30% hydrogel remained after incubation (Table 1.1). Interestingly, the introduction of collagen marginally affected the biodegradability of MeGC, slightly from 25% to 30% residual hydrogel under identical conditions. Additionally, an increase in MeGC concentration hindered biodegradation. Specifically, a 3% MeGC-involved hydrogel took 70 days to reach the remaining content of 25%, whereas a 2% MeGC hydrogel achieved a similar remaining content of 30% in just 21 days.

Additionally, both MeGC hydrogels demonstrated outstanding cell viability (> 90%) in either human or mouse cells (Table 1.1).^{49, 50} Meanwhile, its hemocompatibility, assessed through the hemolysis level upon contact with anticoagulated blood, aligned with the ISO-10993-4 standard, indicating its suitability for blood-contacting applications.⁴⁹ Examining biocompatibility, cell proliferation serves as a significant indicator. Over a 7-day culture period, the 3D printed scaffold without collagen demonstrated a gradual increase in cell counts. Conversely, when treated with collagen, the scaffold significantly enhanced the growth of cells. Specifically, cells exhibited elongated morphology, displaying continuous proliferation, and spreading. Evaluating cell viability and proliferation is crucial, yet cell differentiation is pivotal in determining the feasibility of the developed scaffold for regenerative medicine applications. Cultivating human bone cells (MG-63) within the scaffold revealed observed cell differentiation after 7-day culture period, evidenced by an ALP activity of 0.8 U/L (Table 1.1) and substantial calcium deposition of 3 at O.D. 540 nm.⁴⁹ Additionally, using the mouse bone marrow stromal cells (BMSCs) resulted in lower ALP activity and calcium deposition.⁵⁰ However, collagen treatment considerably increase the BMSC differentiation upon cell culture. Specifically, ALP activity notably increased from ~0.005 U/L (collagen-untreated) to ~0.18 U/L (collagen-treated) after a 14-day BMSC culture (Table 1.1). Furthermore, calcium expression in the collagen-treated scaffold tripled compared to the collagen-untreated scaffold. Consequently, the combination of riboflavin and curable chitosan significantly contributed to the advanced fabrication of scaffolds tailored for regenerative medicine applications.

Table 1.1. The biocompatibility indicators comparison of collagen-treated and collagen-untreated scaffold fabricated by riboflavin-induced 3D printing.^{49, 50}

	Collagen untreated	Collagen treated
Degradation	25% ¹ 30% ²	25% ²
Cell viability	> 90%	> 90%
ALP activity	~0.8 U/L ³ ~0.005 U/L ⁴	~0.18 U/L ⁴

¹ Incubation of 3% MeGC hydrogel in 3 mg/mL lysozyme in PBS solution for 70 days⁴⁹

² Incubation of 2% MeGC hydrogel in 3 mg/mL lysozyme in PBS solution for 21 days⁵⁰

³ MG-63 incubated for 7 days

⁴ BMSCs incubated for 14 days

Furthermore, the developed formula has shown remarkable potential in cartilage repair.⁶² The cell viability, proliferation, and in-situ gelation demonstrated the promising characteristics of the riboflavin photoinitiated MeGC gel for in situ cartilage regeneration. Specifically, the gel's ability to support cell viability and proliferation, as evidenced by chondrocyte viability surpassing 80% on the scaffold and observed cell growth over a 21-day incubation period, underscores its suitability for tissue regeneration. Practically, the riboflavin contained MeGC resin was evenly spread onto the cartilage defects of rabbit knee joints. Subsequently, the gel applied to the shallow defect exhibited sustained adhesion at the 14-day mark, ensuring continued attachment and delivery of the therapeutic agent.

Besides bond (joint) tissue engineering, riboflavin was also involved in ocular prostheses as a photoinitiator. In the early 2000s, riboflavin-induced collagen crosslinking was employed in the treatment of keratoconus.⁶³ The in-situ photopolymerization of collagen in the presence of riboflavin under the irradiation of UVA significantly improved corneal biomechanical stiffness, easing keratoconus. However, challenges related to corneal thickness requirements (> 400 μm) and patient discomfort due to direct irradiation exposure need to be addressed for wider application. Nonetheless, this concept holds promise for treating other ocular conditions such as myopia and hyperopia. Moreover, the versatility of riboflavin extends to alternative materials like silk fibroin for fabricating ocular prostheses. An ocular prosthesis of 40 μm thick was fabricated using silk fibroin photoinitiated by riboflavin.⁶⁴ The riboflavin-treated artificial cornea demonstrated outstanding adhesion to the cornea without degradation. Adjusting the thickness and the morphology of these riboflavin-treated artificial cornea offers a feasible avenue for treating myopia and hyperopia without invasive surgical procedures.

1.3.3 Regenerative medicines photoinitiated by carbazole Derivatives

1.3.3.1 Hydrogel scaffold

Tissue regeneration is a multiscale technology, occurring at scales ranging from centimeters down to nanometers.⁶⁵ To achieve a desired scale of tissue regenerative medicine, careful consideration of the manufacturing method is crucial, and 3D printing stands out as a promising avenue. Within 3D printing, both one-photon and two-photon techniques offer capabilities across diverse scales. Specifically, compared to one-photon induced digital light processing (DLP) 3D printing, two-photon printing demonstrates better structural resolution at the micron scale.^{66, 67} Moreover, two-photon printing, utilizing red-infrared instead of UV-visible light, operates within the optical window in biological tissues (780-800 nm irradiation sources).⁶⁸ This technique significantly mitigates photodamage, a critical factor for successful tissue regeneration processes.⁷ Therefore, the development of two-photon photoinitiating systems for biofabrication has garnered great attention in the field.⁶⁹ In addition to dedicated two-photon photoinitiators such as the aforementioned HA-PI1, there's been exploration into leveraging a single-photon photoinitiator for two-photon photopolymerization through the host-guest interaction, allowing the two-photon absorption (TPA) cross-section to be enhanced. For instance, the carbazole derivatives are well-investigated guests to hydrophilic cucurbit[7]uril (CB7), exhibiting two-photon photoinitiation abilities.^{51, 52}

CBZ1 and CBZ2 demonstrated different physical and chemical properties in the complex with CB7. The binding interaction between CBZs (Scheme 1.1) and CB7 indicated stable complexes in solution (Table 1.2). CBZ1 demonstrated better binding with CB7 compared to CBZ2 in terms of both binding ratio and binding constant (Table 1.2), suggesting the effect of alkane on R group (Scheme 1.1) on binding interactions. In addition, CBZ1 and CBZ2 exhibited similar light absorption maxima (at ~ 450 nm) and negligible fluorescence upon the excitation at either 440 nm or 450 nm for CBZ1 or CBZ2, respectively. Contrarily, the addition of CB7 drastically enhanced the fluorescence of CBZs in aqueous solution. Subsequently, complexed with CB7, the CBZs exhibited a considerably increased TPA cross-section of ~2500 GM (Table 1.2). The substantial increase in the TPA cross-section can significantly reduce the laser power threshold, facilitating the initiation of two-photon processes. Demonstrating their capabilities, micron-scale objects produced through two-photon 3D printing further affirmed their printability for such applications (Figure 1.3a-d).

Even though residual CBZs/CB7 complexes exhibited bright fluorescence in the microstructures from confocal fluorescence images (Figure 1.3e and g), their

biocompatibilities in terms of cell morphologies (Figure 1.3f and h) and cell density was exceptional. Specifically, the Hela cells (Figure 1.3f) and L929 (Figure 1.3h) maintained their morphologies, exhibiting continuous growth and reaching a cell density of $\sim 550/\text{mm}^2$. This successful cell growth on the hydrogel scaffold fabricated by two-photon printing in the presence of CBZs/CB7 complexes confirms the potential application of host-guest motif in developing two-photon photoinitiating systems for regenerative medicines.

Table 1.2. The binding interaction parameters and photophysical properties of CBZ1 and CBZ2.^{51, 52}

	CBZ1	CBZ2
Binding ratio with CB7	0.97 ± 0.008	0.939 ± 0.027
Binding constant with CB7	$(6.01 \pm 0.75) \times 10^5 \text{ M}^{-1}$	$(2.18 \pm 0.56) \times 10^5 \text{ M}^{-1}$
TPA cross-section	613 GM	750 GM
TPA cross-section with CB7	$\sim 2500 \text{ GM}$	$\sim 2500 \text{ GM}$

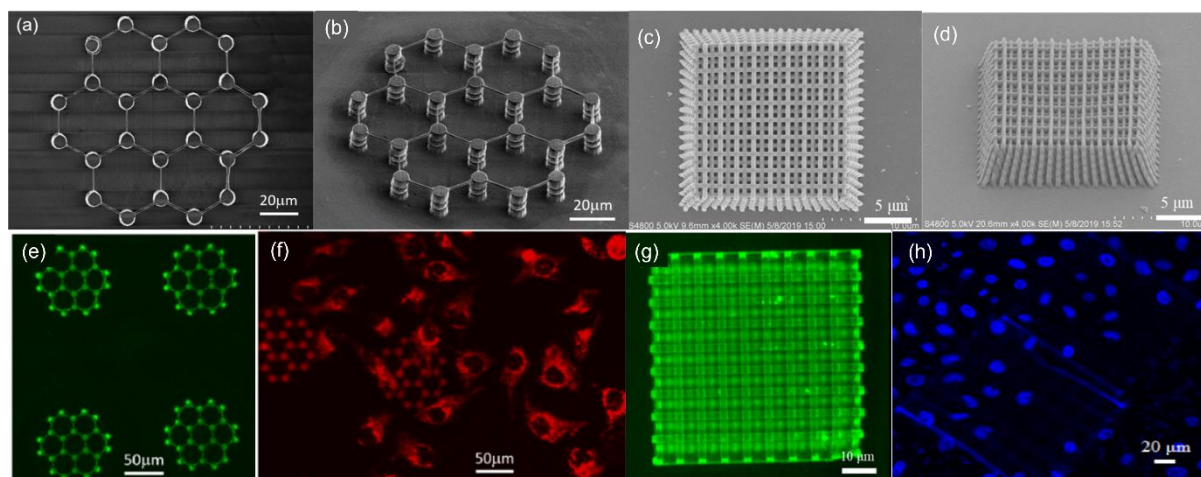
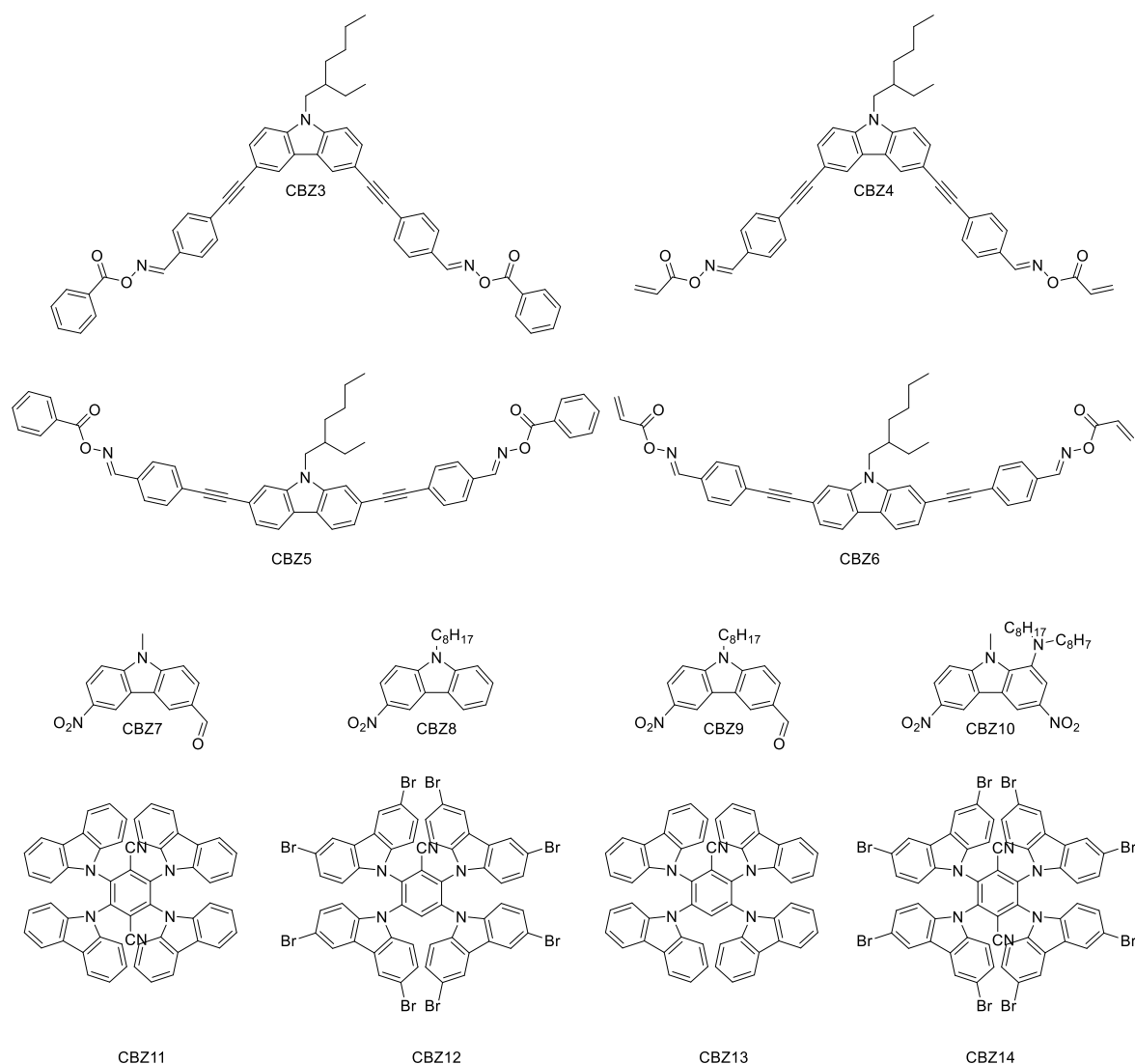


Figure 1.3. (a-d) SEM images of two-photon microfabricated structures in (a, c) top view and (b, d) side view, and (e-h) confocal fluorescence images of (e, g) hydrogel scaffold and (f, h) cell-laden hydrogel scaffold; (a-b, e-f) CBZ1/CB7 complex or (c-d, g-h) CBZ2/CB7 complex as two-photon photoinitiators. Adapted with permissions from^{51, 52}. Copyright 2019 American Chemical Society and Copyright 2021 American Chemical Society.

1.3.3.2 Chemical structure effect on photoinitiation abilities of carbazole derivatives

Besides the host-guest motif, esterification with oxime esters and structural modification can also promote the photophysics and one-photon and two-photon photoinitiation abilities.⁷⁰ For instance, in the context of CBZ3-4 and CBZ5-6 (Scheme 1.2), their one-photon light absorption peaks at 377 nm and 371 nm respectively, highlight the red-shift induced by the para-substitution. However, an intriguing observation emerges when comparing their molar extinction coefficients at these respective absorption maxima, with para-substituted CBZs (CBZ3-4) displaying higher molar extinction coefficients ($\sim 75,000 \text{ M}^{-1} \text{ cm}^{-1}$) compared to meta-substituted CBZs (CBZ5-6) ($\sim 55,000 \text{ M}^{-1} \text{ cm}^{-1}$). The effect of the end group of vinyl on the

photoinitiation ability of CBZ is noteworthy. The utilization of CBZ4 instead of CBZ3 led to an increase in double bond conversions of trimethylolpropane triacrylate (TMPTA) and ethoxylated trimethylolpropane triacrylate (TMP3EOTA) (functional group ratio = 1:1) from 40% to 57%. This enhancement underscores the significant contribution of the vinyl end group to the superior photoinitiation ability of CBZ, particularly in achieving higher final double bond conversion. Interestingly, while CBZ5 exhibited limited free radical photoinitiation ability upon exposure to LED@405 nm, the introduction of vinyl substitution notably improved the photoinitiation capabilities of CBZ4 and CBZ6 to a level comparable to that of a commercially available photoinitiator, diphenyl(2,4,6-trimethylbenzoyl) phosphine oxide (TPO). Notably, the exceptional photoinitiation ability of CBZ6 facilitated the successful 3D printing of a highly precise object with minimal 0.1-mm deviation. Moreover, the application of CBZ-oxime ester in two-photon 3D printing deserves attention. CBZ6, in particular, exhibited the highest TPA cross-section (136 GM) among CBZ3-6 along with demonstrating the broadest ideal processing window of laser power from 7 to 32 mW. These insights into the two-photon photophysical properties enabled the microfabrication of a microstructure using two-photon 3D printing technology.



Scheme 1.2. Chemical structures of carbazole derivatives.

Furthermore, the addition of coinitiator(s) (e.g., bis-(4-tertbutylphenyl) iodonium hexafluorophosphate (Iod)) can also improve CBZ derivatives' one-photon photoinitiation abilities. CBZ7-10 (Scheme 1.2) exhibited their maximum light absorptions at ~ 370 nm (Table 1.3).^{71,72} Initially, CBZ7 and CBZ9 exhibit identical light absorption maxima; however, the molar extinction coefficient of CBZ9 is significantly higher, indicating that the N-substitution merely influences the molar extinction coefficient rather than the absorption maxima. Furthermore, the substitution of aldehyde on CBZ9 blue-shifted its light absorption to 364 nm. In contrast, the push-pull effect between amine and nitro groups on CBZ10 induced a red-shifted light absorption.⁷¹ Interestingly, the extension of the conjugated band led to a blue shift when comparing CBZ11-14 (Scheme 1.2) with CBZ7-10 (Table 1.3). Incorporating CBZ7-14/Iod into monomers demonstrated their abilities in both free radical and cationic photoinitiation under the irradiation of LED@405 nm. Regarding the cationic photopolymerization of (3,4-

epoxycyclohexane)methyl 3,4-epoxycyclohexylcarboxylate (EPOX), CBZ11-14 showcased similar photoinitiation abilities. In contrast, the cationic photoinitiation abilities of CBZ7-10 were significantly distinct. Specifically, CBZ7/Iod resulted in the highest epoxy conversion of 76%, despite its comparatively low molar extinction coefficient at 405 nm. However, the energy of electron transfer between CBZ7-10 and Iod were similar.⁷¹ This may be attributed to the stabilizing effect of N-methyl substitution on CBZ⁺, determining higher cationic reactivities. Moreover, regarding the free radical photopolymerization of TMPTA, CBZ7-10 exhibited similar free radical photoinitiation abilities, while significant differences were observed in CBZ11-14 (Table 1.3). Specifically, CBZ13 demonstrated the best free radical photoinitiation ability in the presence of Iod, achieving a 58% double bond conversion among CBZ11-14. The double bond conversion in the presence of CBZ12/Iod was reduced by 8% compared to CBZ13/Iod, suggesting that the halogenated substitutions on CBZ12 potentially weakened the free radical photoinitiation ability. Similar final conversions were found in the photopolymerization of TMPTA in the presence of CBZ11/Iod and CBZ14/Iod. Meanwhile, the addition of substituent (CBZ11 and CBZ14), -CN, reduced the free radical photoinitiation abilities as well. Consequently, this comprehensive investigation into the photoinitiation abilities of CBZs, validated the 3D printing capability of the developed CBZ-based photoinitiating systems (CBZ8/Iod and CBZ13/Iod) through laser write experiments, achieving writing in a remarkably short time (< 1 min), resulting in the written letters with thicknesses of only 230 μm or 500 μm .

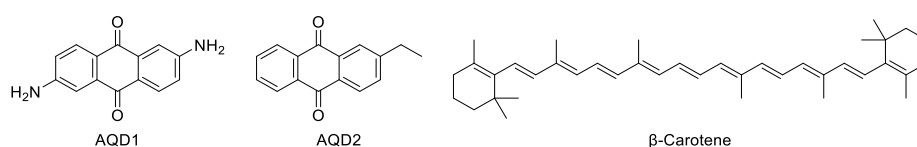
Table 1.3. The photophysical properties of CBZs and the final functional group conversions of TMPAT or EPOX in the presence of CBZ/Iod (0.5%/1%, wt). Adapted with permission from ⁷¹, ⁷². Copyrights 2017 American Chemical Society.

	λ_{max}	ϵ_{max}	$\epsilon_{405 \text{ nm}}$	Conversion (EPOX)	Conversion (TMPTA)
CBZ7	364 nm	$\sim 11,750 \text{ M}^{-1} \text{ cm}^{-1}$	$\sim 2600 \text{ M}^{-1} \text{ cm}^{-1}$	76%	46%
CBZ8	374 nm	$\sim 11,180 \text{ M}^{-1} \text{ cm}^{-1}$	$\sim 5200 \text{ M}^{-1} \text{ cm}^{-1}$	50%	56%
CBZ9	364 nm	$\sim 25,000 \text{ M}^{-1} \text{ cm}^{-1}$	$\sim 2450 \text{ M}^{-1} \text{ cm}^{-1}$	58%	49%
CBZ10	388 nm	$\sim 6000 \text{ M}^{-1} \text{ cm}^{-1}$	$\sim 5200 \text{ M}^{-1} \text{ cm}^{-1}$	70%	50%
CBZ11	300 nm	$\sim 8800 \text{ M}^{-1} \text{ cm}^{-1}$	$\sim 1350 \text{ M}^{-1} \text{ cm}^{-1}$	47%	23%
CBZ12	340 nm	$\sim 40,000 \text{ M}^{-1} \text{ cm}^{-1}$	$\sim 7800 \text{ M}^{-1} \text{ cm}^{-1}$	55%	50%
CBZ13	333 nm	$\sim 3300 \text{ M}^{-1} \text{ cm}^{-1}$	$\sim 5700 \text{ M}^{-1} \text{ cm}^{-1}$	55%	58%
CBZ14	349 nm	$\sim 18,000 \text{ M}^{-1} \text{ cm}^{-1}$	$\sim 3300 \text{ M}^{-1} \text{ cm}^{-1}$	50%	47%

1.4 Photoinitiators for Antibacterial or Antifouling Coatings

The pursuit of antibacterial surface modification and products aims to eradicate bacteria or hinder their growth. Recently, a 3D antibacterial hydrogel was produced using carbazole derivatives as photoinitiators via 3D printing technology.⁷³ With the addition of silver

nanoparticles, this hydrogel disc demonstrated a visible antibacterial effect with a bacteria-free circle. However, while the creation of 3D antibacterial objects holds promise, surface modification through antibacterial coatings presents a simpler and more cost-effective manner for comprehensive protection. The antibacterial coatings can be in-situ fabricated on the surface of targeted objects via photopolymerization technology, preventing bacterial biofilm formation on various surfaces, particularly on medical devices.⁷⁴⁻⁷⁶ For instance, coatings were successfully fabricated within 15 min or less under exposure to UV LED@365 nm and exhibited excellent antibacterial effects for both Gram-positive and Gram-negative bacteria (> 99% reduction rate of bacteria). However, the photoinitiators utilized in these processes, such as 2-hydroxy-4'-(2-hydroxyethoxy)-2-methylpropiophenone (Irgacure 2959), 2-hydroxy-2-methylpropiophenone (Irgacure 1173), and 2,2-dimethoxy-2-phenylacetophenone (DMPA), are synthetic and potentially pose environmental risks. In contrast, there is growing interest in employing naturally derived compounds like anthraquinone derivatives (AQDs) and naturally occurring β -carotene, derived from plants, fungi, fruit, or insects,^{77, 78} as photoinitiators for the fabrication of antibacterial/antifouling coatings. Some of the AQDs serve as food colorants, textile dyes, or even antimicrobial drugs.⁷⁹⁻⁸⁵ Besides, β -carotene functions as a food colorant and antioxidant.⁷⁸ Leveraging these naturally occurring/derived photoinitiators (Scheme 1.3), antibacterial coatings were efficiently fabricated on substrates like either stainless-steel, cotton fabrics, or glass slides.⁸⁶⁻⁸⁸ These coatings exhibited resistance to bacteria, as demonstrated through investigations involving both the Gram-negative bacteria, such as *Escherichia coli* (*E. coli*), and the Gram-positive bacteria, including *Staphylococcus aureus* (*S. aureus*). This approach offers promise in developing environmentally friendly and effective antibacterial coatings, addressing concerns related to synthetic photoinitiators and promoting sustainable antibacterial surface modifications.



Scheme 1.3. Chemical structures of anthraquinone derivatives (AQDs) and β -carotene for the fabrication of antibacterial coatings.

Table 1.4. The composition of prepolymers for the fabrication of antibacterial coatings.⁸⁶⁻⁸⁸

Entry	Photoinitiators	Irradiations	Reactive components	Monomers ²	Substrates	Reduction rate of bacterial count		Ref
						<i>E. coli</i>	<i>S. aureus</i>	
1	AQD1	Xenon lamp (30 mW cm ⁻²)	GPTMS ¹	EPOX	Stainless-steel substrates	97%	97%	⁸⁶
2	AQD2	365 nm (3 mW cm ⁻²)	AQD2	AAm, DMMSA, OFA and BA	Cotton fibers	99%	99%	⁸⁷
3	β-Carotene	405 nm (100 mW cm ⁻²)	Eugenol	DPDO and Lim	Glass slides	80%	50%	⁸⁸

¹ GPTMS: 3-glycidylxypropyltrimethoxysilane

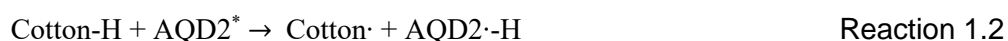
² EPOX: 3,4-epoxycyclohexylmethyl-3,4-epoxycyclohexanecarboxylate; AAm: acrylamide; DMMSA: [2-(methacryloyloxy) ethyl] dimethyl-(3-sulfopropyl) ammonium hydroxide; OFA: 1*H*, 1*H*, 5*H*-octafluoropentyl acrylate; BA: butyl acrylate; DPDO: dipentene dioxide; Lim: limonene 1,2-epoxide

1.4.1 Anthraquinone derivatives

1.4.1.1 Antibacterial or antifouling coatings

Among effective AQD photoinitiators, AQD1 and AQD2 (Scheme 1.3) are the two exceptional photoinitiators for the fabrication of antibacterial coatings through either cationic or free radical polymerization.^{86, 87} Unlike the aforementioned synthetic photoinitiators, AQD1, in combination with diphenyliodonium hexafluorophosphate (Iod1), exhibited potent photoinitiation capability in the cationic polymerization of 3,4-epoxycyclohexylmethyl-3,4-epoxycyclohexanecarboxylate (EPOX) under the irradiation of a commercially available xenon lamp (> 350 nm).⁸⁶ Interestingly, the incorporation of benzoyl alcohols significantly accelerated the photolysis of the excited AQD1^{*}, indicating subsequent photopolymerization. Particularly, the presence of benzoyl alcohol notably improved the conversions of epoxides up to 86%, surpassing the performance of the photoinitiating system in the absence of benzoyl alcohol (AQD1/Iod1). Notably, the rates of polymerization and the conversions of epoxides varied depending on the cations derived from benzoyl alcohols and their electron-donating substituents. Among the investigated benzoyl alcohols, 2,5-dimethoxybenzyl alcohol (DMBzOH) exhibited unprecedented improvement in the cationic photopolymerization of EPOX, achieving an 86% conversion rate.

Additionally, apart from cationic polymerization, AQDs was employed in free radical polymerization for the application of antibacterial coatings. Using AQD2-dyed (Scheme 1.3) cotton fabrics, a photocurable resin mixture (Table 1.4) were successfully grafted onto the AQD2-dyes cotton fabrics under the irradiation of ultraviolet (UV) at 365 nm.⁸⁷ The graft polymerization proceeded via a mechanism involving Reaction 1.1 to Reaction 1.3. Specifically, under irradiation, the excited AQD2 produced from Reaction 1.1 abstracts hydrogens from cotton fabrics (Reaction 1.2). Afterward, the monomers were grafted onto cotton fabrics through polymerization initiated by free radicals on cellulose chains (Reaction 1.3). Notably, the radicals on AQD2 (AQD2·-H) were less reactive than the ones on the cellulose chain (Cotton) due to the high steric hindrance of AQD2, thus the cotton radical rather than AQD2 radical served as the active species for subsequent polymerization.⁸⁷



Consequently, employing the developed photoinitiating system (AQD1/Iod1/DMBzOH) along with the antibacterial reactive component and 3-glycidyloxypropyltrimethoxysilane (GPTMS), a coating was successfully attached to a stainless-steel substrate under irradiation. In addition, various coatings grafted with diverse monomers (Table 1.4: entry 2) were fabricated by the AQD2-dyed cotton fabrics. The resulting antifouling and antibacterial coatings exhibited substantial reduction in bacteria count: 97% for AQD1-initiated coatings and 99% for AQD2-initiated coatings against both Gram-negative and Gram-positive bacteria (Table 1.4 and Figure 1.4). These coatings demonstrated comparable antibacterial effect to the ones fabricated by Irgacure 2959, although the mechanisms of the antibacterial process differed.⁷⁴ Typically, regarding the coatings on stainless steel initiated by AQD1, the reactive component GPTMS played an important role thanks to the silanol moieties in either the bacteria adherence or bacteria membrane disruption.⁸⁹ In contrast, AQD2 directly engaged in the antibacterial process by generating reactive oxygen species under 365 nm illumination, hindering bacterial biofilm formation.⁸⁷ Additionally, the presence of the grafted polymer favored the light-induced reactions.

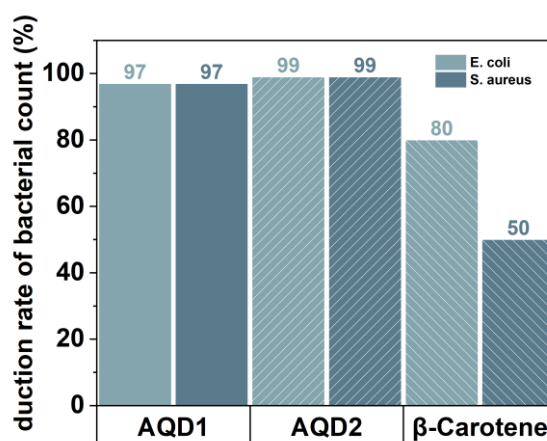


Figure 1.4. The reduction rate of bacterial count on the coatings fabricated by AQD1, AQD2, and β -carotene under irradiations.⁸⁶⁻⁸⁸

1.4.1.2 Substituent effect on photoinitiation ability

In the quest for suitable photoinitiators for the fabrication of antibacterial coatings, anthraquinone-derivative dyes have emerged as promising candidates, as highlighted in both Scheme 4 and Scheme 5.^{30-32, 90-95} To further improve the efficiency of coating fabrication, it becomes imperative to delve deeper into understanding the influence of substitutions on the photoinitiation abilities of anthraquinone derivatives. In the 2000s, arylmethyloxy-substituted anthraquinones were synthesized, which exhibited the ability to photoinitiate both free radical and cationic polymerizations.⁹⁰ However, their photoinitiation abilities were found to be insufficient (< 20% double bond conversions under ambient conditions), thereby the effect of substitution was ambiguous. Recent advancements have demonstrated promising outcomes, notably with newly reported AQDs substituted with amino or hydroxyl groups (Scheme 1.4 and Scheme 1.5). These derivatives exhibited excellent photoinitiation abilities, particularly showcasing sensitivity to long-wavelength visible light (LED@518 nm, LED@594 nm, and LED@636 nm),^{31, 32, 92, 94, 95} which can avoid the potential damages caused by UV irradiation⁹⁶⁻⁹⁹. Of particular interest is the sensitivity of most AQDs were to the entire band or visible light (Table 1.5), with some derivatives, notably, AQD-NH2-8, demonstrating sensitivity even to infrared irradiation.⁹⁴ The newfound capability of these anthraquinone derivatives to effectively respond to longer-wavelength light sources not only opens new avenues for antibacterial coating fabrication but also presents a safer and more versatile approach by reducing potential damage to substrates and surrounding environments caused by UV irradiation.

Table 1.5. The irradiation sources for the investigated AQDs.^{30-32, 91-95}

Photoinitiators	Irradiation	Intensities	References
AQD-OH-1	Halogen lamp (370 – 800 nm); Red laser diode (635 nm); LED@455 nm; LED@518 nm	~12 mW cm ⁻² ; 100 mW cm ⁻² ; 100 mW cm ⁻² ; 60 mW cm ⁻²	32, 93
AQD-OH-2	LED@455 nm; LED@518 nm	100 mW cm ⁻² ; 60 mW cm ⁻²	32
AQD-OH-3			
AQD-OH-4			
AQD-OH-5	LED@518 nm	60 mW cm ⁻²	95
AQD-OH-6			
AQD-OH-7			
AQD-NH2-1	LED@455 nm	60 mW cm ⁻²	91
AQD-NH2-2			
AQD-NH2-3			
AQD-NH2-4	LED@455 nm; LED@518 nm; LED@594 nm; LED@636 nm	60 mW cm ⁻² ; 60 mW cm ⁻² ; 30 mW cm ⁻² ; 60 mW cm ⁻²	30, 31
AQD-NH2-5			30, 31, 92
AQD-NH2-6			
AQD-NH2-7	Halogen lamp (370 – 800 nm); Red laser diode (635 nm); LED@392 nm; LED@455 nm; LED@518 nm; LED@594 nm; LED@636 nm; Infrared bulb (590 – 1080 nm)	~12 mW cm ⁻² ; 100 mW cm ⁻² ; 100 mW cm ⁻² ; 100 mW cm ⁻² ; 60 mW cm ⁻² ; 60 mW cm ⁻² ; 30 mW cm ⁻² ; 90 mW cm ⁻² ; 100 mW cm ⁻²	93, 94
AQD-NH2-8	LED@392 nm; LED@455 nm; LED@518 nm; LED@594 nm; LED@636 nm; Infrared bulb (590 – 1080 nm)	100 mW cm ⁻² ; 100 mW cm ⁻² ; 60 mW cm ⁻² ; 30 mW cm ⁻² ; 90 mW cm ⁻² ; 100 mW cm ⁻²	94
AQD-NH2-9			
AQD-NH2-10	Halogen lamp (370 – 800 nm); Red laser diode (635 nm)	~12 mW cm ⁻² ; 100 mW cm ⁻²	93

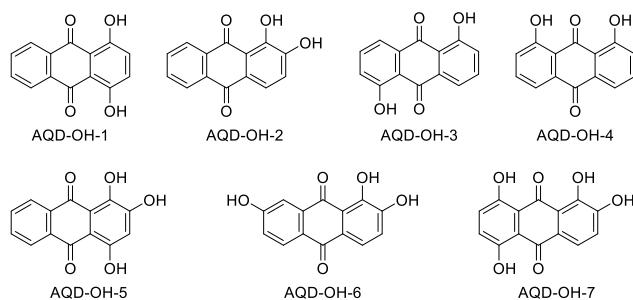
1.4.1.2.1 Hydroxyl-substituted anthraquinone derivatives (AQD-OHs)

The introduction of hydroxyl groups into anthraquinone derivatives yielded diverse effects on their photoinitiation capabilities in cationic polymerization and free radical polymerizations. The positioning of these substitutions significantly influenced the anthraquinone derivatives' effectiveness in cationic polymerization, while their abilities in initiating free radical polymerization of bisphenol A glycerolate dimethacrylate (Bis-GMA)/triethylene glycol dimethacrylate (TEGDMA) (70%/30%, wt) remained relatively consistent across most cases (Table 1.6). For instance, photoinitiating systems based on AQD-OH-1, AQD-OH-3, and AQD-

OH-4 resulted in double bond conversions of 40%-50% in Bis-GMA/TEGDMA (70%/30%, wt) upon exposure to LED@455 nm. In contrast, the impact of hydroxyl substitutions on their photoinitiation abilities in cationic polymerization of EPOX varied significantly. The AQD-OH-2/Iod1/NVK (0.5%/2%/3%, wt) failed to photoinitiate the polymerization of EPOX, whereas AQD-OH-4/Iod1/NVK (0.5%/2%/3%, wt) achieved an impressive 79% epoxide conversion of EPOX under LED@455 nm (Table 1.6). Moreover, trihydroxy-substituted AQDs (AQD-OH-5~7) demonstrated notable photoinitiation abilities under green irradiation, as evidenced by the photopolymerization of Bis-GMA/TEGDMA (70%/30%, wt) upon exposure to green LED@518 nm (Table 1.6).⁹⁵ AQD-OH-5/TEAOH/R-Cl (0.5%/2%/2%, wt) achieved a comparable double bond conversion of 49% under the irradiation of LED@518 nm. Furthermore, the polymerization of DVE-3 reached an impressive 90% for the AQD-OH-5-based photoinitiating systems. These findings confirm the significant potential of multi-substituted AQD-OH derivatives, not only in enhancing their photoinitiation abilities but also in potentially improving their water solubilities, rendering them suitable for applications in aqueous environments like hydrogels and related applications.

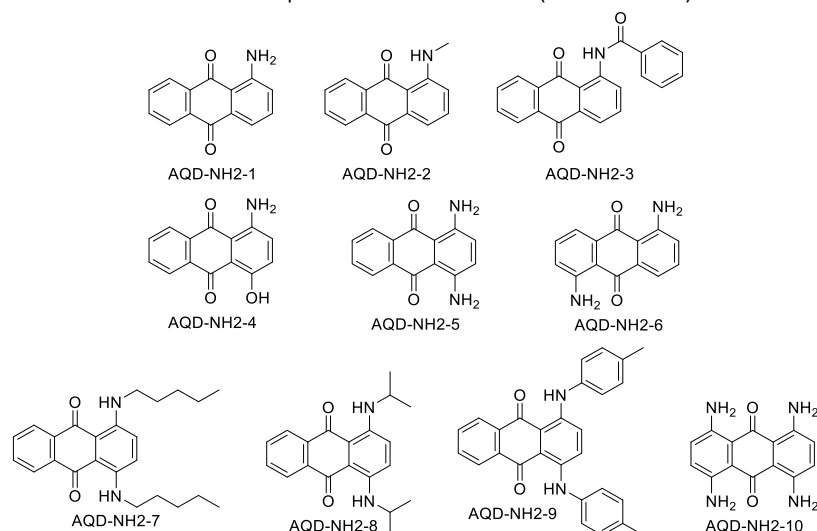
Table 1.6. Final conversions of Bis-GMA/TEGDMA (70%/30%, wt), EPOX, and DVE-3 in the presence of AQD-OH-based photoinitiating systems upon exposure to LED@455 nm and/or LED@518 nm. (AQD-OH: 0.5 wt %; TEAOH, R-Br, or Iod1: 2 wt %; NVK: 3 wt %)^{32, 95}

Photoinitiating system	Conversion (%)			
	LED@455 nm		LED@518 nm	
	Bis-GMA/TEGDMA	EPOX	Bis-GMA/TEGDMA	DVE-3
AQD-OH-1/Iod1/NVK	50	67	47%	-
AQD-OH-1/TEAOH/R-Cl	48	-	-	-
AQD-OH-2/Iod1/NVK	0	0	-	-
AQD-OH-2/TEAOH/R-Cl	0	-	-	-
AQD-OH-3/Iod1/NVK	45	15	-	-
AQD-OH-3/TEAOH/R-Cl	38	-	-	-
AQD-OH-4/Iod1/NVK	55	79	35%	-
AQD-OH-4/TEAOH/R-Cl	56	-	-	-
AQD-OH-5/Iod1	-	-	40%	90
AQD-OH-5/Iod1/NVK	-	-	-	90
AQD-OH-5/R-Cl	-	-	40%	-
AQD-OH-5/TEAOH/R-Cl	-	-	49%	-
AQD-OH-7/Iod1	-	-	38%	-



Scheme 1.4. Chemical structures of hydroxyl-substituted anthraquinone derivatives (AQD-OHs) for photopolymerizations.

1.4.1.2.2 Amino-substituted anthraquinone derivatives (AQD-NH₂s)



Scheme 1.5. Chemical structures of amino-substituted anthraquinone derivatives (AQD-NH₂s) for photopolymerizations.

The introduction of amino groups into anthraquinone derivatives has demonstrated significant enhancements in their light sensitivities and the photoinitiation abilities, surpassing those achieved with hydroxyl substitutions. The modulation of these capabilities has been achieved by varying the amount of amino substituents, the substituted position, and the amino group structures. Therefore, AQD-NH₂-1 ~ AQD-NH₂-10 (Scheme 1.5) systematically examined to discern the impact of amino substituents on the photoinitiation abilities of anthraquinone derivatives, showcasing their effectiveness in inducing free radical or cationic polymerizations.^{31, 91-94} With the addition of Iod1 and N-vinylcarbazole (NVC), amino-substituted AQDs (i.e., AQD-NH₂-1 ~ AQD-NH₂-3) displayed diverse photophysical properties and distinctive photoinitiation abilities in cationic photopolymerization of EPOX.⁹¹ For instance, AQD-NH₂-1 exhibited its absorption maxima at 465 nm, suggesting its excellent overlapping with the emission spectrum of LED@455 nm. Subsequently, a 30% epoxide conversion was observed upon exposure to LED@455 nm. With the substitution of a N-methyl group, the light absorption of AQD-NH₂-2 was blue-shifted slightly, and the overlapping with LED@455 nm

was significantly reduced. Consequently, a reduced epoxide conversion (12%) was observed after 780-second exposure to LED@455 nm. In contrast, the AQD-NH2-3 demonstrated a red-shifted light absorption, showcasing the highest photoinitiation ability, achieving a 53% epoxide conversion, and the highest polymerization rate upon exposure to LED@455 nm (60 mW cm⁻²). This can be ascribed to the significant orbital contribution from the benzamido substitution, offering low-lying nπ* states of AQD-NH2-3 that allows sufficient energy for electron transfer among AQD-NH2-3, Iod1, and NVK.⁹¹

Moreover, investigations involving hetero/homo di-substituted AQDs unveiled intriguing insights into their photoinitiation abilities to both cationic and free radical photopolymerization under irradiations from blue light to red light (Table 1.7).^{30, 31} AQD-NH2-4, synthesized from AQD-NH2-1 with substitution of a hydroxyl group, exhibited insufficient photoinitiation ability in cationic polymerization of EPOX and no efficacy in free radical polymerization of trimethylolpropane triacrylate (TMPTA), tripropyleneglycol diacrylate (TPGDA), and bisphenol A epoxy diacrylate/TPGDA (75/25, w/w) (EB605) under all investigated conditions. AQD-NH2-5 and AQD-NH2-6, modified from AQD-NH2-1 with substitution of an amino group, demonstrated exceptional capabilities, especially when paired with NVK, triethanolamine (TEAOH) and phenacyl bromide (R-Br). Compared to the AQD-NH2-5-based multi-component photoinitiating systems, the AQD-NH2-6-based corresponding photoinitiating systems exhibited comparable photoinitiation abilities for cationic polymerization and better photoinitiation abilities for free radical polymerization. Specifically, the epoxide conversions of EPOX in the presence of AQD-NH2-5-based and AQD-NH2-6-based three-component photoinitiating systems under the irradiations of LED@455 nm were 73% and 85%, respectively. The addition of amino substituent significantly improved the photoinitiation ability of amino-substituted AQD compared to AQD-NH2-1 (30% epoxide conversion under the same condition).^{30, 91} Moreover, under the irradiation of LED@518 nm, the epoxide conversions of EPOX were 80% and 83% in the presence of AQD-NH2-5-based and AQD-NH2-6-based three-component photoinitiating systems, respectively (Table 1.7). Impressively, AQD-NH2-5 also exhibited red-light sensitivity and successfully photoinitiated EPOX polymerization (77%-78% epoxide conversion) in the presence of Iod1/NVK (2%/3%, wt) under yellow and red LEDs.³⁰ The cationic photopolymerization of tri(ethylene glycol) divinyl ether (DVE-3) followed a similar order.

For the free radical photopolymerization, the double bond conversions of TPGDA were only 14% and 15% in the presence of AQD-NH2-5/Iod1/NVK (0.5%/2%/3%, wt) upon exposure to LED@455 nm and LED@518 nm, respectively. In contrast, the double bond conversions of

TPGDA reached 63% and 59% when AQD-NH2-6 replaced AQD-NH2-5. In the presence of TEOH and/or R-Br, AQD-NH2-4 exhibited no photoinitiation ability under irradiation of both LEDs, while AQD-NH2-5 notably induced TPGDA photopolymerization. Especially, compared to those in the presence of two-component photoinitiating systems, exceptional double bond conversions of 82% and 78% were observed for TPGDA in the presence of a three-component photoinitiating system (AQD-NH2-5/TEAOH/R-Br: 0.5%/2%/2%, wt) upon exposure to LED@455 nm and LED@518 nm.³¹ Besides TPGDA, a similar trend was observed in the photopolymerization of TMPTA. However, in the case of the monomer mixture, EB605, both AQD-NH2-4-based and AQD-NH2-5-based photoinitiating systems exhibited comparable performances, resulting in similar double bond conversions upon exposure to LED@455 nm. Notably, AQD-NH2-5 displayed better photoinitiation ability than AQD-NH2-4, attributed to its the extraordinary thermodynamic favorability.³¹ The exceptional photoinitiation ability of AQD-NH2-6 paved the way for its successful application in rapid optical 3D printing, underscoring its potential for advanced technological applications.^{31, 92}

Table 1.7. Final conversions of (a) EPOX and DVE-3, (b) TPGDA, (c) TMPTA, and (d) EB605 in the presence of AQD-NH₂-based photoinitiating systems upon exposure to LED@455 nm and LED@518 nm. (AQD-NH₂: 0.5 wt %; TEAOH, R-Br, or Iod1: 2 wt %; NVK: 3 wt %)^{30, 31}

Photoinitiating system	Conversion (%)									
	LED@455 nm					LED@518 nm				
	EPO X	DV E-3	TPGD A	TMPT A	EB60 5	EPO X	DV E-3	TPGD A	TMPT A	EB60 5
AQD-NH ₂ -4/Iod1	15	-	-	-	0	26	-	-	-	0
AQD-NH ₂ -4/Iod1/NVK	31	-	0	0	-	35	-	0	0	-
AQD-NH ₂ -4/TEAOH	-	-	0	-	0	-	-	0	-	0
AQD-NH ₂ -4/R-Cl	-	-	0	-	0	-	-	0	-	0
AQD-NH ₂ -4/TEAOH/R-Cl	-	-	-	-	-	-	-	-	-	-
AQD-NH ₂ -5/Iod1	66	78	7	-	53	67	74	6	-	51
AQD-NH ₂ -5/Iod1/NVK	73	-	14	33	42	80	-	15	12	-
AQD-NH ₂ -5/TEAOH	-	-	0	0	0	-	-	0	0	0
AQD-NH ₂ -5/R-Cl	-	-	0	0	0	-	-	0	0	0
AQD-NH ₂ -5/TEAOH/R-Cl	-	-	0	0	-	-	-	0	0	-
AQD-NH ₂ -6/Iod1	75	78	0	-	59	72	87	17	-	53
AQD-NH ₂ -6/Iod1/NVK	85	80	63	36	52	83	87	69	35	-
AQD-NH ₂ -6/TEAOH	-	-	66	37	54	-	-	48	31	35
AQD-NH ₂ -6/R-Cl	-	-	27	30	53	-	-	41	26	57
AQD-NH ₂ -6/TEAOH/R-Cl	-	-	82	47	65	-	-	78	44	57

The impact of N-substituent on the photophysical property and photoinitiation ability of AQD-NH₂ has been a key focus. The design and synthesis of symmetrically N-substituted AQD-NH₂ (AQD-NH₂-7~9)^{93, 94} have elucidated these effects, shedding light on their photoinitiation ability. With the N-substitution of alkyl and aromatic group, AQD-NH₂-7~9 exhibited a red shift compared to AQD-NH₂-5.^{30, 94} In most cases, AQD-NH₂-7 and AQD-NH₂-8 with alkyl N-substitutions exhibited better photoinitiation abilities compared to AQD-NH₂-9 with aromatic N-substitution (Figure 1.5a). As expected, the addition of NVK further improved the conversion of functional groups compared to the AQD-NH₂/Iod1 systems for both the cationic

polymerization of EPOX and the free radical polymerization of Bis-GMA/TEGDMA (70%/30%, wt). Moreover, the symmetric N-substituted AQD-NH₂ exhibited superior photoinitiation abilities in cationic polymerization compared to free radical polymerization (Figure 1.5a-b). Specifically, the AQD-NH₂-8/Iod1/NVK system achieved notable epoxide conversion of EPOX (56%) and double bond conversion of DVE-3 (80%) under the irradiation of LED@636 nm. In contrast, the double bond conversions of TMPTA and Bis-GMA/TEGDMA (70%/30%, wt) were only 20% and 50% under the same conditions (Figure 1.5b). Similar trends were observed for AQD-NH₂-7 and AQD-NH₂-9 (Figure 1.5a). Besides, the broad light absorption of AQD-NH₂-7~9^{93, 94} heightened their potential to photoinitiate polymerization under varied light sources. To identify their photoinitiation abilities under diverse lights, photopolymerization of EPOX and Bis-GMA/TEGDMA (70%/30%, wt) were involved under the irradiation of LED@392 nm, LED@455 nm, LED@518 nm, LED@594 nm, LED@636 nm and an infrared (IR) bulb (Figure 1.5c). Generally, AQD-NH₂-8/Iod1/NVK exhibited better photoinitiation abilities in cationic polymerization of EPOX than in free radical polymerization of Bis-GMA/TEGDMA (70%/30%, wt), except for the photopolymerizations upon exposure to LED@455 nm. Among the visible LEDs, the AQD-NH₂-8 exhibited the best photoinitiation ability in cationic polymerization under the irradiation of LED@594 nm and LED@636 nm, which can be ascribed to the complete overlap between the LED emission spectrum and its absorption maxima.⁹⁴ Regarding free radical polymerization of Bis-GMA/TEGDMA (70%/30%, wt), the photoinitiation ability of AQD-NH₂-8 appeared relatively similar under the investigated visible light irradiations. Notably, AQD-NH₂-8 exhibited limited yet discernible photoinitiation capacity under IR, enabling specific applications like deep curing.

Comparatively, amino-substituted AQD-NH₂ outperformed hydroxyl-substituted AQD-OH, and alkyl N-substituted AQD-NH₂ exhibited exceptional photoinitiation abilities, even under red light, surpassing unsubstituted AQD-NH₂ (AQD-NH₂-5) and phenyl N-substituted AQD-NH₂ (AQD-NH₂-9). Nonetheless, while these observations provide valuable insights, a deeper understanding of the molecular-scale mechanism governing substitution effects on photoinitiation abilities remains elusive. Therefore, further systematic investigations are warranted to uncover these mechanisms, facilitating the informed selection of AQD-derived photoinitiators, and offering a more comprehensive understanding of their potential applications.

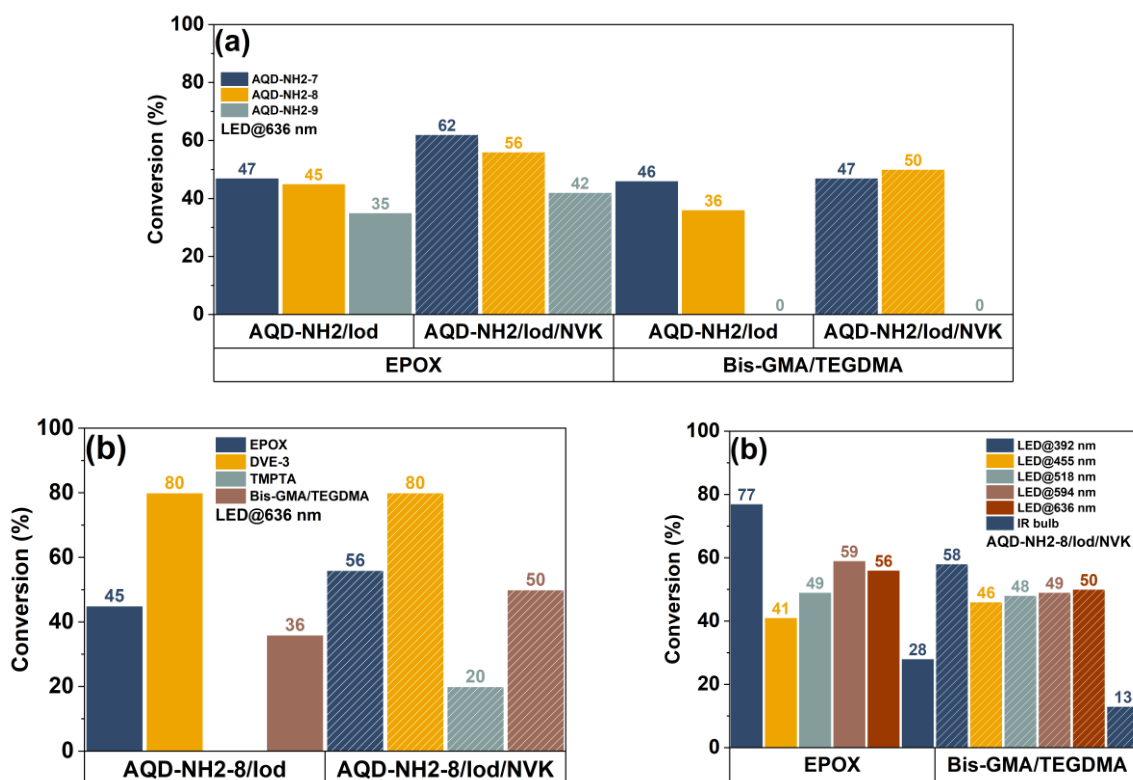


Figure 1.5. Final conversions of (a) EPOX and Bis-GMA/TEGDMA (70%/30%, wt) in the presence of AQD-NH2-based photoinitiating systems and (b) EPOX DVE-3, TMPTA and Bis-GMA/TEGDMA (70%/30%, wt) in the presence of AQD-NH2-8-based photoinitiating systems upon exposure to LED@636 nm; (c) EPOX and Bis-GMA/TEGDMA (70%/30%, wt) in the presence of AQD-NH2-8/lod1/NVK under irradiation from UV to IR bulb. (AQD-NH2: 0.5 wt %; lod1: 2 wt %; NVK: 3 wt %)⁹⁴

1.4.2 β -Carotene

In addition to the previously mentioned anthraquinone derivatives (AQDs), β -carotene has emerged as another effective photoinitiator for the fabrication of antibacterial or antifouling coatings.⁸⁸ The creation of coatings requires careful consideration, particularly due to the significant impact of shrinkage from free radical polymerization on product quality. To mitigate this concern, thiol-ene crosslinking¹⁰⁰ and ring-opening¹⁰¹ polymerization, known for their minimal shrinkage and tolerance to oxygen, have been extensively utilized in fabrication of coatings. Therefore, in the presence of a three-component photoinitiating system, β -carotene/bis(4-methylphenyl)iodonium hexafluorophosphate (lod2)/trimethylolpropane tris(3-mercaptopropionate) (TT) (1%/3%/6%, wt), ring-opening cationic polymerization and thiol-ene polymerization under irradiation of blue LEDs were investigated. Specifically, the epoxide conversion of dipentene dioxide (DPDO) in the presence of β -carotene/lod2 (1%/3%, wt) reached 58% upon exposure to LED@405 nm (100 mW cm⁻²) after 800 s. To incorporate with thiol-ene crosslinking, a compound consisting of epoxide, double bond (Lim: limonene 1,2-

epoxide), and a thiol component (TT) as crosslinker, were incorporated into the formula. The epoxy and double bond conversions were 84% and 50%, respectively, in the presence of β -carotene/Iod2/TT (1%/3%/6%, wt) under the irradiation of LED@405 nm (100 mW cm^{-2}). Moreover, the epoxy and double bond conversions of the DPDO/Lim blend (50%/50%, wt) were 68% and 50%, respectively. The formulation was further modified to fabricate antibacterial coating by including the active component, eugenol. The presence of eugenol, owing to its double bond, facilitated surface modification on the coatings (Table 1.4 and Figure 1.6). Notably, the addition of eugenol led to an enhancement in the epoxy, while reducing the double bond conversion. Specifically, in a DPDO/Lim/eugenol blend (50%/25%/25%, wt), the epoxy and lim- and eugenol-double bond conversions were 80%, 24%, and 20%, respectively. With the developed formula, an interpenetrating polymer network was successfully formed (Figure 1.6), and antibacterial coatings were fabricated on glass slides (Table 1.4). These coatings exhibited a better antibacterial effect on *E. coli* than *S. aureus*. Specifically, a reduction in bacterial count of 80% was observed for *E. coli*, while the reduction of *S. aureus* was 50% (Table 1.4 and Figure 1.4). Interestingly, the introduction of eugenol also imparted the waterproof properties to the coatings, evidenced by a water contact angle of 89.7° , surpassing the 71.2° angle exhibited by the coating without eugenol was. This enhancement in waterproofing represents an additional advantageous attribute of the modified coatings.

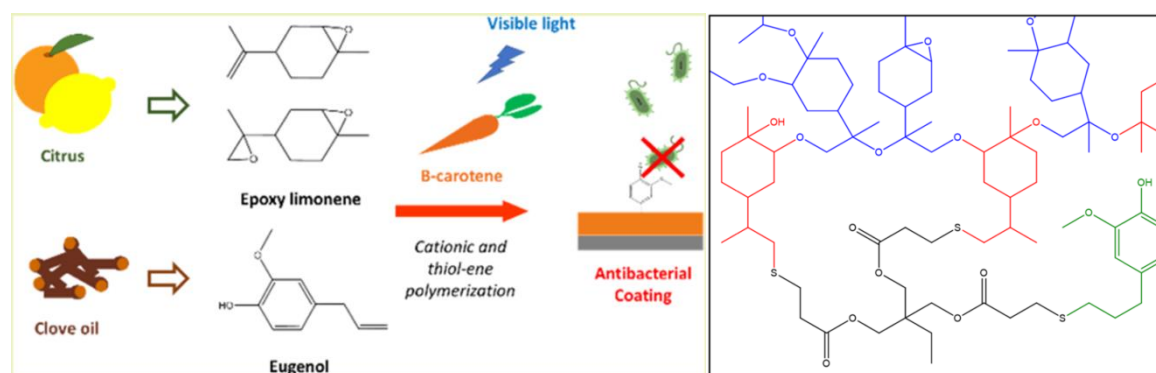
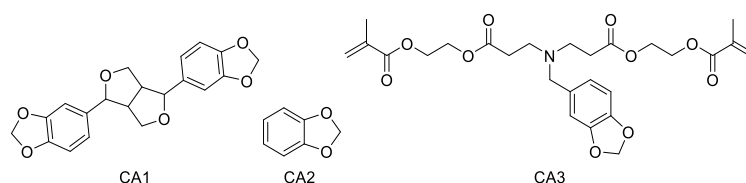


Figure 1.6. The synthesis of antibacterial coatings via photopolymerization of epoxy limonene and eugenol in the presence of a β -carotene-based photoinitiating system and the structure of interpenetrating polymer network. Adapted with permission from ⁸⁸. Copyright 2019 American Chemical Society.

1.5 Photoinitiators/coinitiators for Dental Restoration

Camphorquinone (CQ) in combination with amines has been a prevalent photoinitiating system employed in dental restoration practices.¹⁰² However, of the concern over aesthetic issues such as yellowing and discoloration arising from amines within dental fillings has led to a growing interest in developing amine-free photoinitiating systems. For instance, sulfonates and

sulfonates were reported as effective coiniciators capable of reducing yellowing in dental restorative materials.¹⁰³ Components like sodium 1-methyl 3sulfinooproanoate (NaMeSP), zinc benzylsulfinate (ZnBnS), or zinc isopropylsulfinate (ZniPrS) have facilitated the CQ-based photoinitiating systems to achieve double bond conversions exceeding 50% within 120 seconds under LED@477 nm (300 mW cm⁻²) irradiation.¹⁰³ However, the environmental impact posed by metal-based components necessitates the exploration of metal-free photoinitiating systems or photocatalysts.¹⁰⁴⁻¹⁰⁶ Cyclic acetals (CA), belonging to a family of heterocyclic compounds prevalent in nature, exhibit promising potential for amine-free and metal-free dental restorative formulas. For example, benzodioxole (BDO) ring system is widely found in natural products (e.g., sesamin, safrole, piperonal, etc.).¹⁰⁷ Meanwhile, a few cyclic acetals (Scheme 1.6) have been reported as efficient coiniciators incorporated with commercially available photoinitiators for free radical photopolymerization.¹⁰⁸⁻¹¹⁰ The newly developed CQ/cyclic acetals (e.g., sesamin, BDO, etc.) photoinitiating systems exhibited comparable photoinitiation abilities to the CQ/amine ones. Moreover, certain formulations have exhibited enhanced properties such as reduced yellowing and improved biocompatibility.¹¹¹⁻¹¹⁴



Scheme 1.6. Chemical structures of cyclic acetals (CAs) for the dental restorative formulas.

1.5.1 Cyclic acetals as coiniciators

The investigation into cyclic acetals (CA) as coiniciators in dental restoration has revealed promising outcomes, notably observed in the CQ/CA1 and CQ/CA2 photoinitiating systems. (Table 1.8).¹¹¹⁻¹¹⁴ The dental resin consisted of Bis-GMA/TEGDMA (70%/30%, wt), and the photopolymerizations were performed upon exposure to blue lights (400-500 nm). Compared to the commonly used photoinitiating system, CQ/ethyl 4-*N,N*-dimethylaminobenzoate (EDB), CQ/CA1 (also known as sesamin), and CQ/CA2 exhibited comparable photoinitiation abilities at the same weight percentage and/or mole percentage in terms of the final double bond conversions (Table 1.8). Interestingly, with the molar ratio of CQ/CA2 at 1/1 (1.66%/1.22%, wt), the double bond conversion of dental resin was significantly improved and could reach 90% (Table 1.8). Moreover, mechanical property assessments indicated comparable or even higher storage modulus at human body temperature for the polymers photoinitiated by CQ/CA1 and CQ/CA2.^{111, 112}

Furthermore, a polymerizable CA3 was designed and presented dual roles as a coinitiator and a diluent.¹¹⁴ The CQ/CA3 system, across varied concentrations, exhibited results comparable to CQ/EDB in terms of double bond conversions (Table 1.8). More interestingly, CA3, containing a polymerizable methacrylate group, could replace TEGDMA as a diluent, integrating within the polymer network. With the increase of CA3 content to 25 wt%, the double bond conversion of Bis-GMA/CA3 (75%/25%, wt) achieved 67.5%, and the storage modulus and T_g of the resultant polymer were similar to those of the polymer photoinitiated by CQ/EDB.¹¹⁴

Given the application of dental restorative materials within aqueous environments (i.e., oral cavity), factors such as water sorption and water solubility are pivotal considerations. Therefore, dental restorative materials with low water sorption and water solubility are favorable. Encouragingly, the water sorption and water solubility of the polymer photoinitiated by CQ/CA1 (0.5%/1%, wt) were comparable to the control group (CQ/EDB), and those initiated by CQ/CA3 (0.5%/25%, wt) even exhibited lower values than the control.^{111, 114} Aesthetic considerations in dentistry, particularly the yellowing effect associated with amine byproducts during photoreaction, have been addressed by the CQ/CA1 system, significantly reducing yellowing compared to the CQ/EDB system.¹¹¹ Moreover, CA1 also demonstrated favorable biocompatibility with L2959 cells after a 72-hr cell culture, suggesting its safety for oral cavity application.¹¹¹

Table 1.8. The composition of dental restorative formulas and their corresponding light intensity, double bond conversions, and maximum rates of photopolymerization of Bis-GMA/TEGDMA (70%/30%, wt).¹¹¹⁻¹¹⁴

Photoinitiating system	Concentration (wt%)	Light source	Double bond conversion	R_p (min^{-1})	Ref.
CQ/CA1	0.5%/1%	400-500 nm (100 mW cm^{-2})	~63%	~0.56	111
	0.5%/1.83%		71%	-	
CQ/EDB	0.5%/1%		75%	-	
CQ/CA2	0.5%/1%	400-500 nm (500 mW cm^{-2})	~70%	~0.016	112
	0.5%/2%		~72%	~0.024	
CQ/EDB	0.5%/1%		~72%	-	
CQ/CA2	1.66%/1.22%	400-550 nm (100 mW cm^{-2})	90%	1.51	113
CQ/CA3 ¹	0.5%/0.5%	400-500 nm (100 mW cm^{-2})	64.8%	0.91	114
	0.5%/1%		67%	-	
CQ/EDB ¹	0.5%/0.5%		66.4%	3.3	

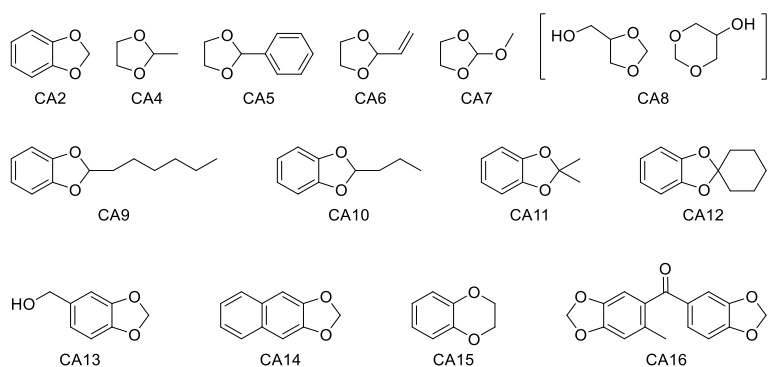
¹ Bis-GMA/TEGDMA ratio in the formulas was 75 wt%/25 wt%.

1.5.2 Substituent effect on photoinitiation ability

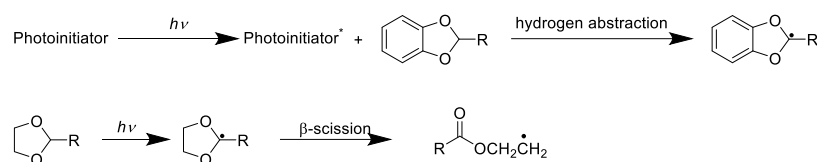
The utilization of cyclic acetals in dental restoration presents numerous advantages, prompting a deeper exploration into their photochemical mechanism and structural effects (Scheme 1.7) on their photoinitiation abilities. This examination aims to broaden the scope of cyclic acetals as coinitiators and enhance their photochemical activities. Within the *p*-chlorobenzophenone (CBP)-based photoinitiating systems, CBP/CAs (2%/4%, wt), the comparative evaluation of various cyclic acetals (CAs) highlighted CA2 as the most efficient among CAs (i.e., CA2 – CA8). Specifically, the photoinitiation abilities of the CBP/CA photoinitiating systems followed the order: CA2 > CA4 > CA5 > CA6 > CA8 > CA7, in terms of both final double bond conversions and the rates of polymerization of 1,6-hexanedioldiacrylate (HDDA).¹¹² The efficacies of CAs were further validated in three-component photoinitiating systems under the irradiation of an ion laser at 514 nm (100 mW cm⁻²).¹⁰⁹ According to the photochemical mechanism elucidated in Scheme 1.8, the substitution (R group) on C2 could influence the hydrogen abstraction and consequentially impact the photopolymerization. To comprehensively understand the effect of substituents on photoinitiation, a study on CA9-12 with selected substituents was conducted.^{110, 113} Notably, 2-monosubstituted BDO (i.e., CA9 and CA10) demonstrated exceptional photoinitiation abilities in terms of double bond conversion of HDDA due to their sensitivity to hydrogen abstraction.^{110, 113} In contrast, unlike the 2-monosubstituted BDOs, the oxidation of 2,2-disubstituted CAs primarily occurred on the benzene ring rather than the dioxole ring.¹¹⁰ Therefore, while the corresponding benzophenone (BP)-based photoinitiating systems with CA11 and CA12 presented adequate efficacy for the photopolymerization of HDDA, their polymerization rate was significantly compared to the 2-monosubstituted CAs. Specifically, the BP/CA9 and BP/CA10 systems achieved maximum polymerization within 2-min irradiation without any observable induction time, whereas the BP/CA11 and BP/CA12 systems initiated the photopolymerization only after ~20-second irradiation, and the double bond conversion of HDDA was slowly increased. Besides, the chain length of the substituent also affected the photochemical electron transfer between BP and CA. Shorter substituent chain lengths correlated with higher HDDA double bond conversions (CA2 > CA10 > CA9), thereby reducing the induction time. Additionally, the investigation encompassed CAs with substitution on other positions except for C2 (CA13-CA16) in both BP-based and CQ-based photoinitiating systems.¹⁰⁸ CA13 demonstrated photoinitiation ability comparable to CA2 for the photopolymerization of TMPTA in terms of both final double bond conversion and the rate of polymerization, underscoring the importance of the C2-substitution. However, CA14 and CA15 exhibited marginal improvement in the photoinitiation ability

compared to the BP alone and/or CQ alone systems, consistent with the quenching rate constants between excited BP and CA15 or CA16 (0.02 and 0).

Interestingly, CA9, CA10, and CA16 were found to function as one-component photoinitiating systems.^{108, 110} The free radicals formed via β -scission from the radical on C2 (Scheme 1.8). CA9 and CA10 as photoinitiators demonstrated sufficient photoinitiation abilities in polymerizing HDDA, comparable to CA2 in terms of double bond conversion, but weaker than BP. Meanwhile, in their roles as coinitiators, CA10 exhibited superior photoinitiation abilities compared to CA9. In contrast, CA16 exhibited better photoinitiation ability than BP in terms of both double bond conversion and rate of polymerization of TMPTA under UV irradiation.¹⁰⁸



Scheme 1.7. Chemical structures of cyclic acetals for CQ-based photoinitiating systems.

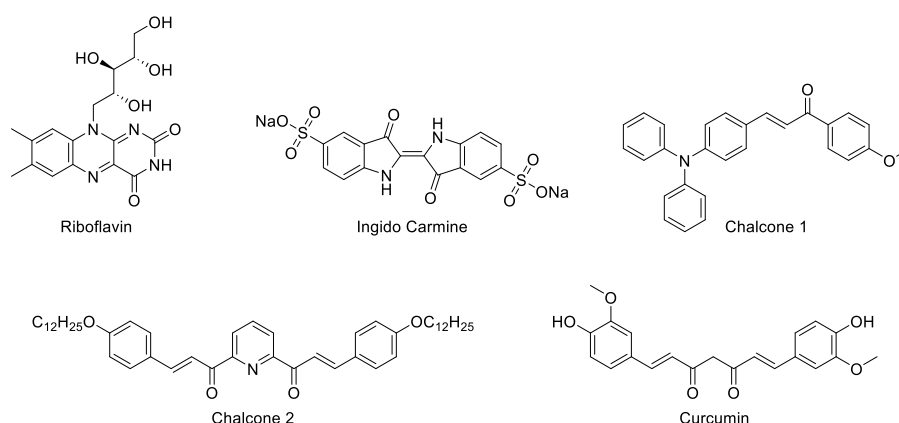


Scheme 1.8. The proposed photochemical mechanism between photoinitiator and cyclic acetal, or cyclic acetals alone under irradiation.

1.6 Photoinitiator Candidates for Other Medical Applications

In addition to its profound contributions to tissue regeneration, antifouling/antibacterial coatings, and dental restoration, photopolymerization has been leveraged to great effect in a wide range of medical devices.¹¹⁵ For instance, microneedles,^{116, 117} organ-on-a-chip,¹¹⁸ biosensors¹¹⁹⁻¹²¹, and bio mimic microchips¹²² have been fabricated via photopolymerization technology. However, their reliance on photoinitiators such as phosphine oxide, N-phenylglycine (NPG), 2,20-dimethoxy phenyl acetophenone (Irgacure 651), isopropylthioxanthone (ITX), and others raises concerns about their biocompatibility, limiting their practical application in clinical

settings. Despite ITX being a xanthone derivative, a core component found in various natural compounds,^{123, 124} its presence is associated with adverse effects on human health, including genotoxicity and other health-related concerns.¹²⁵ Recognizing these limitations, the forthcoming section endeavors to introduce the naturally derived photoinitiators (Scheme 1.9: riboflavin, chalcone derivatives, an indigo derivative, and curcumin which have found application in diverse medical contexts.



Scheme 1.9. Chemical structures of the introduced naturally derived photoinitiations.

1.6.1 Microneedle initiated by riboflavin

The fabrication of microneedles, an easy to use medical device, necessitates meticulous attention to factors such as mechanical strength, precision, and resolution, particularly considering the presence of physical barriers. Vat polymerization technology has been employed in the fabrication of microneedles.¹¹⁷ However, challenges persist due to the residual photoinitiator causing undesired damage through migration. In addressing this concern, employing inherently biocompatible photoinitiator emerges as a promising solution. Riboflavin has demonstrated excellent capability in tissue engineering as a photoinitiator, thanks to its inherent visible light sensitivity and natural origin. Its role in photoinitiating silk fibroin has been highlighted in our previous discussion on artificial cornea development (Section 1.3.2).⁶⁴ Silk fibroin, due to its versatile applications, serves not only in ocular prostheses but also in the fabrication of microneedles used in drug delivery.^{126, 127} Therefore, a silk fibroin microneedle patch produced through riboflavin-photoinitiated polymerization has been successfully achieved (Figure 1.7).¹²⁸

As discussed in Section 2.2, the 3D printability should be carefully considered because the overcuring or damp materials considerably impact the strength and resolution of resulting

microneedles. A total pixel of $48\mu\text{m} \times 48\mu\text{m}$ was printed to define the printability and the corresponding resolution. A high-resolution pattern necessitated a minimum of 2-by-2 pixels requiring 3-minute irradiation. Using the correlation between resolution and irradiation time, microneedles were fabricated via 3D printing photoinitiated by riboflavin. However, dehydration led to microneedle deformation, resulting in roughly 50% shrinkage in both horizontal and vertical directions. Furthermore, unlike the horizontal direction, the vertical deformation exhibited a pronounced correlation with the layer thickness of the 3D printing settings. Specifically, augmenting the subsequent layered thickness escalated vertical shrinkage. While shrinkage impacted microneedle topology, diminishing the function of drug delivery, horizontal deformation of the microneedles facilitates sharpening, enhancing penetration performance. Therefore, controlling vertical shrinkage via 3D printing layer thickness manipulation determined microneedle functionality.

The silk fibroin microneedle patch fabricated via 3D printing in the presence of riboflavin demonstrated exceptional flexibility (Figure 1.7A). Furthermore, the evaluation of the drug delivery was carried out via *in vitro* penetration of a model drug, rhodamine B, employing a microneedle patch (Figure 1.1B-D). Specifically, after microneedle penetration, evident puncture impressions were observed under natural light (Figure 1.1C), and the fluorescence of rhodamine B appeared under UV irradiation (Figure 1.1D).

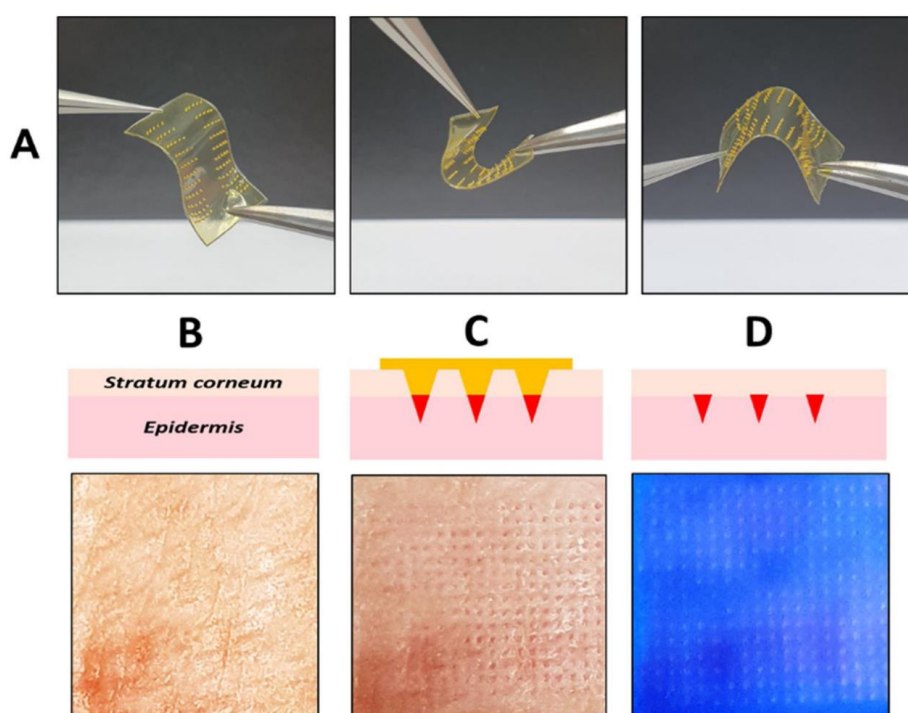


Figure 1.7. Photographs of (A) the fabricated microneedle patch via 3D printing of silk fibroin in the presence of riboflavin, and swine skin (B) before and (C) after penetration, and (D) fluorescence of rhodamine B in the swine skin under UV illumination. Reproduced with permission from ¹²⁸. Copyright 2020 The Korean Society of Industrial and Engineering Chemistry.

1.6.2 Shape memory polymers initiated by chalcone derivatives and an indigo derivative

Shape memory polymers have drawn great attention due to their various applications to electronic devices, aerospace engineering, biomedical applications, etc.¹²⁹⁻¹³¹ Their origami capabilities endow materials with unique smart responses upon stimuli (e.g., light, heat, moisture, pressure, electricity, etc.).¹³² The integration of 3D printing technology into the development of shape memory polymers has further enhanced their customizability and versatility.¹³³⁻¹³⁶ Particularly in medical device applications, the biocompatibility of these polymers plays a crucial role. Chalcone and indigo carmine are natural substances. Herein, a series of chalcone derivatives and an indigo derivative (Scheme 1.9) have been well-investigated as photoinitiators for the fabrication of shape memory polymers.¹³⁷⁻¹³⁹

Chalcone 1/Iod (1.5%/1.5%, wt) and chalcone 2/Iod/ethyl 4-dimethylaminobenzoate (EDB) (1.5%/1.5%/1.5%, wt) were two photoinitiating systems used to produce water-stimulated shape memory hydrogels (Figure 1.8). Under the irradiation of LED@405 nm, chalcone 1/Iod exhibited a remarkable 94% double bond conversion of PEGDA in 2 mm thickness samples. The excellent photoinitiation ability of chalcone 1/Iod for thick samples endows the capability of one-step production of thick designs. Conversely, chalcone 2/Iod/EDB resulted in only 62% conversion upon exposure to LED@405 nm, which significantly improved to 86% when LED@375 nm was used. The chalcone derivatives (i.e., chalcone 1 and 2) demonstrated high conversion of PEGDA and were employed in producing shape memory polymers. Specifically, the cross-shape structures photoinitiated by chalcone 1/Iod (Figure 1.8A2) and chalcone 2/Iod/EDB (Figure 1.8B2) exhibited symmetrical folding after immersion in water for 1 min (Figure 1.8A3 and B3). Subsequent 100-second dehydration at 100 °C resulted in the recovery of these cross-shape structures to their original shapes (Figure 1.8A4 and B4). Further dehydration led to the invertedly curled cross structures (Figure 1.8 A5 and B5), which reverted to their original shapes under ambient conditions (Figure 1.8A6 and B6). Water and heat stimuli demonstrated excellent efficacy for the chalcone derivatives-photoinitiated poly(ethylene glycol) (PEG) hydrogels.

In addition to chalcone derivatives, the exceptional water-soluble visible-light-sensitive photoinitiator, indigo carmine, was explored and investigated.¹³⁹ Under violet light, PEGDA

achieved complete conversion within a short duration. Interestingly, the introduction of NaOH manipulated the photoinitiation ability of indigo carmine. Specifically, the addition of hydroxides created the basic environment and facilitated the formation of the leuco form of indigo carmine. In addition, it improved the solubility of indigo carmine in the designed hydrogel formula, thus benefiting the photoinitiation ability. The exceptional photoinitiation ability endows the indigo carmine-involved formula with valuable 3D printability. A seashell-shaped structure was 3D printed to validate the shape memory behavior of the designed 3D resin (Figure 1.8C). Varied thicknesses of the designed model resulted in differences in crosslinking densities (Figure 1.8C-a), impacting the swelling ratio. Upon hydration and dehydration, the seashell exhibited reversible changes in curvature (Figure 1.8C-b).

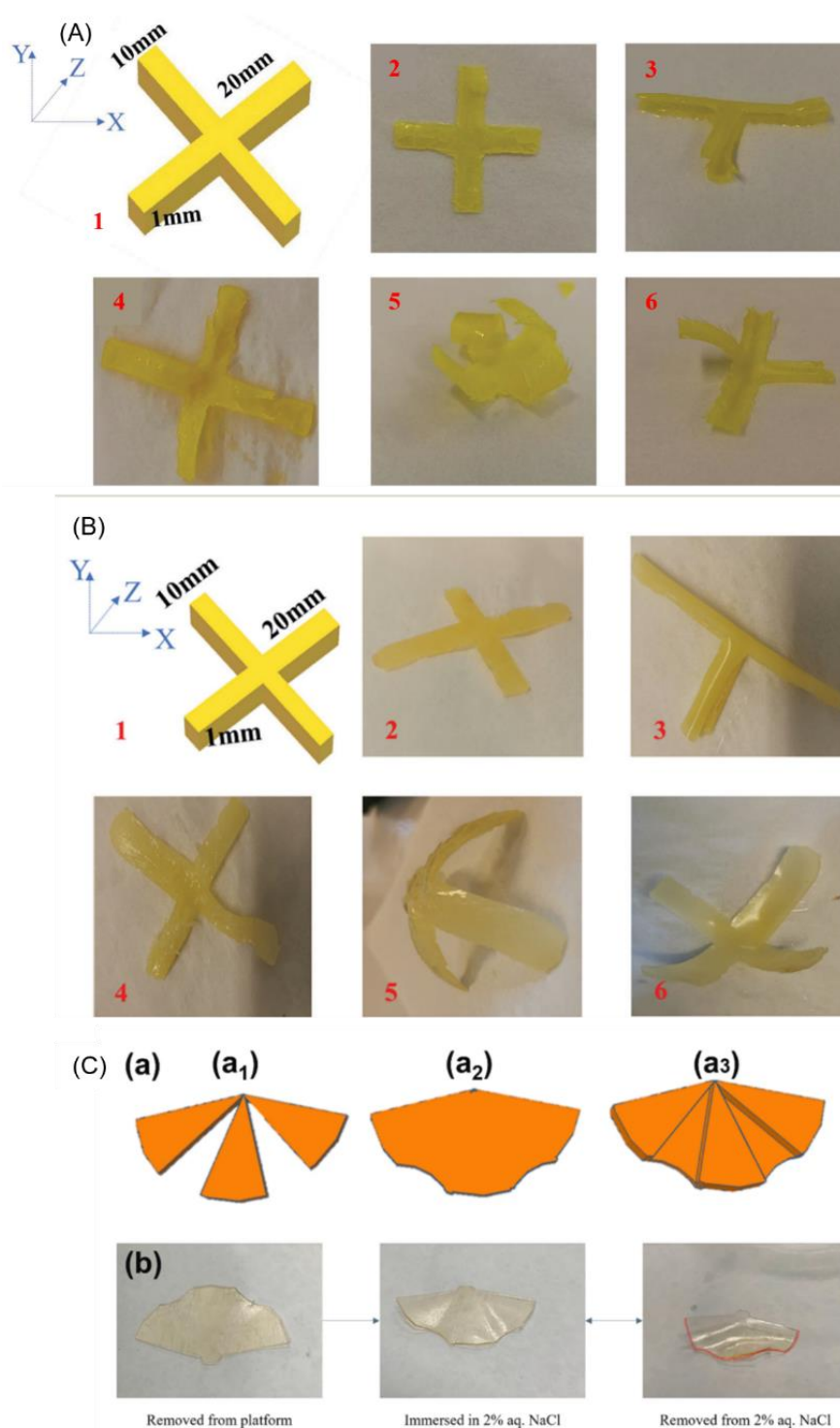


Figure 1.8. (A-B) Cross-shape structure (1) mold and (2-6) shape memory behavior upon stimuli: (2) after 1-min photopolymerization, (3) after 1-min immersion into water, (4) after 1-min dehydration at 100 °C, (5) after 10-min dehydration at 100 °C, and (6) after 10-min exposure to open air under ambient condition; cross-shape structure fabricated using (A) chalcone 1/Iod (1.5%/1.5%, wt) and (B) chalcone 2/Iod/EDB (1.5%/1.5%/1.5%, wt). (C) The (a) design and (b) the shape memory behavior of the 3D printed seashell structure upon hydration and dehydration under ambient conditions. Adapted with permission from ¹³⁷⁻¹³⁹. Copyright 2020 The Royal Society of Chemistry, Copyright 2021 The Royal Society of Chemistry and the Chinese Chemical Society, and Copyright 2022 Elsevier B.V.

1.7 Conclusion and current challenges

The evolution of photopolymerization technology has been rapid, particularly within the manufacturing industry, where it finds prominent applications in decoration and parts manufacturing, such as aerospace engineering and mechanical engineering. However, the scope of its practical medical applications remains limited, primarily focused on dental restoration. To expand the utility of photopolymerization within medical field, it is imperative to ascertain the safety of photopolymerizable formulas. While significant research has targeted the monomer utilized in bioink formulas,^{6, 7} the subsequent development of biocompatible photoinitiators is imperative. Leveraging the abundance of safe light-sensitive compounds in nature, numerous naturally occurring and naturally derived photoinitiators have been developed as photoinitiator candidates for medical applications. This review provides a comprehensive summary of these photoinitiators' benefits in medical device applications and their corresponding functional evaluations.

A straightforward strategy of safe photoinitiator development involves the direct evaluation of naturally occurring biocompatible compounds. Riboflavin, for instance, stands as a versatile naturally occurring photoinitiator used in diverse medical applications, including regenerative medicines and microneedles. Another popular strategy involves establishing covalent associations between macromolecular natural products and commercially available photoinitiators such as hyaluronan and BAPO or TPO. These macrophotoinitiators have demonstrated excellent photoinitiation abilities and outstanding biocompatibility. The third strategy revolves around the development of small molecular naturally derived compounds (e.g., carbazole derivatives, anthraquinone derivatives, etc.). However, further assessments, particularly in terms of biocompatibility, are critical for their application in medical contexts.

Moreover, further optimization of formulas and subsequent thorough safety assessments are essential steps toward producing medical devices. Understanding the structural effect on photoinitiation ability, as discussed in Sections 1.3.3.2, 1.4.1.2, and 1.5.2, is crucial. Knowledge of the substituent effect on photoinitiation ability will guide future endeavors in designing naturally derived photoinitiators within an efficient framework. Continued research and development in this direction will contribute substantially to expanding the utility of photopolymerization in the medical domain.

While numerous naturally derived compounds have been explored as efficient photoinitiators,^{22-24, 27, 28, 34, 140-142} many challenges of photocurable materials remain in medical contexts. First, there is still synthetic pollution brought by naturally derived photoinitiators.

Specifically, most of the aforementioned photoinitiators are modified with synthetic compounds. Second, most of the photopolymerization in the presence of those natural photoinitiators happened under near-UV irradiation, causing health issues. Third, there is limited natural photoinitiators for the fabrication of waterborne materials.

1.8 Objectives and thesis outline

To overcome the abovementioned limitations, the following objectives guided the present thesis directions. First, identify naturally occurring photoinitiators from a broader plant family. Second, develop visible-light sensitive natural photoinitiators. Third, employ natural photoinitiators in waterborne materials.

In the present thesis, four natural biocompatible dyes have been developed as biocompatible photoinitiators sensitive to visible light. These natural dyes can be extracted from berries, citrus, pomegranate, or *Indigofera*.¹⁴³⁻¹⁴⁶ They are either antioxidant, anti-inflammatory substance, or food colorant.^{144, 147-151} Thanks to these reported effects, quercetin and morin from berries (Chapter 2), naringin from citrus (Chapter 3), ellagic acid from pomegranate (Chapter 4), and indigo carmine from *Indigofera* (Chapter 5) are inherently biocompatibilities, and the further safety assessment of them is unnecessary. Therefore, they have potential for direct use without further biocompatibility evaluation. Meanwhile, the direct use of these natural compounds as photoinitiators can prevent pollution from synthesis process.

Quercetin and morin discussed in Chapter 2 demonstrated their photoinitiation abilities under violet light and expanded the scope of natural photoinitiator. However, these two natural compounds were only employed in hydrophobic monomer systems. To resolve this problem, another flavone derivative, naringin in Chapter 3, was developed as a water-soluble natural photoinitiator. The strategy of hydroxyl group ionization by adding alkane can potentially enable photoinitiators with hydroxyl groups to function in water/photocurable polymer blends. To expand the scope of natural photoinitiator candidate, a dark plant extract, ellagic acid, in Chapter 4 demonstrated its excellent photoinitiation ability in water/photocurable polymer blends. This polyphenol compound demonstrated its dual-role of photoinitiator and photoabsorber, which resulted in a highly precise 3D printing. However, the extra strong alkanes may also cause undesired safety issues. A natural sodium salt dye, indigo carmine, in Chapter 5 could significantly reduce the addition of alkane. In addition, indigo carmine also demonstrated its photoinitiation ability under green light, further reducing the capable health hazard brought by near UV.

In the following chapters, their photoinitiation abilities under visible light, 3D printability of the developed 3D resins in the presence of these photoinitiator candidates, and/or further applications will be discussed.

1.9 References:

- (1) Setoura, K.; Ito, S. Optical manipulation in conjunction with photochemical/photothermal responses of materials. *J. Photochem. Photobiol., C* **2022**, *52*, 100536.
- (2) Pierau, L.; Elian, C.; Akimoto, J.; Ito, Y.; Caillol, S.; Versace, D.-L. Bio-sourced monomers and cationic photopolymerization—The green combination towards eco-friendly and non-toxic materials. *Prog. Polym. Sci.* **2022**, *127*, 101517.
- (3) Lai, H.; Peng, X.; Li, L.; Zhu, D.; Xiao, P. Novel monomers for photopolymer networks. *Prog. Polym. Sci.* **2022**, *128*, 101529.
- (4) Wu, C.; Corrigan, N.; Lim, C. H.; Liu, W.; Miyake, G.; Boyer, C. Rational Design of Photocatalysts for Controlled Polymerization: Effect of Structures on Photocatalytic Activities. *Chem. Rev.* **2022**, *122* (6), 5476-5518.
- (5) Yu, C.; Schimelman, J.; Wang, P.; Miller, K. L.; Ma, X.; You, S.; Guan, J.; Sun, B.; Zhu, W.; Chen, S. Photopolymerizable Biomaterials and Light-Based 3D Printing Strategies for Biomedical Applications. *Chem. Rev.* **2020**, *120* (19), 10695-10743.
- (6) Lim, K. S.; Galarraga, J. H.; Cui, X.; Lindberg, G. C. J.; Burdick, J. A.; Woodfield, T. B. F. Fundamentals and Applications of Photo-Cross-Linking in Bioprinting. *Chem. Rev.* **2020**, *120* (19), 10662-10694.
- (7) Lee, M.; Rizzo, R.; Surman, F.; Zenobi-Wong, M. Guiding Lights: Tissue Bioprinting Using Photoactivated Materials. *Chem. Rev.* **2020**, *120* (19), 10950-11027.
- (8) Lai, H.; Zhang, J.; Xing, F.; Xiao, P. Recent advances in light-regulated non-radical polymerisations. *Chem. Soc. Rev.* **2020**, *49* (6), 1867-1886.
- (9) Jung, K.; Corrigan, N.; Ciftci, M.; Xu, J.; Seo, S. E.; Hawker, C. J.; Boyer, C. Designing with Light: Advanced 2D, 3D, and 4D Materials. *Adv. Mater.* **2020**, *32* (18), e1903850.
- (10) You, J.; Fu, H.; Zhao, D.; Hu, T.; Nie, J.; Wang, T. Flavonol dyes with different substituents in photopolymerization. *J. Photochem. Photobiol., A* **2020**, *386*, 112097.
- (11) Wang, Y.; Cui, H.; Esworthy, T.; Mei, D.; Wang, Y.; Zhang, L. G. Emerging 4D Printing Strategies for Next-Generation Tissue Regeneration and Medical Devices. *Adv. Mater.* **2022**, *34* (20), e2109198.
- (12) Fairbanks, B. D.; Schwartz, M. P.; Halevi, A. E.; Nuttelman, C. R.; Bowman, C. N.; Anseth, K. S. A Versatile Synthetic Extracellular Matrix Mimic via Thiol-Norbornene Photopolymerization. *Adv. Mater.* **2009**, *21* (48), 5005-5010.
- (13) Bao, Y.; Paunović, N.; Leroux, J. C. Challenges and Opportunities in 3D Printing of Biodegradable Medical Devices by Emerging Photopolymerization Techniques. *Adv. Funct. Mater.* **2022**, *32* (15), 2109864.
- (14) Chen, Y.; Zhang, J.; Liu, X.; Wang, S.; Tao, J.; Huang, Y.; Wu, W.; Li, Y.; Zhou, K.; Wei, X.; et al. Noninvasive in vivo 3D bioprinting. *Sci. Adv.* **2020**, *6* (23), eaba7406.
- (15) Anandakrishnan, N.; Ye, H.; Guo, Z.; Chen, Z.; Mentkowski, K. I.; Lang, J. K.; Rajabian, N.; Andreadis, S. T.; Ma, Z.; Spornyak, J. A.; et al. Fast Stereolithography Printing of Large-Scale Biocompatible Hydrogel Models. *Adv. Healthcare Mater.* **2021**, *10* (10), e2002103.
- (16) He, Y. J.; Santana, M. F.; Staneviciute, A.; Pimentel, M. B.; Yang, F.; Goes, J.; Kawaji, K.; Vaicik, M. K.; Abdulhadi, R.; Hibino, N.; et al. Cell-Laden Gradient Hydrogel Scaffolds for Neovascularization of Engineered Tissues. *Adv. Healthcare Mater.* **2021**, *10* (7), e2001706.
- (17) Winterwerber, P.; Harvey, S.; Ng, D. Y. W.; Weil, T. Photocontrolled Dopamine Polymerization on DNA Origami with Nanometer Resolution. *Angew. Chem., Int. Ed.* **2020**, *59* (15), 6144-6149.

- (18) Bernal, P. N.; Delrot, P.; Loterie, D.; Li, Y.; Malda, J.; Moser, C.; Levato, R. Volumetric Bioprinting of Complex Living-Tissue Constructs within Seconds. *Adv. Mater.* **2019**, *31* (42), e1904209.
- (19) Ji, X.; Liang, J.; Liu, J.; Shen, J.; Li, Y.; Wang, Y.; Jing, C.; Mabury, S. A.; Liu, R. Occurrence, Fate, Human Exposure, and Toxicity of Commercial Photoinitiators. *Environ. Sci. Technol.* **2023**, *57* (32), 11704-11717.
- (20) Popal, M.; Volk, J.; Leyhausen, G.; Geurtsen, W. Cytotoxic and genotoxic potential of the type I photoinitiators BAPO and TPO on human oral keratinocytes and V79 fibroblasts. *Dent. Mater.* **2018**, *34* (12), 1783-1796.
- (21) *Photopolymerization: Fundamentals and Applications*; American Chemical Society, 1997.
- (22) Peng, X.; Zhu, D.; Xiao, P. Naphthoquinone derivatives: Naturally derived molecules as blue-light-sensitive photoinitiators of photopolymerization. *Eur. Polym. J.* **2020**, *127*, 109569.
- (23) Zhu, D.; Peng, X.; Xiao, P. Penta - Hydroxy Flavones - Based Photoinitiating Systems for Free Radical, Cationic, and Thiol - Ene Polymerization upon Exposure to Mild Blue LEDs. *Macromol. Mater. Eng.* **2021**, *306* (6), 2100059.
- (24) Al Mousawi, A.; Garra, P.; Dumur, F.; Graff, B.; Fouassier, J. P.; Lalevée, J. Flavones as natural photoinitiators for light mediated free - radical polymerization via light emitting diodes. *J. Polym. Sci.* **2020**, *58* (2), 254-262.
- (25) Kim, S.-h.; Chu, C.-C. Visible light induced dextran-methacrylate hydrogel formation using (-)-riboflavin vitamin B2 as a photoinitiator and L-arginine as a co-initiator. *Fibers Polym.* **2009**, *10* (1), 14-20.
- (26) Zhao, J.; Lalevée, J.; Lu, H.; MacQueen, R.; Kable, S. H.; Schmidt, T. W.; Stenzel, M. H.; Xiao, P. A new role of curcumin: as a multicolor photoinitiator for polymer fabrication under household UV to red LED bulbs. *Polym. Chem.* **2015**, *6* (28), 5053-5061.
- (27) Wu, C.; Shanmugam, S.; Xu, J.; Zhu, J.; Boyer, C. Chlorophyll a crude extract: efficient photo-degradable photocatalyst for PET-RAFT polymerization. *Chem. Commun.* **2017**, *53* (93), 12560-12563.
- (28) Shanmugam, S.; Xu, J.; Boyer, C. Utilizing the electron transfer mechanism of chlorophyll a under light for controlled radical polymerization. *Chem. Sci.* **2015**, *6* (2), 1341-1349.
- (29) Wang, J.; Stanic, S.; Altun, A. A.; Schwentenwein, M.; Dietliker, K.; Jin, L.; Stampfl, J.; Baudis, S.; Liska, R.; Grutzmacher, H. A highly efficient waterborne photoinitiator for visible-light-induced three-dimensional printing of hydrogels. *Chem. Commun.* **2018**, *54* (8), 920-923.
- (30) Zhang, J.; Lalevée, J.; Hill, N. S.; Launay, K.; Morlet-Savary, F.; Graff, B.; Stenzel, M. H.; Coote, M. L.; Xiao, P. Disubstituted Aminoanthraquinone-Based Multicolor Photoinitiators: Photoinitiation Mechanism and Ability of Cationic Polymerization under Blue, Green, Yellow, and Red LEDs. *Macromolecules* **2018**, *51* (20), 8165-8173.
- (31) Zhang, J.; Launay, K.; Hill, N. S.; Zhu, D.; Cox, N.; Langley, J.; Lalevée, J.; Stenzel, M. H.; Coote, M. L.; Xiao, P. Disubstituted Aminoanthraquinone-Based Photoinitiators for Free Radical Polymerization and Fast 3D Printing under Visible Light. *Macromolecules* **2018**, *51* (24), 10104-10112.
- (32) Zhang, J.; Lalevée, J.; Zhao, J.; Graff, B.; Stenzel, M. H.; Xiao, P. Dihydroxyanthraquinone derivatives: natural dyes as blue-light-sensitive versatile photoinitiators of photopolymerization. *Polym. Chem.* **2016**, *7* (47), 7316-7324.
- (33) Lai, H.; Zhu, D.; Peng, X.; Zhang, J.; Lalevée, J.; Xiao, P. N-Aryl glycines as versatile initiators for various polymerizations. *Polym. Chem.* **2021**, *12* (13), 1991-2000.
- (34) Al Mousawi, A.; Garra, P.; Schmitt, M.; Toufaily, J.; Hamieh, T.; Graff, B.; Fouassier, J. P.; Dumur, F.; Lalevée, J. 3-Hydroxyflavone and N-Phenylglycine in High Performance Photoinitiating Systems for 3D Printing and Photocomposites Synthesis. *Macromolecules* **2018**, *51* (12), 4633-4641.
- (35) Chartrain, N. A.; Williams, C. B.; Whittington, A. R. A review on fabricating tissue scaffolds using vat photopolymerization. *Acta Biomater.* **2018**, *74*, 90-111.

- (36) Zielinska, D.; Fisch, P.; Moehrlen, U.; Finkielstein, S.; Linder, T.; Zenobi-Wong, M.; Biedermann, T.; Klar, A. S. Combining bioengineered human skin with bioprinted cartilage for ear reconstruction. *Science Advances* **2023**, *9* (40), eadh1890.
- (37) Jia, H.; Flommersfeld, J.; Heymann, M.; Vogel, S. K.; Franquelim, H. G.; Bruckner, D. B.; Eto, H.; Broedersz, C. P.; Schwille, P. 3D printed protein-based robotic structures actuated by molecular motor assemblies. *Nature Materials* **2022**, *21* (6), 703-709.
- (38) Wang, Y.; Wang, P.; Qin, J. Human Organoids and Organs-on-Chips for Addressing COVID-19 Challenges. *Advanced Science* **2022**, *9* (10), e2105187.
- (39) Enrico, A.; Voulgaris, D.; Ostmans, R.; Sundaravadivel, N.; Moutaux, L.; Cordier, A.; Niklaus, F.; Herland, A.; Stemme, G. 3D Microvascularized Tissue Models by Laser-Based Cavitation Molding of Collagen. *Advanced Materials* **2022**, *34* (11), e2109823.
- (40) Cao, X.; Ashfaq, R.; Cheng, F.; Maharjan, S.; Li, J.; Ying, G.; Hassan, S.; Xiao, H.; Yue, K.; Zhang, Y. S. A Tumor-on-a-Chip System with Bioprinted Blood and Lymphatic Vessel Pair. *Advanced Functional Materials* **2019**, *29* (31), 1807173.
- (41) Gold, K.; Gaharwar, A. K.; Jain, A. Emerging trends in multiscale modeling of vascular pathophysiology: Organ-on-a-chip and 3D printing. *Biomaterials* **2019**, *196*, 2-17.
- (42) Mannoor, M. S.; Jiang, Z.; James, T.; Kong, Y. L.; Malatesta, K. A.; Soboyejo, W. O.; Verma, N.; Gracias, D. H.; McAlpine, M. C. 3D printed bionic ears. *Nano Letters* **2013**, *13* (6), 2634-3639.
- (43) Lee, J. W.; Kang, K. S.; Lee, S. H.; Kim, J. Y.; Lee, B. K.; Cho, D. W. Bone regeneration using a microstereolithography-produced customized poly(propylene fumarate)/diethyl fumarate photopolymer 3D scaffold incorporating BMP-2 loaded PLGA microspheres. *Biomaterials* **2011**, *32* (3), 744-752.
- (44) Fraser, J. R.; Laurent, T. C.; Laurent, U. B. Hyaluronan: its nature, distribution, functions and turnover. *J. Intern. Med.* **1997**, *242* (1), 27-33.
- (45) Ashoori, M.; Saedisomeolia, A. Riboflavin (vitamin B(2)) and oxidative stress: a review. *Br. J. Nutr.* **2014**, *111* (11), 1985-1991.
- (46) Arbiser, J. L.; Govindarajan, B.; Battle, T. E.; Lynch, R.; Frank, D. A.; Ushio-Fukai, M.; Perry, B. N.; Stern, D. F.; Bowden, G. T.; Liu, A.; et al. Carbazole is a naturally occurring inhibitor of angiogenesis and inflammation isolated from antipsoriatic coal tar. *J. Invest. Dermatol.* **2006**, *126* (6), 1396-1402.
- (47) Rossi, C. A.; Flaibani, M.; Blaauw, B.; Pozzobon, M.; Figallo, E.; Reggiani, C.; Vitiello, L.; Elvassore, N.; De Coppi, P. In vivo tissue engineering of functional skeletal muscle by freshly isolated satellite cells embedded in a photopolymerizable hydrogel. *FASEB J.* **2011**, *25* (7), 2296-2304.
- (48) Tromayer, M.; Gruber, P.; Markovic, M.; Rosspeintner, A.; Vauthey, E.; Redl, H.; Ovsianikov, A.; Liska, R. A biocompatible macromolecular two-photon initiator based on hyaluronan. *Polym. Chem.* **2017**, *8* (2), 451-460.
- (49) Chang, H. K.; Yang, D. H.; Ha, M. Y.; Kim, H. J.; Kim, C. H.; Kim, S. H.; Choi, J. W.; Chun, H. J. 3D printing of cell-laden visible light curable glycol chitosan bioink for bone tissue engineering. *Carbohydr. Polym.* **2022**, *287*, 119328.
- (50) Arakawa, C.; Ng, R.; Tan, S.; Kim, S.; Wu, B.; Lee, M. Photopolymerizable chitosan-collagen hydrogels for bone tissue engineering. *J. Tissue Eng. Regener. Med.* **2017**, *11* (1), 164-174.
- (51) Zheng, Y. C.; Zhao, Y. Y.; Zheng, M. L.; Chen, S. L.; Liu, J.; Jin, F.; Dong, X. Z.; Zhao, Z. S.; Duan, X. M. Cucurbit[7]uril-Carbazole Two-Photon Photoinitiators for the Fabrication of Biocompatible Three-Dimensional Hydrogel Scaffolds by Laser Direct Writing in Aqueous Solutions. *ACS Appl. Mater. Interfaces* **2019**, *11* (2), 1782-1789.
- (52) Gao, W.; Chao, H.; Zheng, Y. C.; Zhang, W. C.; Liu, J.; Jin, F.; Dong, X. Z.; Liu, Y. H.; Li, S. J.; Zheng, M. L. Ionic Carbazole-Based Water-Soluble Two-Photon Photoinitiator and the Fabrication of Biocompatible 3D Hydrogel Scaffold. *ACS Appl. Mater. Interfaces* **2021**, *13* (24), 27796-27805.

- (53) Zhu, D.; Zhang, J.; Lalevée, J.; Xiao, P. Chapter 1 Novel Photoinitiating Systems for 3D Printing. In *3D Printing with Light*, Xiao, P., Zhang, J. Eds.; De Gruyter, 2021; pp 1-48.
- (54) Wang, J.; Chiappone, A.; Roppolo, I.; Shao, F.; Fantino, E.; Lorusso, M.; Rentsch, D.; Dietliker, K.; Pirri, C. F.; Grutzmacher, H. All-in-One Cellulose Nanocrystals for 3D Printing of Nanocomposite Hydrogels. *Angew. Chem., Int. Ed.* **2018**, *57* (9), 2353-2356.
- (55) Rodgers, Z. L.; Hughes, R. M.; Doherty, L. M.; Shell, J. R.; Molesky, B. P.; Brugh, A. M.; Forbes, M. D.; Moran, A. M.; Lawrence, D. S. B12-mediated, long wavelength photopolymerization of hydrogels. *J. Am. Chem. Soc.* **2015**, *137* (9), 3372-3378.
- (56) Batchelor, R. R.; Kwandou, G.; Spicer, P. T.; Stenzel, M. H. (-)-Riboflavin (vitamin B2) and flavin mononucleotide as visible light photo initiators in the thiol-ene polymerisation of PEG-based hydrogels. *Polym. Chem.* **2017**, *8* (6), 980-984.
- (57) Encinas, M. V.; Rufs, A. M.; Bertolotti, S.; Previtali, C. M. Free Radical Polymerization Photoinitiated by Riboflavin/Amines. Effect of the Amine Structure. *Macromolecules* **2001**, *34* (9), 2845-2847.
- (58) Kim, S. H.; Chu, C. C. Fabrication of a biodegradable polysaccharide hydrogel with riboflavin, vitamin B2, as a photo-initiator and L-arginine as coinitiator upon UV irradiation. *J. Biomed. Mater. Res., Part B* **2009**, *91* (1), 390-400.
- (59) Bertolotti, S. G.; Previtali, C. M.; Rufs, A. M.; Encinas, M. V. Riboflavin/Triethanolamine as Photoinitiator System of Vinyl Polymerization. A Mechanistic Study by Laser Flash Photolysis. *Macromolecules* **1999**, *32* (9), 2920-2924.
- (60) Orellana, B.; Rufs, A. M.; Encinas, M. V.; Previtali, C. M.; Bertolotti, S. The Photoinitiation Mechanism of Vinyl Polymerization by Riboflavin/Triethanolamine in Aqueous Medium. *Macromolecules* **1999**, *32* (20), 6570-6573.
- (61) Shin, J. Y.; Yeo, Y. H.; Jeong, J. E.; Park, S. A.; Park, W. H. Dual-crosslinked methylcellulose hydrogels for 3D bioprinting applications. *Carbohydr. Polym.* **2020**, *238*, 116192.
- (62) Hu, J.; Hou, Y.; Park, H.; Choi, B.; Hou, S.; Chung, A.; Lee, M. Visible light crosslinkable chitosan hydrogels for tissue engineering. *Acta Biomater.* **2012**, *8* (5), 1730-1738.
- (63) Wollensak, G.; Spoerl, E.; Seiler, T. Riboflavin/ultraviolet-a-induced collagen crosslinking for the treatment of keratoconus. *Am. J. Ophthalmol.* **2003**, *135* (5), 620-627.
- (64) Applegate, M. B.; Partlow, B. P.; Coburn, J.; Marelli, B.; Pirie, C.; Pineda, R.; Kaplan, D. L.; Omenetto, F. G. Photocrosslinking of Silk Fibroin Using Riboflavin for Ocular Prostheses. *Adv. Mater.* **2016**, *28* (12), 2417-2420.
- (65) Marti-Figueroa, C. R.; Ashton, R. S. The case for applying tissue engineering methodologies to instruct human organoid morphogenesis. *Acta Biomater.* **2017**, *54*, 35-44.
- (66) Moroni, L.; Boland, T.; Burdick, J. A.; De Maria, C.; Derby, B.; Forgacs, G.; Groll, J.; Li, Q.; Malda, J.; Mironov, V. A.; et al. Biofabrication: A Guide to Technology and Terminology. *Trends Biotechnol.* **2018**, *36* (4), 384-402.
- (67) Moroni, L.; Burdick, J. A.; Highley, C.; Lee, S. J.; Morimoto, Y.; Takeuchi, S.; Yoo, J. J. Biofabrication strategies for 3D in vitro models and regenerative medicine. *Nat. Rev. Mater.* **2018**, *3* (5), 21-37.
- (68) Smith, A. M.; Mancini, M. C.; Nie, S. Bioimaging: second window for in vivo imaging. *Nat. Nanotechnol.* **2009**, *4* (11), 710-711.
- (69) Xing, J. F.; Zheng, M. L.; Duan, X. M. Two-photon polymerization microfabrication of hydrogels: an advanced 3D printing technology for tissue engineering and drug delivery. *Chem. Soc. Rev.* **2015**, *44* (15), 5031-5039.
- (70) Hu, P.; Qiu, W.; Naumov, S.; Scherzer, T.; Hu, Z.; Chen, Q.; Knolle, W.; Li, Z. Conjugated Bifunctional Carbazole - Based Oxime Esters: Efficient and Versatile Photoinitiators for 3D Printing under One - and Two - Photon Excitation. *ChemPhotoChem* **2020**, *4* (3), 224-232.
- (71) Al Mousawi, A.; Dumur, F.; Garra, P.; Toufaily, J.; Hamieh, T.; Graff, B.; Gimes, D.; Fouassier, J. P.; Lalevée, J. Carbazole Scaffold Based Photoinitiator/Photoredox Catalysts: Toward New High Performance Photoinitiating Systems and Application in LED Projector 3D Printing Resins. *Macromolecules* **2017**, *50* (7), 2747-2758.

- (72) Al Mousawi, A.; Lara, D. M.; Noirbent, G.; Dumur, F.; Toufaily, J.; Hamieh, T.; Bui, T.-T.; Goubard, F.; Graff, B.; Gigmes, D.; et al. Carbazole Derivatives with Thermally Activated Delayed Fluorescence Property as Photoinitiators/Photoredox Catalysts for LED 3D Printing Technology. *Macromolecules* **2017**, *50* (13), 4913-4926.
- (73) Chen, H.; Borjigin, T.; Regeard, C.; Xiao, P.; Dumur, F.; Lalevée, J. 5,12-Dihydroindolo[3,2-a]Carbazole Derivatives-Based Water Soluble Photoinitiators for 3D Antibacterial Hydrogels Preparation. *Small* **2023**, e2300772.
- (74) Zhou, C.; Li, P.; Qi, X.; Sharif, A. R.; Poon, Y. F.; Cao, Y.; Chang, M. W.; Leong, S. S.; Chan-Park, M. B. A photopolymerized antimicrobial hydrogel coating derived from epsilon-poly-L-lysine. *Biomaterials* **2011**, *32* (11), 2704-2712.
- (75) ÇAkmakÇI, E.; ŞEn, F.; Kahraman, M. V. Isosorbide Diallyl Based Antibacterial Thiol–Ene Photocured Coatings Containing Polymerizable Fluorous Quaternary Phosphonium Salt. *ACS Sustainable Chem. Eng.* **2019**, *7* (12), 10605-10615.
- (76) Yang, H.; Li, G.; Stansbury, J. W.; Zhu, X.; Wang, X.; Nie, J. Smart Antibacterial Surface Made by Photopolymerization. *ACS Appl. Mater. Interfaces* **2016**, *8* (41), 28047-28054.
- (77) Pentti, H.; Martti, M.; Tuuli, P.; Heli, L. Laxative Potency and Acute Toxicity of Some Anthraquinone Derivatives, Senna Extracts and Fractions of Senna Extracts. *Pharmacology & Toxicology* **1987**, *61* (2), 153-156.
- (78) Desobry, S. A.; Netto, F. M.; Labuza, T. P. Preservation of beta-carotene from carrots. *Critical Reviews in Food Science and Nutrition* **1998**, *38* (5), 381-396.
- (79) Mouri, C.; Laursen, R. Identification of anthraquinone markers for distinguishing Rubia species in madder-dyed textiles by HPLC. *Microchimica Acta* **2012**, *179* (1-2), 105-113.
- (80) Mapari, S. A. S.; Nielsen, K. F.; Larsen, T. O.; Frisvad, J. C.; Meyer, A. S.; Thrane, U. Exploring fungal biodiversity for the production of water-soluble pigments as potential natural food colorants. *Curr Opin Biotechnol* **2005**, *16* (2), 231-238.
- (81) Rajkumar, D.; Kim, J. G. Oxidation of various reactive dyes with in situ electro-generated active chlorine for textile dyeing industry wastewater treatment. *J Hazard Mater* **2006**, *136* (2), 203-212.
- (82) Epolito, W.; Lee, Y.; Bottomley, L.; Pavlostathis, S. Characterization of the textile anthraquinone dye Reactive Blue 4. *Dyes and Pigments* **2005**, *67* (1), 35-46.
- (83) Takahashi, E.; Marczyklo, T. H.; Watanabe, T.; Nagai, S.; Hayatsu, H.; Negishi, T. Preventive effects of anthraquinone food pigments on the DNA damage induced by carcinogens in Drosophila. *Mutation Research/Fundamental and Molecular Mechanisms of Mutagenesis* **2001**, *480-481*, 139-145.
- (84) Al-Otaibi, J. S.; Teesdale Spittle, P.; El Gogary, T. M. Interaction of anthraquinone anti-cancer drugs with DNA: Experimental and computational quantum chemical study. *Journal of Molecular Structure* **2017**, *1127*, 751-760.
- (85) Koceva-Chyla, A.; Jedrzejczak, M.; Skierski, J.; Kania, K.; Jozwiak, Z. Mechanisms of induction of apoptosis by anthraquinone anticancer drugs aclarubicin and mitoxantrone in comparison with doxorubicin: relation to drug cytotoxicity and caspase-3 activation. *Apoptosis* **2005**, *10* (6), 1497-1514.
- (86) Tomane, S.; Sautrot-Ba, P.; Mazeran, P. E.; Lalevée, J.; Graff, B.; Morlet-Savary, F.; Abbad-Andaloussi, S.; Langlois, V.; Versace, D. L. Photoinitiating Systems Based on Anthraquinone Derivatives: Synthesis of Antifouling and Biocide Coatings. *ChemPlusChem* **2017**, *82* (10), 1298-1307.
- (87) Zhuo, J.; Sun, G. Light-induced surface graft polymerizations initiated by an anthraquinone dye on cotton fibers. *Carbohydr. Polym.* **2014**, *112*, 158-164.
- (88) Breloy, L.; Ouarabi, C. A.; Brosseau, A.; Dubot, P.; Brezova, V.; Abbad Andaloussi, S.; Malval, J.-P.; Versace, D.-L. β -Carotene/Limonene Derivatives/Eugenol: Green Synthesis of Antibacterial Coatings under Visible-Light Exposure. *ACS Sustainable Chem. Eng.* **2019**, *7* (24), 19591-19604.

- (89) Rodrigues, A. I.; Franco, A. R.; Rodrigues, F. J.; Leonor, I. B.; Reis, R. L. Unveiling the effect of three-dimensional bioactive fibre mesh scaffolds functionalized with silanol groups on bacteria growth. *J. Biomed. Mater. Res., Part A* **2016**, *104* (9), 2189-2199.
- (90) Tozuka, M.; Igarashi, T.; Sakurai, T. 1-(Arylmethoxy)-9,10-anthraquinones: Photoinitiators for Radical and Cationic Polymerizations. *Polym. J.* **2009**, *41* (9), 709-714.
- (91) Zhang, J.; Lalevée, J.; Hill, N. S.; Peng, X.; Zhu, D.; Kiehl, J.; Morlet-Savary, F.; Stenzel, M. H.; Coote, M. L.; Xiao, P. Photoinitiation Mechanism and Ability of Monoamino-Substituted Anthraquinone Derivatives as Cationic Photoinitiators of Polymerization under LEDs. *Macromol. Rapid Commun.* **2019**, *40* (16), e1900234.
- (92) Wang, G.; Hill, N. S.; Zhu, D.; Xiao, P.; Coote, M. L.; Stenzel, M. H. Efficient Photoinitiating System Based on Diaminoanthraquinone for 3D Printing of Polymer/Carbon Nanotube Nanocomposites under Visible Light. *ACS Appl. Polym. Mater.* **2019**, *1* (5), 1129-1135.
- (93) Xiao, P.; Dumur, F.; Graff, B.; Fouassier, J. P.; Gimes, D.; Lalevée, J. Cationic and Thiol-Ene Photopolymerization upon Red Lights Using Anthraquinone Derivatives as Photoinitiators. *Macromolecules* **2013**, *46* (17), 6744-6750.
- (94) Zhang, J.; Lalevée, J.; Morlet-Savary, F.; Graff, B.; Xiao, P. Photopolymerization under various monochromatic UV/visible LEDs and IR lamp: Diamino-anthraquinone derivatives as versatile multicolor photoinitiators. *Eur. Polym. J.* **2019**, *112*, 591-600.
- (95) Zhang, J.; Hill, N.; Lalevée, J.; Fouassier, J.-P.; Zhao, J.; Graff, B.; Schmidt, T. W.; Kable, S. H.; Stenzel, M. H.; Coote, M. L.; et al. Multihydroxy-Anthraquinone Derivatives as Free Radical and Cationic Photoinitiators of Various Photopolymerizations under Green LED. *Macromol. Rapid Commun.* **2018**, *39* (19), e1800172.
- (96) Gruijl, F. R.; Kranen, H. J.; Mullenders, L. H. F. UV-induced DNA damage, repair, mutations and oncogenic pathways in skin cancer. *J. Photochem. Photobiol., B* **2001**, *63* (1-3), 19-27.
- (97) Nishigori, C. UV-induced DNA damage in carcinogenesis and its repair. *J. Dermatol. Sci.* **2000**, *23* (1), S41-S44.
- (98) Brash, D. E. UV signature mutations. *Photochem. Photobiol.* **2015**, *91* (1), 15-26.
- (99) Ichihashi, M.; Ueda, M.; Budiyo, A.; Bito, T.; Oka, M.; Fukunaga, M.; Tsuru, K.; Horikawa, T. UV-induced skin damage. *Toxicology* **2003**, *189* (1-2), 21-39.
- (100) Resetco, C.; Hendriks, B.; Badi, N.; Du Prez, F. Thiol-ene chemistry for polymer coatings and surface modification – building in sustainability and performance. *Mater. Horiz.* **2017**, *4* (6), 1041-1053.
- (101) Tardy, A.; Nicolas, J.; Gimes, D.; Lefay, C.; Guillaneuf, Y. Radical Ring-Opening Polymerization: Scope, Limitations, and Application to (Bio)Degradable Materials. *Chem. Rev.* **2017**, *117* (3), 1319-1406.
- (102) Jakubiak, J.; Allonas, X.; Fouassier, J. P.; Sionkowska, A.; Andrzejewska, E.; Linden, L. A.; Rabek, J. F. Camphorquinone-amines photoinitiating systems for the initiation of free radical polymerization. *Polymer* **2003**, *44* (18), 5219-5226.
- (103) Kirschner, J.; Szillat, F.; Bouzrati-Zerelli, M.; Becht, J. M.; Klee, J. E.; Lalevée, J. Sulfinates and sulfonates as high performance co-initiators in CQ based systems: Towards aromatic amine-free systems for dental restorative materials. *Dent. Mater.* **2020**, *36* (2), 187-196.
- (104) Fang, Y.; Wang, X. Metal-Free Boron-Containing Heterogeneous Catalysts. *Angew. Chem., Int. Ed.* **2017**, *56* (49), 15506-15518.
- (105) Treat, N. J.; Sprafke, H.; Kramer, J. W.; Clark, P. G.; Barton, B. E.; Read de Alaniz, J.; Fors, B. P.; Hawker, C. J. Metal-free atom transfer radical polymerization. *J. Am. Chem. Soc.* **2014**, *136* (45), 16096-16101.
- (106) Perkowski, A. J.; You, W.; Nicewicz, D. A. Visible Light Photoinitiated Metal-Free Living Cationic Polymerization of 4-Methoxystyrene. *J. Am. Chem. Soc.* **2015**, *137* (24), 7580-7583.
- (107) Elliott, A. J. Dioxoles and Oxathioles. In *Comprehensive Heterocyclic Chemistry*, Katritzky, A. R., Rees, C. W. Eds.; Five-membered Rings with Two or More Oxygen, Sulfur or Nitrogen Atoms, Vol. 6; Elsevier Science Ltd., 1984; pp 749-782.

- (108) Xiao, P.; Lalevée, J.; Allonas, X.; Fouassier, J. P.; Ley, C.; El-Roz, M.; Shi, S. Q.; Nie, J. Photoinitiation mechanism of free radical photopolymerization in the presence of cyclic acetals and related compounds. *J. Polym. Sci., Part A: Polym. Chem.* **2010**, *48* (24), 5758-5766.
- (109) Kabatc, J. Cyclic acetals as the second co-initiators in three-component photoinitiating systems. *Polym. Bull.* **2011**, *68* (3), 667-679.
- (110) Wang, K.; Han, J.; Shi, S.; Nie, J. Effect of cyclic acetals structure on efficiency of photoinitiation. *Polym. Adv. Technol.* **2009**, *21* (6), 430-434.
- (111) Wang, K.; Yang, D.; Xiao, M.; Chen, X.; Lu, F.; Nie, J. Sesamin as a co-initiator for unfilled dental restorations. *Acta Biomater.* **2009**, *5* (7), 2508-2517.
- (112) Shi, S.; Gao, H.; Wu, G.; Nie, J. Cyclic acetal as coinitorator for bimolecular photoinitiating systems. *Polymer* **2007**, *48* (10), 2860-2865.
- (113) Wang, K.; Ma, G.; Qin, X.; Xiao, M.; Nie, J. Cyclic acetals as coinitorators in CQ-induced photopolymerizations. *Polym. J.* **2010**, *42* (6), 450-455.
- (114) Wang, K.; Yin, R.; Zhang, X.; Shi, S.; Nie, J. Synthesis and photopolymerization of piperonylamine derivatives as a polymerizable cyclic acetals co-initiator for light-cured unfilled dental resins. *Polym. Adv. Technol.* **2010**, *21* (9), 609-614.
- (115) Xu, X.; Awad, A.; Robles-Martinez, P.; Gaisford, S.; Goyanes, A.; Basit, A. W. Vat Photopolymerization 3D Printing for Advanced Drug Delivery and Medical Device Applications. *J. Controlled Release* **2021**, *329*, 743-757.
- (116) Economidou, S. N.; Uddin, M. J.; Marques, M. J.; Douroumis, D.; Sow, W. T.; Li, H.; Reid, A.; Windmill, J. F. C.; Podoleanu, A. A novel 3D printed hollow microneedle microelectromechanical system for controlled, personalized transdermal drug delivery. *Addit. Manuf.* **2021**, *38*, 101815.
- (117) Detamornrat, U.; McAlister, E.; Hutton, A. R. J.; Larraneta, E.; Donnelly, R. F. The Role of 3D Printing Technology in Microengineering of Microneedles. *Small* **2022**, *18* (18), e2106392.
- (118) Liu, H.; Wang, Y.; Cui, K.; Guo, Y.; Zhang, X.; Qin, J. Advances in Hydrogels in Organoids and Organs-on-a-Chip. *Adv. Mater.* **2019**, *31* (50), e1902042.
- (119) Puig-Lleixà, C.; Jiménez, C.; Bartrolí, J. Acrylated polyurethane — photopolymeric membrane for amperometric glucose biosensor construction. *Sens. Actuators, B* **2001**, *72* (1), 56-62.
- (120) Schalkhammer, T.; Lobmaier, C.; Pittner, F.; Leitner, A.; Brunner, H.; Aussenegg, F. R. The use of metal-island-coated pH-sensitive swelling polymers for biosensor applications. *Sens. Actuators, B* **1995**, *24* (1-3), 166-172.
- (121) Mikulchyk, T.; Walshe, J.; Cody, D.; Martin, S.; Naydenova, I. Humidity and temperature induced changes in the diffraction efficiency and the Bragg angle of slanted photopolymer-based holographic gratings. *Sens. Actuators, B* **2017**, *239*, 776-785.
- (122) Huang, H. C.; Huang, S. Y.; Lin, C. I.; Lee, Y. D. A multi-array sensor via the integration of acrylic molecularly imprinted photoresists and ultramicroelectrodes on a glass chip. *Anal. Chim. Acta* **2007**, *582* (1), 137-146.
- (123) Kong, L.; Deng, Z.; You, D. Chemistry and biosynthesis of bacterial polycyclic xanthone natural products. *Nat. Prod. Rep.* **2022**, *39* (11), 2057-2095.
- (124) Winter, D. K.; Sloman, D. L.; Porco, J. A., Jr. Polycyclic xanthone natural products: structure, biological activity and chemical synthesis. *Nat. Prod. Rep.* **2013**, *30* (3), 382-391.
- (125) Sagratini, G.; Mañes, J.; Giardiná, D.; Picó, Y. Determination of isopropyl thioxanthone (ITX) in fruit juices by pressurized liquid extraction and liquid chromatography-mass spectrometry. *J. Agric. Food Chem.* **2006**, *54* (20), 7947-7952.
- (126) Zhu, M.; Liu, Y.; Jiang, F.; Cao, J.; Kundu, S. C.; Lu, S. Combined Silk Fibroin Microneedles for Insulin Delivery. *ACS Biomater. Sci. Eng.* **2020**, *6* (6), 3422-3429.
- (127) Tsiaris, K.; Raja, W. K.; Pritchard, E. M.; Panilaitis, B.; Kaplan, D. L.; Omenetto, F. G. Fabrication of Silk Microneedles for Controlled-Release Drug Delivery. *Adv. Funct. Mater.* **2012**, *22* (2), 330-335.

- (128) Shin, D.; Hyun, J. Silk fibroin microneedles fabricated by digital light processing 3D printing. *J. Ind. Eng. Chem.* **2021**, *95*, 126-133.
- (129) Xia, Y.; He, Y.; Zhang, F.; Liu, Y.; Leng, J. A Review of Shape Memory Polymers and Composites: Mechanisms, Materials, and Applications. *Adv. Mater.* **2021**, *33* (6), e2000713.
- (130) Zarek, M.; Layani, M.; Cooperstein, I.; Sachyani, E.; Cohn, D.; Magdassi, S. 3D Printing of Shape Memory Polymers for Flexible Electronic Devices. *Adv. Mater.* **2016**, *28* (22), 4449-4454.
- (131) Zhang, F.; Xiong, L.; Ai, Y.; Liang, Z.; Liang, Q. Stretchable Multiresponsive Hydrogel with Actuable, Shape Memory, and Self-Healing Properties. *Adv. Sci.* **2018**, *5* (8), 1800450.
- (132) Leanza, S.; Wu, S.; Sun, X.; Qi, H. J.; Zhao, R. R. Active Materials for Functional Origami. *Adv. Mater.* **2023**, e2302066.
- (133) Yu, R.; Yang, X.; Zhang, Y.; Zhao, X.; Wu, X.; Zhao, T.; Zhao, Y.; Huang, W. Three-Dimensional Printing of Shape Memory Composites with Epoxy-Acrylate Hybrid Photopolymer. *ACS Appl. Mater. Interfaces* **2017**, *9* (2), 1820-1829.
- (134) Zhang, B.; Zhang, W.; Zhang, Z.; Zhang, Y. F.; Hingorani, H.; Liu, Z.; Liu, J.; Ge, Q. Self-Healing Four-Dimensional Printing with an Ultraviolet Curable Double-Network Shape Memory Polymer System. *ACS Appl. Mater. Interfaces* **2019**, *11* (10), 10328-10336.
- (135) Huang, B.; Hu, R.; Xue, Z.; Zhao, J.; Li, Q.; Xia, T.; Zhang, W.; Lu, C. Continuous Liquid Interface Production of Alginate/Polyacrylamide Hydrogels with Supramolecular Shape Memory Properties. *Carbohydr. Polym.* **2020**, *231*, 115736.
- (136) Yin, Q.; Tu, S.; Chen, M.; Wu, L. Bioinspired Design of Reinforced Gradient Hydrogels with Rapid Water-Triggered Shape Memory Performance. *ACS Appl. Polym. Mater.* **2020**, *2* (7), 2858-2866.
- (137) Chen, H.; Noirbent, G.; Zhang, Y.; Brunel, D.; Gigmes, D.; Morlet-Savary, F.; Graff, B.; Xiao, P.; Dumur, F.; Lalevée, J. Novel D- π -A and A- π -D- π -A three-component photoinitiating systems based on carbazole/triphenylamino based chalcones and application in 3D and 4D printing. *Polym. Chem.* **2020**, *11* (40), 6512-6528.
- (138) Chen, H.; Noirbent, G.; Liu, S.; Brunel, D.; Graff, B.; Gigmes, D.; Zhang, Y.; Sun, K.; Morlet-Savary, F.; Xiao, P.; et al. Bis-chalcone derivatives derived from natural products as near-UV/visible light sensitive photoinitiators for 3D/4D printing. *Mater. Chem. Front.* **2021**, *5* (2), 901-916.
- (139) Zhu, D.; Peng, X.; Xiao, P. Indigo Carmine: A Base and Neutral Electrolyte-mediated Photoinitiator for 3D Printing in High Fidelity. *Addit. Manuf.* **2022**, *59*, 103154.
- (140) Hammoud, F.; Pavlou, A.; Petropoulos, A.; Graff, B.; Siskos, M. G.; Hijazi, A.; Morlet-Savary, F.; Dumur, F.; Lalevée, J. Naphthoquinone-based imidazolyl esters as blue-light-sensitive Type I photoinitiators. *Polym. Chem.* **2022**, *13* (33), 4817-4831.
- (141) Zhang, J.; Zivic, N.; Dumur, F.; Guo, C.; Li, Y.; Xiao, P.; Graff, B.; Gigmes, D.; Fouassier, J. P.; Lalevée, J. Panchromatic photoinitiators for radical, cationic and thiol-ene polymerization reactions: A search in the diketopyrrolopyrrole or indigo dye series. *Mater. Today Commun.* **2015**, *4*, 101-108.
- (142) Li, Z.; Zou, X.; Shi, F.; Liu, R.; Yagci, Y. Highly efficient dandelion-like near-infrared light photoinitiator for free radical and thiol-ene photopolymerizations. *Nat. Commun.* **2019**, *10* (1), 3560.
- (143) Sari, H.; Pirjo, S.; Riitta, T. QUERCETIN CONTENT IN BERRY PRODUCTS. In *Natural Antioxidants and Anticarcinogens in Nutrition, Health and Disease*, 1999; pp 341-342.
- (144) Sahiner, M.; Sahiner, N.; Sagbas, S.; Fullerton, M. L.; Blake, D. A. Fabrication of Biodegradable Poly(naringin) Particles with Antioxidant Activity and Low Toxicity. *ACS Omega* **2018**, *3* (12), 17359-17367.
- (145) Peng, R.; Wu, Q.; Chen, J.; Ghosh, R.; Chen, X. Isolation of ellagic acid from pomegranate peel extract by hydrophobic interaction chromatography using graphene oxide grafted cotton fiber adsorbent. *J. Sep. Sci.* **2018**, *41* (3), 747-755.
- (146) Villaño, D.; García-Viguera, C.; Mena, P. Colors: Health Effects. In *Encyclopedia of Food and Health*, Caballero, B., Finglas, P. M., Toldrá, F. Eds.; Elsevier B.V., 2016; pp 265-272.

- (147) Cai, W.; Chen, Y.; Xie, L.; Zhang, H.; Hou, C. Characterization and density functional theory study of the antioxidant activity of quercetin and its sugar-containing analogues. *Eur. Food Res. Technol.* **2013**, *238* (1), 121-128.
- (148) Alam, M. A.; Subhan, N.; Rahman, M. M.; Uddin, S. J.; Reza, H. M.; Sarker, S. D. Effect of citrus flavonoids, naringin and naringenin, on metabolic syndrome and their mechanisms of action. *Adv. Nutr.* **2014**, *5* (4), 404-417.
- (149) Lavrador, P.; Gaspar, V. M.; Mano, J. F. Bioinspired bone therapies using naringin: applications and advances. *Drug Discovery Today* **2018**, *23* (6), 1293-1304.
- (150) Alfei, S.; Turrini, F.; Catena, S.; Zunin, P.; Grilli, M.; Pittaluga, A. M.; Boggia, R. Ellagic acid a multi-target bioactive compound for drug discovery in CNS? A narrative review. *Eur. J. Med. Chem.* **2019**, *183*, 111724.
- (151) Scientific Opinion on the re-evaluation of Indigo Carmine (E 132) as a food additive. *EFSA J.* **2014**, *12* (7), 3768.

Chapter 2 Flavones: natural photoinitiators extracted from berries

2.1 Preface

A few synthetic and natural flavones have been investigated as effective photoinitiators.^{1, 2} However, most of the investigated flavone derivatives merely exhibited UV absorption (i.e., < 400 nm). Not only is the safety of photoinitiator, but the irradiation safety is also principal. Therefore, the development of visible-light-sensitive natural photoinitiators is imperative. Additionally, considering the photopolymerization types, for instance, free radical photopolymerization, cationic photopolymerization, thiol-ene photopolymerization, etc., versatile photoinitiators are anticipated in diverse demands. The reported flavone derivatives only demonstrated their free radical photoinitiation abilities to acrylates/methacrylates and/or cationic photoinitiation ability to epoxides. As a promising photoinitiator family, natural flavone derivatives could be developed as a versatile photoinitiator for other photopolymerization types (e.g., cationic photopolymerization of vinyl, thiol-ene photopolymerization, etc.).

As the aforementioned objective in the Introduction, this chapter aims to develop a visible-light-sensitive natural photoinitiator for diverse types of photopolymerization. To achieve this, berries-extracted flavone derivatives, quercetin and morin, were introduced in the present chapter to unravel the photoinitiation capability. Quercetin and morin exhibited their visible light sensitivities to violet-blue light and violet-yellow light, respectively. Furthermore, their photoreaction mechanism has been elucidated, and their photoinitiation abilities in diverse resins (i.e., bisphenol A glycidyl methacrylate (Bis-GMA)/triethylene glycol dimethacrylate (TEGDMA) blend, trimethylolpropane triacrylate (TMPTA), tri(ethylene glycol) divinyl ether (DVE-3), DVE-3/trimethylolpropane tris(3-mercaptopropionate) (TriThiol) blend, and DVE-3/1,3,5-triallyl-1,3,5-triazine-2,4,6(1H,3H,5H)-trione (Trione) blend) are presented. Additionally, their performance under two different light irradiations was also compared and discussed.

Briefly, the developed photoinitiating systems demonstrated their efficient photoinitiation abilities in diverse hydrophobic polymerization formulations under violet-blue LEDs via a photo-redox reaction.

2.2 Statement of contribution

I declare that the published research results enclosed in this chapter are the original work carried out by me for my Ph.D. program at Australian National University.

As the first author, I contributed to the development of the concept, outline of the experiments, data analysis, figure production, and preparation of the original draft, under the supervision of my primary supervisor, Prof. Pu Xiao.

2.3 Publication status

The published manuscript entitled “Penta-Hydroxy Flavones-Based Photoinitiating Systems for Free Radical, Cationic, and Thiol-Ene Polymerization upon Exposure to Mild Blue LEDs” and the supporting information are reproduced as a chapter with permission³, Copyright 2021, Wiley-VCH GmbH. This manuscript has been published in the journal **Macromolecular Materials & Engineering** in 2021, and the citation of this published manuscript is:

Zhu, D.; Peng, X.; Xiao, P. Penta-Hydroxy Flavones-Based Photoinitiating Systems for Free Radical, Cationic, and Thiol-Ene Polymerization upon Exposure to Mild Blue LEDs. *Macromol. Mater. Eng.* **2021**, *306* (6), 2100059. DOI: 10.1002/mame.202100059.

2.4 Abstract

Natural flavone-derivatives (i.e., morin and quercetin) are investigated as visible light-sensitive photoinitiators. The photochemical mechanisms of the radical generation from flavone-derivative-based photoinitiating systems (PISs) upon exposure to mild blue light-emitting diodes are studied. The impact of the substituent site of functional groups on the photoinitiation ability is determined. The quercetin-based PISs exhibit more reactivity than the morin-based systems on free radical photopolymerization. Moreover, the investigated flavone-based PISs present their stabilities at room temperature, indicating that resins containing these systems barely require special storage requirements. Thiol-ene polymerization initiated by the flavone-derivatives-based PISs is also investigated.

2.5 Introduction

Photopolymerization is an attractive strategy using light as an energy provider to initiate polymerization. Photoinitiator excited by irradiation is a pivotal component to initiate polymerization via the generation of active species (e.g., free radicals and cations).^{4, 5}

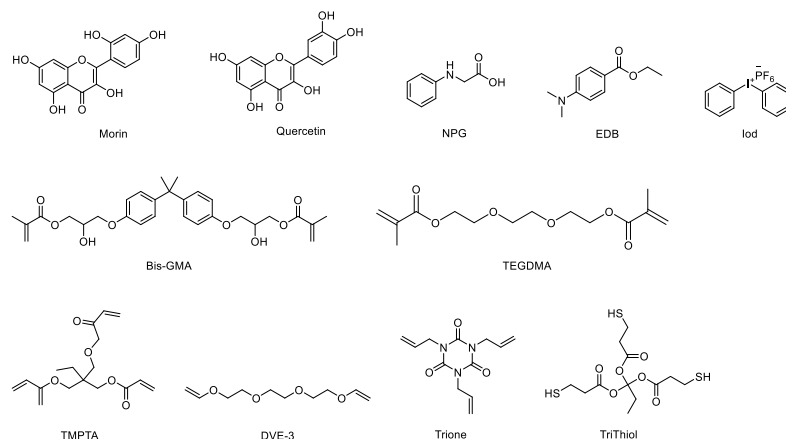
According to previous reports, UV exposure is harmful to human beings.⁶⁻⁹ The investigation and development of novel photoinitiators sensitive to visible light are boosting.^{2, 10-21} Apart from synthetic photoinitiators sensitive to visible light (e.g., naphthalimide dyes, pyromethene dye, etc.^{22, 23}), numerous natural dyes were published as effective photoinitiators due to their fascinating photochemical properties.²⁴⁻²⁸ For instance, curcumin, riboflavin, and anthraquinone derivatives were well investigated.^{12, 13, 27, 29-34} Flavones, known as biosynthesized products with promising benefits according to in vivo studies,³⁵ were revealed as effective visible light photoinitiators.^{1,2} The hydroxyl substituted flavones exhibited better performance than flavone in the presence of *N*-phenyl glycine (NPG) under LED@405 nm.¹ A flavone-derived photoinitiator was also investigated in atom transfer radical polymerization of methyl methacrylate.³⁶ The flavone excited by 350-440 nm of light irradiation transferred electron to amine, then CuBr was reduced by the electrons from CuBr₂. The radicals were produced from the oxidation of CuBr and then successfully initiated polymerization. The photopolymerization was well-controlled with living characters induced by flavone. These reports inspired us to explore flavone-derivatives as effective visible light sensitive photoinitiators and develop effective flavone-derivative-based PISs for various types of photopolymerization. Morin and quercetin, two penta-hydroxy flavones (PHFs) (Scheme 2.1), were discovered as dietary flavonoid inhibitors of monocarboxylate because of flavone derivatives metabolized by plants. Quercetin has been developed as a photosensitizer of iodonium salt to initiate the cationic photopolymerization of epoxy monomer under the UV light. Moreover, quercetin is an antibacterial agent to endow the photocured patches with antibacterial properties.³⁷ However, quercetin has not been investigated as a photoinitiator for other types of photopolymerization reactions (e.g., free radical polymerization or thiol-ene polymerization). The photoinitiation ability of quercetin under the irradiation of mild light-emitting diodes (LED) lights was unclear. Accordingly, to characterize the photochemical mechanisms of two PHFs, ultraviolet–visible spectrophotometer (UV–vis) and electron paramagnetic resonance spin trapping (EPR-ST) were used. The comparison of photoinitiation abilities of morin and quercetin in the presence of diverse additives in free radical, cationic, and thiol-ene polymerization was determined by real-time Fourier-transform infrared spectroscopy (RT-FTIR).

2.6 Experimental

2.6.1 Materials

The investigated compounds, morin (B.D.H), quercetin (L. LIGHT & Co. Ltd.), and additives, diphenyliodonium hexafluorophosphate (Iod), ethyl 4-(dimethylamino)benzoate (EDB), and *N*-phenyl glycine (NPG) were purchased from Sigma-Aldrich. Bisphenol A glycidyl methacrylate

(Bis-GMA), triethylene glycol dimethacrylate (TEGDMA), trimethylolpropane triacrylate (TMPTA), tri(ethylene glycol) divinyl ether (DVE-3), 1,3,5-triallyl-1,3,5-triazine-2,4,6(1H,3H,5H)-trione (Trione), and trimethylolpropane tris(3-mercaptopropionate) (TriThiol) were obtained from Sigma-Aldrich as well. The chemical structures are shown in Scheme 2.1. Isotope solvents for NMR characterization were obtained from Cambridge Isotope Laboratories, Inc., Andover, MA. Other solvents applied in experiments were from Merck KGaA, Darmstadt, Germany.



Scheme 2.1. Chemical structures of the investigated photoinitiators (morin and quercetin), additives (NPG, EDB, and Iod), and monomers (Bis-GMA, TEGDMA, TMPTA, DVE-3, Trione, and TriThiol).

2.6.2 Irradiation Sources

LEDs with emission wavelengths centered at 394 nm (4 mW cm^{-2}), 410 nm (110 mW cm^{-2}), and 445 nm (80 mW cm^{-2}) were used as the irradiation devices.

2.6.3 Steady-State Photolysis

Varian Cary 50 Bio UV–visible (UV–vis) spectrophotometer from Agilent Technologies was utilized in steady-state photolysis experiments. Investigated photoinitiators in ethanol were irradiated under UV LED@394 nm in the presence of iodonium salt, being recorded by UV-vis at different irradiation timepoint.

2.6.4 Electron Paramagnetic Resonance Spin Trapping

EPR-ST experiment was conducted via Bruker E500 spectrometer equipped with a Bruker ER4122 SHQ resonator. Samples were loaded into standard X-band EPR tubes of 2.8 mm i.d. The radicals were generated at room temperature upon exposure to UV LED@374 nm under nitrogen

purging. Radicals were trapped by phenyl-*N*-tert-butyl nitron (PBN). The simulation was processed via WINSIM application.

2.6.5 Photopolymerization Experiments

The free radical photopolymerization of Bis-GMA/TEGDMA (70%/30%, w/w) and TMPTA as well as cationic photopolymerization of DVE-3 in the presence of morin- or quercetin-based PISs were investigated. The degree of conversion of the functional group was monitored by INVENIOR, RT-FTIR, from Bruker. In detail, a thin layer of Bis-GMA/TEGDMA, TMPTA, or DVE-3 formulation was laid between two plastic laminates and sandwiched between two BaF₂ windows. The prepared sample was exposed to a selected LED, and RT-FTIR measured infrared absorption of samples along with time. The decreasing number of carbon–carbon double bonds of photopolymerized monomers (TMPTA, Bis-GMA/TEGDMA, and DVE-3) was followed by FTIR with a characterization band at 1620 cm⁻¹. Double bond of Trione and thiol bond of TriThiol were located at 933 and 2569 cm⁻¹, respectively, in FTIR. The degree of conversion was calculated by $D.C. = \left(1 - \frac{\int O.D.d\tilde{\nu}|_{t=t}}{\int O.D.d\tilde{\nu}|_{t=0}}\right) \times 100\%$ (O.D.: absorbance; $\tilde{\nu}$: wavenumber.)

2.7 Results and Discussion

2.7.1 Light Absorption Properties of Morin and Quercetin

The light absorption of two PHFs, morin and quercetin, were investigated in ethanol using the UV-vis spectrometer (Figure 2.1). Morin showed no distinctive absorption peak in UV-visible range while quercetin was characterized by the maximum absorption at 372 nm ($\epsilon_{372 \text{ nm}} = 23,300 \text{ M}^{-1} \text{ cm}^{-1}$), ascribed to the molecular polar effect and the position of substituents.³⁸ The phenomenon was also observed for other flavone and anthraquinone derivatives substituted with diverse groups at varied positions which resulted in various light absorption properties.^{1, 2, 12, 31, 33, 39} The corresponding molar extinction coefficients of morin and quercetin at their maximum absorption and the emission wavelengths of LEDs utilized in the present work were summarized in Table 2.1.

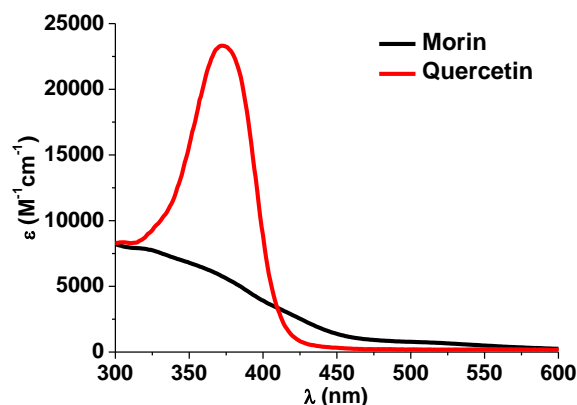


Figure 2.1. UV-vis absorption spectra of morin and quercetin in ethanol.

Table 2.1. Light absorption properties of morin and quercetin in ethanol: maximum absorption wavelengths λ_{\max} , extinction coefficients at λ_{\max} and at the maximum emission wavelengths of the different LED bulbs.

	λ_{\max} (nm)	ϵ_{\max} ($M^{-1}cm^{-1}$)	$\epsilon_{374\text{ nm}}$ ($M^{-1}cm^{-1}$) ^{a)}	$\epsilon_{394\text{ nm}}$ ($M^{-1}cm^{-1}$) ^{a)}	$\epsilon_{410\text{ nm}}$ ($M^{-1}cm^{-1}$) ^{a)}	$\epsilon_{445\text{ nm}}$ ($M^{-1}cm^{-1}$) ^{a)}
Morin	-	-	5700	4300	3360	1560
Quercetin	372	23,300	23,200	13,960	3260	360

^{a)} For different LEDs.

2.7.2 Photochemistry of Morin and Quercetin

The steady-state photolysis studies of PHF-based PISs in the absence and the presence of various additives (i.e., Iod, EDB or NPG) were carried out to investigate the efficiencies of the relevant PISs. As shown in Figure 2.2, the immediate photolysis of morin/Iod or quercetin/Iod was observed under light irradiation. The UV-vis absorption of morin/Iod was reduced in the range of 325-450 nm along with the light irradiation. The similar implication was concluded from the results of the steady-state photolysis of quercetin/Iod, and its UV-vis absorption was diminished at 374 nm. Little change of absorbance was found in morin or quercetin alone under the irradiation of the LED@394 nm (Figure S2.1a,b), indicating that they cannot undergo chemical bond cleavage route. Compared to the addition of Iod, the addition of EDB to the PHFs cannot lead to significant photolysis (Figure S2.1c,d) which revealed the ineffectiveness of the morin/EDB or quercetin/EDB systems. Remarkably, the systems in combination with NPG presented more drastic decreases of the morin- or quercetin-based systems absorption (Figure S2.1e,f) than that of PHFs alone and PHFs/EDB systems. This was ascribed to the weaker hydrogen abstraction ability of PHF from EDB compared to that from NPG.⁴⁰

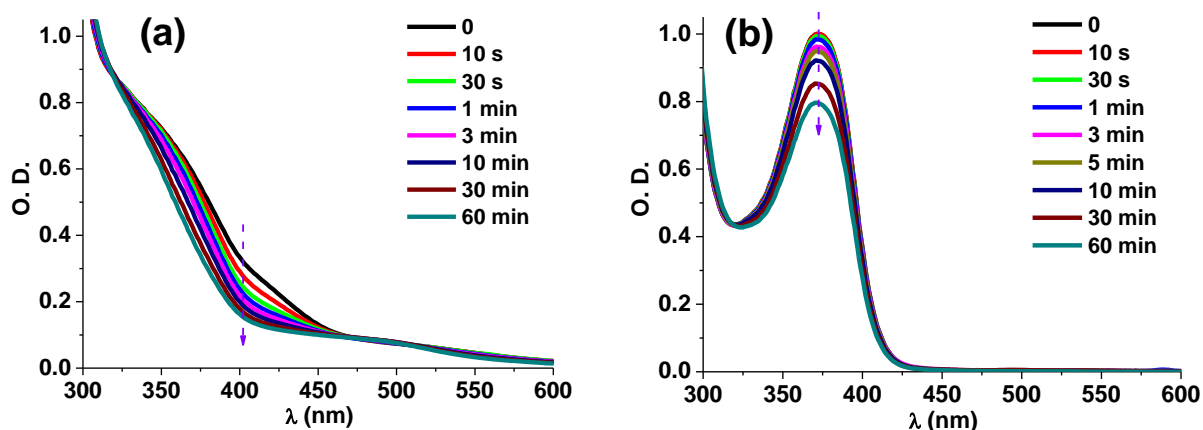


Figure 2.2. Steady state photolysis of (a) morin/iod and (b) quercetin/iod in ethanol ($[Iod] = 8$ mM); UV-vis spectra recorded at different irradiation time; UV LED at 394 nm irradiation (4 $mW \cdot cm^{-2}$).

Free radicals or cations are the active species for the initiation of photopolymerization. The active species were characterized by EPR-ST. The hyperfine splitting constants of PBN/radical adducts were $a_N = 14.3$ G and $a_H = 2.2$ G (Figure 2.3), which characterized the trapped radical as PBN/phenyl radical adduct in *tert*-butylbenzene.^{41, 42} In combination with the mechanism studies, the mechanism of radical generation starting at ground-state photoinitiator was proposed. The photoinitiator was excited by light (Reaction 2.1), and the excited molecules were reacted with Iod to produce free radicals or cations (Reaction 2.2 and Reaction 2.3).

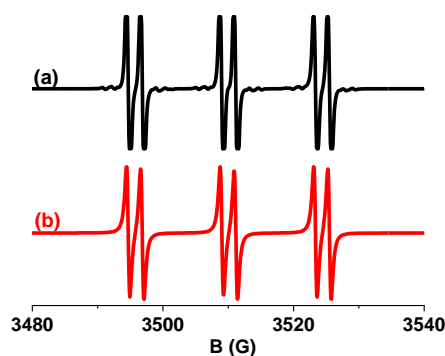
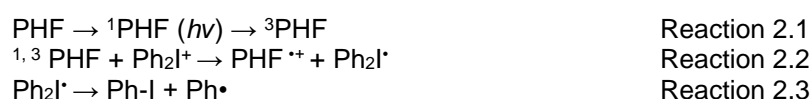


Figure 2.3. EPR spectra of the radicals generated in quercetin/iod combination upon LED@374 nm exposure and trapped by PBN in *tert*-butylbenzene: (a) experimental and (b) simulated spectra. PBN/phenyl radical adducts formed in quercetin/iod system: $a_N = 14.3$ G, $a_H = 2.2$ G., reference values in refs.^{41, 42}.



2.7.3 Photopolymerization Kinetics in the Presence of Morin- and Quercetin-Based PISs under Blue LEDs

Morin and quercetin were considered as potential photoinitiator candidates according to the photochemical mechanism studies. To further confirm the efficiencies of these two compounds as photoinitiators, photopolymerization kinetics studies were conducted, where dental resin (Bis-GMA/TEGDMA (70%/30%, wt)), TMPTA, and DVE-3 were utilized. Bis-GMA/TEGDMA blend is a common dental resin in dentist clinics, thus using nontoxic photoinitiator to initiate restorative materials formation is indispensable.⁴³ The photoinitiation ability of morin and quercetin with the addition of additives (i.e., Iod and/or NPG) upon exposure to LED@410 and LED@445 nm were summarized in Figure 2.4. To reveal the Iod influenced photoinitiation ability, the photopolymerization of Bis-GMA/TEGDMA (70%/30%, wt) initiated by NPG alone was also performed (Table 2.2). The NPG cannot initiate polymerization of BisGMA/TEGDMA under the irradiation of LED@410 nm (Figure 2.4a). With the addition of Iod, NPG/Iod formed charge transfer complexes (CTCs) being confirmed as a versatile initiating component reaching 60% final conversion (FC) of Bis-GMA/TEGDMA (70%/30%, wt).⁴⁴ Morin/Iod cannot initiate polymerization of Bis-GMA/TEGDMA (70%/30%, wt) upon exposure to the LED@410 nm and the LED@445 nm due to its lack of efficiency. As to quercetin-based PISs irradiated by LED@410 nm (Figure 2.4a), the two-component PIS, quercetin/Iod couple, reached only 26% FC. The three-component system, quercetin/Iod/NPG, showed the highest efficiency (FC = 60%) equaled to that of NPG/Iod couple. Meanwhile, due to the efficient free radical production in the presence of NPG/Iod, the conversion of BisGMA/TEGDMA inclined continuously, while lack of free radical generation of quercetin/Iod resulted in rapid completion of photopolymerization (Figure 2.4a). When it came to LED@445 nm (Figure 2.4b), the presence of quercetin in the PIS (i.e., quercetin/Iod/NPG) enhanced both FC and R_p of Bis-GMA/TEGDMA (70%/30%, wt) compared to those in the presence of NPG/Iod couple. NPG/Iod initiated photopolymerization of Bis-GMA/TEGDMA (70%/30%, wt) (Figure 2.4b) was ascribed to the polymerization ability of CTC.⁴⁴ Quercetin exhibited the light absorption at 445 nm (Figure 2.1), therefore quercetin improved photopolymerization of Bis-GMA/TEGDMA (70%/30%, wt) under irradiation of LED@445 nm recognizably. The quercetin/NPG/Iod system displayed not only the best photoinitiation ability for free radical polymerization of Bis-GMA/TEGDMA (70%/30%, wt), but also exceptional stability in a lightproof container at room temperature (Figure S2.2).

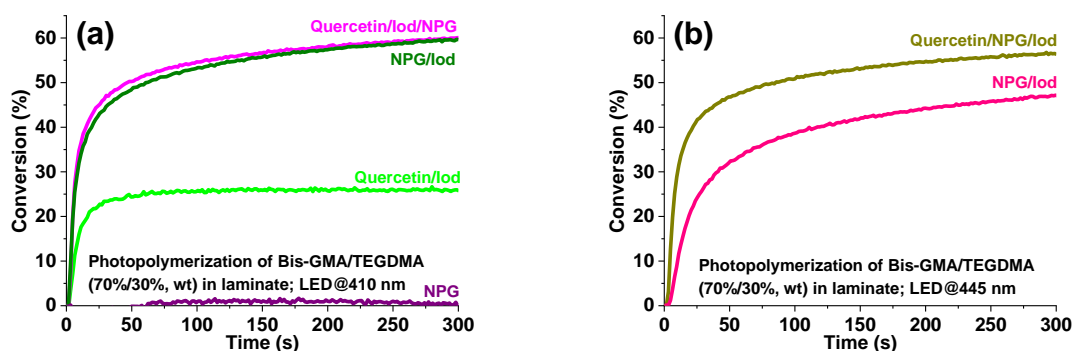


Figure 2.4. Photopolymerization profiles (double bond conversions vs time) of Bis-GMA/TEGDMA blend (70%/30%, w/w) in laminate in the presence of NPG- and quercetin-based PISs (quercetin: 0.5 wt%; NPG: 2 wt%; lod: 2 wt%) upon exposure to (a) LED@410 nm (110 mW cm^{-2}) and (b) LED@445 nm (80 mW cm^{-2}).

Table 2.2. Photopolymerization rates and double bond conversions of photopolymerization of Bis-GMA/TEGDMA blend (70%/30%, w/w) in the presence of quercetin-based PISs (quercetin: 0.5 wt%; lod: 2 wt%; NPG: 2 wt%) upon exposure to the LED@410 nm (110 mW cm^{-2}) or the LED@445 nm (80 mW cm^{-2}) for 300 s.

PISs	$(R_p/[C=C]) \times 100^a \text{ (s}^{-1}\text{)}$	C^b
NPG ^c	0	0
NPG/iod ^c	6.0	60%
Quercetin/iod ^c	2.5	26%
Quercetin/iod/NPG ^c	6.3	60%
NPG/iod ^d	1.7	47%
Quercetin/iod/NPG ^d	5.3	57%

^a: maximum rates of photopolymerization, calculated from the maximum of the first derivative of the double bond conversions versus time curves during photopolymerization;

^b: final double bond conversions after photopolymerization for 300 s;

^c: photopolymerization under the LED@410 nm;

^d: photopolymerization under the LED@445 nm

Photopolymerizations of a triacrylate monomer, TMPTA, initiated by quercetin/NPG/iod (0.5%/2%/2%, wt) and NPG/iod (0.5%/2% or 2%/2%, wt) were carried out upon irradiation with LED@410 and LED@445 nm (Figure 2.5). In Figure 2.5a (red and green curves), the photopolymerization of TMPTA initiated by quercetin/iod/NPG (0.5%/2%/2%, wt) showed the same final FC as that of NPG/iod (2%/2%, wt) (FC = 53%) upon irradiation with the LED@410 nm in laminate, in accordance with the results of the photopolymerization of Bis-GMA/TEGDMA (70%/30%, wt). In Figure 2.5b (red and green curves), quercetin reduced the R_p of TMPTA while improved FC of TMPTA simultaneously upon exposure to LED@445 nm. Quercetin/NPG/iod (0.5%/2%/2%, wt) and NPG/iod (2%/2%, wt) presented lower initiation ability under the irradiation with LED@445 nm in the photopolymerization of TMPTA in comparison to the photopolymerization of Bis-GMA/TEGDMA (70%/30%, wt). The radical

generating rate cannot compensate for the oxygen inhibition effect because the fluidic formula of TMPTA allowed oxygen diffusion and the conserved oxygen in the formula to move freely. The effect of NPG concentration (0.5 wt% and 2 wt%) in a two-component system, NPG/Iod, on photopolymerization of TMPTA was reported in Figure 2.5a. The more concentrated NPG formula (2 wt%) resulted in higher FC (53%) of TMPTA compared to that of the diluter NPG formula (0.5 wt%, FC = 36%). Under the irradiation with LED@445 nm, NPG/Iod (0.5 wt%/2 wt%) led to an undesirable photopolymerization profile of TMPTA (Figure 2.5b black curve, FC = 8%), whereas the FC of TMPTA was improved to 30% by the additional 1.5 wt% NPG.

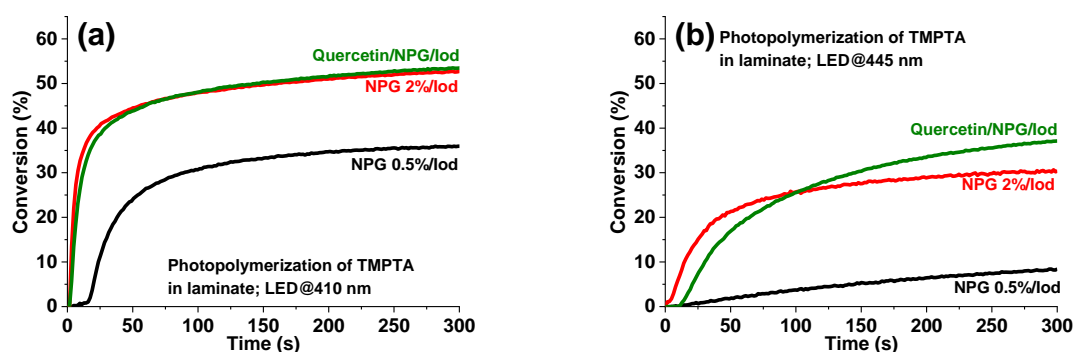


Figure 2.5. Photopolymerization profiles (double bond conversions vs time) of TMPTA in laminate in the presence of NPG- and quercetin-based PISs (quercetin-based PIS: quercetin: 0.5 wt%, NPG: 2 wt%, Iod: 2 wt%; NPG-based PISs: NPG: 0.5 wt% or 2 wt%, Iod: 2 wt%) upon exposure to (a) LED@410 nm (110 mW cm^{-2}) and (b) LED@445 nm (80 mW cm^{-2}).

In Figure 2.6, DVE-3 was used to investigate the photoinitiation abilities of quercetin- and morin-based PISs in cationic photopolymerization. Quercetin/Iod (0.5%/2%, wt) initiated polymerization of DVE-3 with a shorter induction period (25 s) than morin/Iod (0.5%/2%, wt) system (104 s). This could be ascribed to a higher oxygen tolerance of quercetin/Iod. Meanwhile, the quercetin/Iod (0.5%/2%, wt) couple converted 89% ene groups of DVE-3, while the morin/Iod system only resulted in 78% conversion of ene groups.

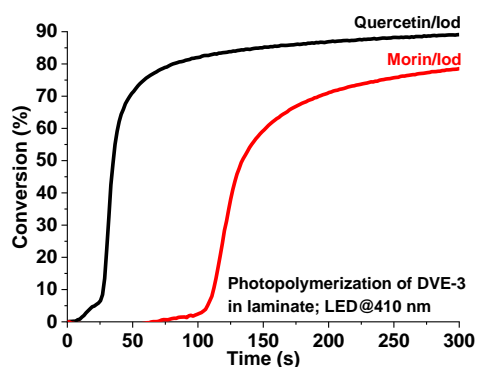


Figure 2.6. Cationic photopolymerization profiles (double-bond conversions vs time) of DVE-3 in laminate in the presence of morin- and quercetin-based PISs (quercetin or morin: 0.5 wt%; Iod: 2 wt%) upon exposure to LED@410 nm.

The photopolymerization of thiol-ene, i.e., DVE-3/TriThiol blend (1:1 by functional groups), was carried out with quercetin/Iod (0.5%/2%, wt) by FTIR (Figure 2.7a). In the presence of TriThiol, DVE-3 was entirely photopolymerized, which was initiated by quercetin/Iod (0.5%/2%, wt). The thiol-ene photopolymerization under the irradiation of LED@410 nm started after 8-s induction period and ended up with FC (DVE-3) of 100% and FC (TriThiol) of 51%. Compared to the 15-s induction period of DVE-3 photoinitiated homopolymerization with FC of 89% (Figure 2.6 and Figure 2.7a), the induction period of thiol-ene crosslinking of DVE-3/TriThiol was shortened, and the FC of that was improved. Trione, a trivinyl monomer, in replacement of DVE-3, was also studied as the partner of TriThiol in thiol-ene photopolymerization in the presence of quercetin/Iod (0.5%/2%, wt) upon exposure to LED@410 nm in laminate (Figure 2.7b). The double bond conversion of Trione and the thiol bond conversion of TriThiol reached to approximately the same FC ($\approx 80\%$). Interestingly, unequal consumption of thiol and ene was observed in DVE-3/TriThiol blend but not in Trione/TriThiol blend even though the blend had been prepared in equal functional group ratio. This was attributed to the fact that DVE-3 underwent homopolymerization and thiol-ene reaction simultaneously. The occurrence of homopolymerization depended on the initiation mechanism. It was challenging for Trione to undergo homopolymerization due to its “degradative chain transfer,”⁴⁵ and only thiol-ene reaction occurred in the Trione/TriThiol blend system resulting in equal consumption of thiol and ene.⁴⁶

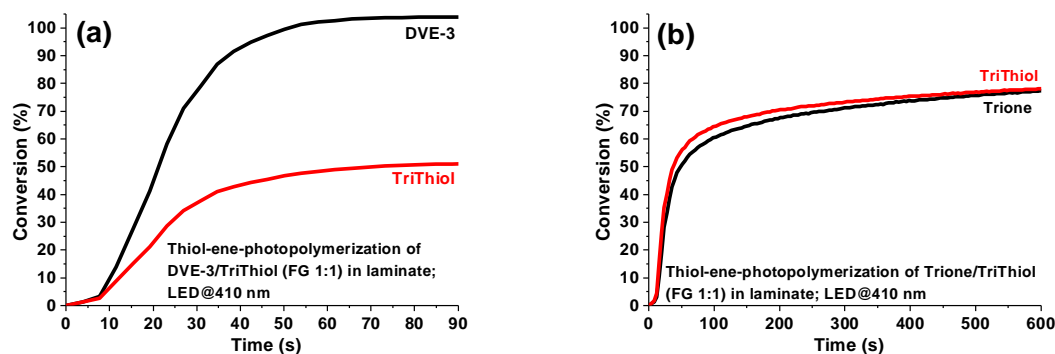


Figure 2.7. Thiol-ene photopolymerization profiles (a) (double-bond conversions vs time) of DVE-3 and (thiol bond conversions vs time) of TriThiol and (b) (double-bond conversions vs time) of Trione and (thiol bond conversions vs time) of TriThiol in the presence of PIS quercetin/Iod (0.5%/2%, wt) in laminate upon exposure to LED@410 nm. (Double-bond conversions: black curves; thiol bond conversions: red curves; ene:thiol = 1:1)

2.8 Conclusion

In the present work, the photochemical mechanism and the photoinitiation ability of penta-hydroxy flavone derivatives, quercetin, and morin, were demonstrated. The interaction between excited PHF and Iod generated active species able to initiate free radical, cationic and thiol-ene photopolymerization upon exposure to blue LED@410 nm or LED@445 nm. The addition of additives to two-component PISs can enhance polymerization efficiency. Furthermore, quercetin improved the photoinitiation ability of a well-studied efficient CTC (i.e., NPG/Iod) under mild blue-light irradiation (LED@445 nm), as the light absorption profile of quercetin was overlapped with the emission wavelength of the irradiation source. The addition of thiol-substituted molecules enhanced the FC of polymerizable vinyl significantly to full conversion in the presence of quercetin/Iod system under the irradiation of blue LED@410 nm, which further solidified the cured materials. The EPR-ST experiment verified the production of the phenyl radicals generated from Iod through the interaction with excited quercetin.

2.9 References:

- (1) Al Mousawi, A.; Garra, P.; Dumur, F.; Graff, B.; Fouassier, J. P.; Lalevée, J. Flavones as natural photoinitiators for light mediated free - radical polymerization via light emitting diodes. *J. Polym. Sci.* **2020**, *58* (2), 254-262.
- (2) Al Mousawi, A.; Garra, P.; Schmitt, M.; Toufaily, J.; Hamieh, T.; Graff, B.; Fouassier, J. P.; Dumur, F.; Lalevée, J. 3-Hydroxyflavone and N-Phenylglycine in High Performance Photoinitiating Systems for 3D Printing and Photocomposites Synthesis. *Macromolecules* **2018**, *51* (12), 4633-4641.

- (3) Zhu, D.; Peng, X.; Xiao, P. Penta - Hydroxy Flavones - Based Photoinitiating Systems for Free Radical, Cationic, and Thiol - Ene Polymerization upon Exposure to Mild Blue LEDs. *Macromol. Mater. Eng.* **2021**, 306 (6), 2100059.
- (4) Bowman, C. N.; Kloxin, C. J. Toward an enhanced understanding and implementation of photopolymerization reactions. *AIChE J.* **2008**, 54 (11), 2775-2795.
- (5) Fouassier, J.-P. *Photoinitiation, Photopolymerization, and Photocuring: Fundamentals and Applications*; Hanser Pub Inc, 1995.
- (6) Hiramoto, K.; Yamate, Y.; Kobayashi, H.; Ishii, M. Long-term ultraviolet A irradiation of the eye induces photoaging of the skin in mice. *Archives of Dermatological Research* **2012**, 304 (1), 39-45.
- (7) Xu, Y.; Shao, Y.; Zhou, J.; Voorhees, J. J.; Fisher, G. J. Ultraviolet irradiation-induces epidermal growth factor receptor (EGFR) nuclear translocation in human keratinocytes. *Journal of Cellular Biochemistry* **2009**, 107 (5), 873-880.
- (8) El-Abaseri, T. B.; Putta, S.; Hansen, L. A. Ultraviolet irradiation induces keratinocyte proliferation and epidermal hyperplasia through the activation of the epidermal growth factor receptor. *Carcinogenesis* **2006**, 27 (2), 225-231.
- (9) Anderson, R. R.; Parrish, J. A. The optics of human skin. *Journal of Investigative Dermatology* **1981**, 77 (1), 13-19.
- (10) Baralle, A.; Garra, P.; Graff, B.; Morlet-Savary, F.; Dietlin, C.; Fouassier, J. P.; Lakhdar, S.; Lalevée, J. Iodinated Polystyrene for Polymeric Charge Transfer Complexes: Toward High-Performance Near-UV and Visible Light Macrophotoinitiators. *Macromolecules* **2019**, 52 (9), 3448-3453.
- (11) Zhang, X.; Xi, W.; Gao, G.; Wang, X.; Stansbury, J. W.; Bowman, C. N. o-Nitrobenzyl-Based Photobase Generators: Efficient Photoinitiators for Visible-Light Induced Thiol-Michael Addition Photopolymerization. *ACS Macro Lett.* **2018**, 7 (7), 852-857.
- (12) Zhang, J.; Launay, K.; Hill, N. S.; Zhu, D.; Cox, N.; Langley, J.; Lalevée, J.; Stenzel, M. H.; Coote, M. L.; Xiao, P. Disubstituted Aminoanthraquinone-Based Photoinitiators for Free Radical Polymerization and Fast 3D Printing under Visible Light. *Macromolecules* **2018**, 21 (24), 10104-10112.
- (13) Zhang, J.; Lalevée, J.; Morlet-Savary, F.; Graff, B.; Xiao, P. Photopolymerization under various monochromatic UV/visible LEDs and IR lamp: Diamino-anthraquinone derivatives as versatile multicolor photoinitiators. *European Polymer Journal* **2018**, 112, 591-600.
- (14) Zhang, C.; Dong, Q.; Liang, K.; Zhou, D.; Yang, H.; Liu, X.; Xu, W.; Zhou, Y.; Xiao, P. Photopolymerizable thiol-acrylate maleiated hyaluronic acid/thiol-terminated poly(ethylene glycol) hydrogels as potential in-situ formable scaffolds. *International Journal of Biological Macromolecules* **2018**, 119, 270-277.
- (15) Wang, J.; Stanic, S.; Altun, A. A.; Schwentenwein, M.; Dietliker, K.; Jin, L.; Stampfl, J.; Baudis, S.; Liska, R.; Grutzmacher, H. A highly efficient waterborne photoinitiator for visible-light-induced three-dimensional printing of hydrogels. *Chemical communications (Cambridge, England)* **2018**, 54 (8), 920-923.
- (16) Eibel, A.; Radebner, J.; Haas, M.; Fast, D. E.; Freißmuth, H.; Stadler, E.; Faschauner, P.; Torvisco, A.; Lamparth, I.; Moszner, N.; et al. From mono- to tetraacylgermanes: extending the scope of visible light photoinitiators. *Polym. Chem.* **2018**, 9 (1), 38-47.
- (17) Abdallah, M.; Le, H.; Hijazi, A.; Schmitt, M.; Graff, B.; Dumur, F.; Bui, T.-T.; Goubard, F.; Fouassier, J.-P.; Lalevée, J. Acridone derivatives as high performance visible light photoinitiators for cationic and radical photosensitive resins for 3D printing technology and for low migration photopolymer property. *Polymer* **2018**, 159, 47-58.
- (18) Radebner, J.; Eibel, A.; Leypold, M.; Gorsche, C.; Schuh, L.; Fischer, R.; Torvisco, A.; Neshchadin, D.; Geier, R.; Moszner, N.; et al. Tetraacylgermanes: Highly Efficient Photoinitiators for Visible-Light-Induced Free-Radical Polymerization. *Angewandte Chemie, International Edition* **2017**, 56 (11), 3103-3107.

- (19) Zhang, J.; Xiao, P.; Morlet-Savary, F.; Graff, B.; Fouassier, J. P.; Lalevée, J. A known photoinitiator for a novel technology: 2-(4-methoxystyryl)-4,6-bis(trichloromethyl)-1,3,5-triazine for near UV or visible LED. *Polym. Chem.* **2014**, *5* (20), 6019-6026.
- (20) Tehfe, M.-A.; Lalevée, J.; Telitel, S.; Contal, E.; Dumur, F.; Gigmès, D.; Bertin, D.; Nechab, M.; Graff, B.; Morlet-Savary, F.; et al. Polyaromatic Structures as Organo-Photoinitiator Catalysts for Efficient Visible Light Induced Dual Radical/Cationic Photopolymerization and Interpenetrated Polymer Networks Synthesis. *Macromolecules* **2012**, *45* (11), 4454-4460.
- (21) Aydoğan, B.; Gunbas, G. E.; Durmus, A.; Toppare, L.; Yagci, Y. Highly Conjugated Thiophene Derivatives as New Visible Light Sensitive Photoinitiators for Cationic Polymerization. *Macromolecules* **2010**, *43* (1), 101-106.
- (22) Yang, J.; Liao, W.; Xiong, Y.; Wu, Q.; Wang, X.; Li, Z.; Tang, H. Naphthalimide dyes: Polymerizable one-component visible light initiators. *Dyes and Pigments* **2018**, *148*, 16-24.
- (23) Mula, S.; Ray, A. K.; Banerjee, M.; Chaudhuri, T.; Dasgupta, K.; Chattopadhyay, S. Design and Development of a New Pyrromethene Dye with Improved Photostability and Lasing Efficiency: Theoretical Rationalization of Photophysical and Photochemical Properties. *Journal of Organic Chemistry* **2008**, *73* (6), 2146-2154.
- (24) Zhou, J.; Allonas, X.; Liu, X. Synthesis and characterization of organozirconiums with type-II photoinitiator ligands as multifunctional photoinitiators for free radical photopolymerization. *Journal of Photochemistry and Photobiology A: Chemistry* **2018**, *356*, 580-586.
- (25) Kocaadam, B.; Sanlier, N. Curcumin, an active component of turmeric (*Curcuma longa*), and its effects on health. *Critical Reviews in Food Science and Nutrition* **2017**, *57* (13), 2889-2895.
- (26) Boeira, P. O.; Meereis, C. T. W.; Suárez, C. E. C.; de Almeida, S. M.; Piva, E.; da Silveira Lima, G. Coumarin-based iodonium hexafluoroantimonate as an alternative photoinitiator for experimental dental adhesives resin. *Applied Adhesion Science* **2017**, *5* (1), 1-11.
- (27) Han, W.; Fu, H.; Xue, T.; Liu, T.; Wang, Y.; Wang, T. Facilely prepared blue-green light sensitive curcuminoids with excellent bleaching properties as high performance photosensitizers in cationic and free radical photopolymerization. *Polym. Chem.* **2018**, *9* (14), 1787-1798.
- (28) Arakawa, C.; Ng, R.; Tan, S.; Kim, S.; Wu, B.; Lee, M. Photopolymerizable chitosan-collagen hydrogels for bone tissue engineering. *Journal of Tissue Engineering and Regenerative Medicine* **2017**, *11* (1), 164-174.
- (29) Batchelor, R. R.; Kwandou, G.; Spicer, P. T.; Stenzel, M. H. (-)-Riboflavin (vitamin B2) and flavin mononucleotide as visible light photo initiators in the thiol-ene polymerisation of PEG-based hydrogels. *Polym. Chem.* **2017**, *8* (6), 980-984.
- (30) Applegate, M. B.; Partlow, B. P.; Coburn, J.; Marelli, B.; Pirie, C.; Pineda, R.; Kaplan, D. L.; Omenetto, F. G. Photocrosslinking of Silk Fibroin Using Riboflavin for Ocular Prostheses. *Adv. Mater.* **2016**, *28* (12), 2417-2420.
- (31) Zhang, J.; Hill, N.; Lalevée, J.; Fouassier, J.-P.; Zhao, J.; Graff, B.; Schmidt, T. W.; Kable, S. H.; Stenzel, M. H.; Coote, M. L.; et al. Multihydroxy-Anthraquinone Derivatives as Free Radical and Cationic Photoinitiators of Various Photopolymerizations under Green LED. *Macromolecular Rapid Communications* **2018**, *39* (19), 1800172.
- (32) Wang, G.; Hill, N. S.; Zhu, D.; Xiao, P.; Coote, M. L.; Stenzel, M. H. Efficient Photoinitiating System Based on Diaminoanthraquinone for 3D Printing of Polymer/Carbon Nanotube Nanocomposites under Visible Light. *ACS Appl. Polym. Mater.* **2019**, *1* (5), 1129-1135.
- (33) Zhang, J.; Xiao, P.; Dietlin, C.; Campolo, D.; Dumur, F.; Gigmès, D.; Morlet-Savary, F.; Fouassier, J.-P.; Lalevée, J. Cationic Photoinitiators for Near UV and Visible LEDs: A Particular Insight into One-Component Systems. *Macromolecular Chemistry and Physics* **2016**, *217* (Copyright (C) 2017 American Chemical Society (ACS). All Rights Reserved.), 1214-1227, 10.1002/macp.201500546.

- (34) Xiao, P.; Dumur, F.; Graff, B.; Fouassier, J. P.; Gignes, D.; Lalevée, J. Cationic and Thiol–Ene Photopolymerization upon Red Lights Using Anthraquinone Derivatives as Photoinitiators. *Macromolecules* **2013**, *46* (17), 6744-6750.
- (35) Hostetler, G. L.; Ralston, R. A.; Schwartz, S. J. Flavones: Food Sources, Bioavailability, Metabolism, and Bioactivity. *Advances in Nutrition* **2017**, *8* (3), 423-435.
- (36) He, B.-H.; He, J.; Wang, G.-X.; Liu, L.-C.; Wu, H.; Zhong, M. Photoinduced controlled/“living” polymerization of methyl methacrylate with flavone as photoinitiator. *Journal of Applied Polymer Science* **2016**, *133* (34), 43845.
- (37) Condat, M.; Babinot, J.; Tomane, S.; Malval, J.-P.; Kang, I.-K.; Spillebout, F.; Mazeran, P.-E.; Lalevée, J.; Andalloussi, S. A.; Versace, D.-L. Development of photoactivable glycerol-based coatings containing quercetin for antibacterial applications. *RSC Advances* **2016**, *6* (22), 18235-18245.
- (38) Abou-Hatab, S.; Spata, V. A.; Matsika, S. Substituent Effects on the Absorption and Fluorescence Properties of Anthracene. *Journal of Physical Chemistry A* **2017**, *121* (6), 1213-1222.
- (39) Zhang, J.; Lalevee, J.; Hill, N. S.; Peng, X.; Zhu, D.; Kiehl, J.; Morlet-Savary, F.; Stenzel, M. H.; Coote, M. L.; Xiao, P. Photoinitiation Mechanism and Ability of Monoamino-Substituted Anthraquinone Derivatives as Cationic Photoinitiators of Polymerization under LEDs. *Macromolecular Rapid Communications* **2019**, *40* (16), 1900234.
- (40) Lalevée, J.; Graff, B.; Allonas, X.; Fouassier, J. P. Aminoalkyl Radicals: Direct Observation and Reactivity toward Oxygen, 2,2,6,6-Tetramethylpiperidine-N-oxyl, and Methyl Acrylate. *The Journal of Physical Chemistry A* **2007**, *111* (30), 6991-6998.
- (41) Tehfe, M. A.; Lalevée, J.; Telitel, S.; Contal, E.; Dumur, F.; Gignes, D.; Bertin, D.; Nechab, M.; Graff, B.; Morlet-Savary, F.; et al. Polyaromatic Structures as Organo-Photoinitiator Catalysts for Efficient Visible Light Induced Dual Radical/Cationic Photopolymerization and Interpenetrated Polymer Networks Synthesis. *Macromolecules* **2012**, *45* (11), 4454-4460.
- (42) Lalevée, J.; Blanchard, N.; Tehfe, M. A.; Morlet-Savary, F.; Fouassier, J. P. Green Bulb Light Source Induced Epoxy Cationic Polymerization under Air Using Tris(2,2'-bipyridine)ruthenium(II) and Silyl Radicals. *Macromolecules* **2010**, *43* (24), 10191-10195.
- (43) Layliev, E.; Golub-Evans, J. Chapter 15 - Direct Veneers. In *Contemporary Esthetic Dentistry*, Freedman, G. Ed.; Mosby, 2012; pp 405-435.
- (44) Garra, P.; Caron, A.; Al Mousawi, A.; Graff, B.; Morlet-Savary, F.; Dietlin, C.; Yagci, Y.; Fouassier, J.-P.; Lalevée, J. Photochemical, Thermal Free Radical, and Cationic Polymerizations Promoted by Charge Transfer Complexes: Simple Strategy for the Fabrication of Thick Composites. *Macromolecules* **2018**, *51* (19), 7872-7880.
- (45) Matsumoto, A. Polymerization of multiallyl monomers. *Progress in Polymer Science* **2001**, *26* (2), 189-257.
- (46) Hoyle, C. E.; Lee, T. Y.; Roper, T. Thiol-enes: Chemistry of the past with promise for the future. *Journal of Polymer Science Part A: Polymer Chemistry* **2004**, *42* (21), 5301-5338.
- (47) Hata, E.; Mitsube, K.; Momose, K.; Tomita, Y. Holographic nanoparticle-polymer composites based on step-growth thiol-ene photopolymerization. *Opt. Mater. Express* **2011**, *1* (2), 207-222.

2.10 Supporting Information

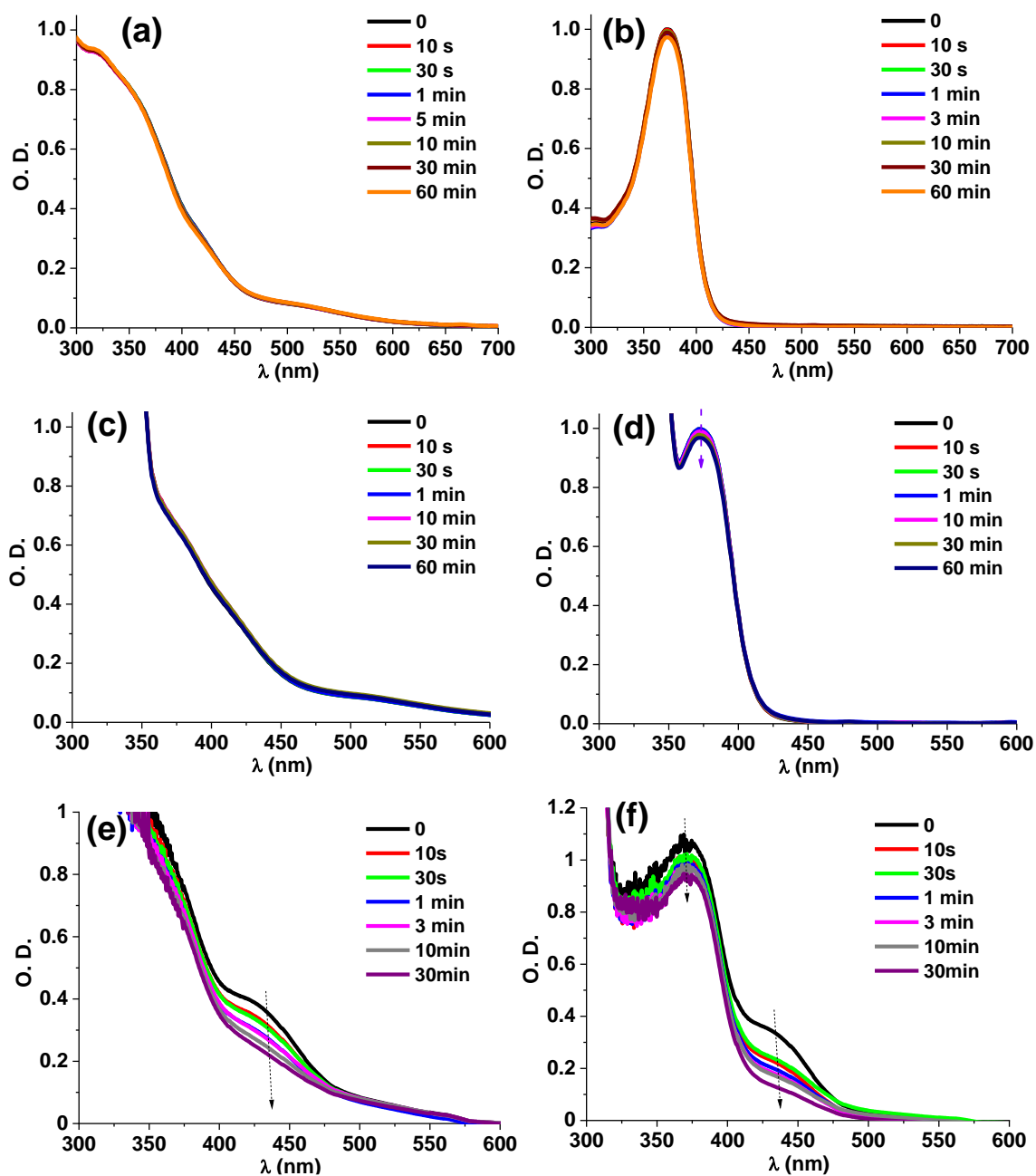


Figure S2.1.. Steady state photolysis of (a) Morin, (b) Quercetin, (c) Morin/EDB, (d) Quercetin/EDB, (e) Morin/NPG and (f) Quercetin/NPG in ethanol ($[EDB] = 18 \text{ mM}$, $[NPG] = 2 \text{ mM}$); UV-vis spectra recorded at different irradiation time; UV LED@394 nm irradiation (4 mW cm^{-2}).

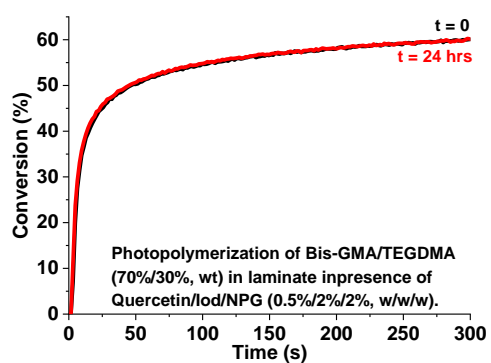


Figure S2.2. Photopolymerization profiles (double bond conversions vs time) of Bis-GMA/TEGDMA blend (70%/30%, w/w) along with storage time in laminate in presence of Quercetin/Iod/NPG (0.5%/2%/2%, w/w/w) PIS upon exposure of LED@410 nm (110 mW cm^{-2}).

Chapter 5 Indigo carmine: a natural photoinitiator extracted from *Indigofera* for the 3D printing application of shape memory hydrogel

5.1 Preface

In the previous chapters, the investigated photoinitiators were efficient in their sodium salt forms, thus additional NaOH was introduced to induce the formation of their conjugate base. A natural sodium salt dye could significantly reduce the amount of NaOH. Therefore, the indigo carmine was investigated as a natural photoinitiator candidate. Indigo carmine is a natural sodium salt (Scheme 5.1) and was originally extracted from *Indigofera*.^{1,2} Furthermore, indigo carmine has been approved as a food colorant,² guaranteeing its biocompatibility. To achieve the aforementioned objectives, the mechanism of photoreaction between indigo carmine and a selected coinitiator has been preliminarily revealed. Thereafter, the photoinitiation ability of indigo carmine has been investigated in diverse formulations. The composition of the formulation has been screened, and the photoinitiation ability of indigo carmine has been optimized. The optimized indigo carmine-based photoinitiating system demonstrated its capability in 3D resins. Additionally, the developed indigo carmine-based 3D resin achieved high-fidelity 3D printing, and an advanced 2D-3D conversion has been afforded upon water immersion and under airdrying.

5.2 Author contributions to the published article

I declare that the published research results enclosed in this chapter are the original work carried out by me for my Ph.D. program at Australian National University.

As the first author, I contributed to the development of the concept, outline of the experiments, data analysis, figure production, and preparation of the original draft, under the supervision of my primary supervisor, Prof. Pu Xiao.

5.3 Publication status

The published manuscript entitled “Indigo carmine: A base and neutral electrolyte-mediated photoinitiator for 3D printing in high fidelity” is presented as a chapter with the following revision: the discussion of cage-escape yields effect on the photoinitiation ability of indigo carmine is supplemented in 5.7.3. The article with supporting information is reproduced with permission³. Copyright 2022, Elsevier B.V. in this chapter. This manuscript is published in the journal **Additive Manufacturing** in 2022, and the citation of the published manuscript is:

Zhu, D.; Peng, X.; Xiao, P. Indigo carmine: A base and neutral electrolyte-mediated photoinitiator for 3D printing in high fidelity. *Addit. Manuf.* **2022**, *59*, 103154. DOI: 10.1016/j.addma.2022.103154.

5.4 Abstract

Volumetric additive manufacturing with light is an advanced technology in diverse conventional fields. However, with the raising awareness of environmental concerns and the growing interest in biomedical applications, the safety and water solubility of the existing photoinitiators are challenged. Herein, we developed a photoinitiating system based on a blue food colorant, i.e., indigo carmine. The indigo carmine-based photoinitiating system induced a rapid photochemical reaction and photobleaching under blue and green LEDs in the alkaline medium. The unprecedented photoinitiation ability of the indigo carmine-based photoinitiating system in terms of rate of photopolymerization and the final monomer conversion was achieved under the irradiation of low-intensity light sources. Subsequently, a sophisticated 3D printing in high fidelity was carried out and a 2D seashell was designed and printed with the function of 2D-3D reversible switching. These findings demonstrated that the indigo carmine-based photoinitiating system could resolve the safety and water solubility challenges and be involved in the 3D printing of biomedical materials.

5.5 Introduction

The development of light-based 3D printing has improved and replaced conventional fabrication techniques in diverse applications.⁴⁻¹⁵ The existing and recently developed photoinitiators for vat photopolymerization/3D printing mainly exhibit hydrophobic properties,¹⁶ limiting their capabilities of broadening the applications involving waterborne materials. As with the hydrogel formation process, the 3D printing technique can produce complex and designed hydrogel structures for biomedical applications in drug delivery, cell delivery, and scaffold, etc.^{4, 17-20} To meet the increasing demands of hydrogel-involved biomedical applications, several efforts have been devoted to exploring water-compatible photoinitiators. For instance, the non-covalent and covalent strategies of solubility modification were developed to allow numerous hydrophobic photoinitiators to be involved in the hydrogel formation. Specifically, for the non-covalent strategies, the nanoparticles of microemulsion formed by surfactant encapsulating the commercially available 2,4,6-trimethylbenzoyl-diphenylphosphine oxide (TPO) and 2,2-dimethoxyphenylacetophenone (DMPA).^{21, 22} In addition, the encapsulation of hydrophobic photoinitiators (e.g., a developed naphthalimide-derived photoinitiator and 2-hydroxy-2-methyl-1-phenylpropan-1-one) into the cavities of cyclodextrins can endow the

formed non-bonding host-guest complexes with hydrophilic property which can be used as waterborne UV/blue light sensitive photoinitiators and successfully applied in photopolymerization of hydrophilic monomers.^{23, 24} Alternatively, for the covalent strategy, the phenylbis(2,4,6-trimethylbenzoyl)phosphine oxide (BAPO) grafted onto cellulose nanocrystals (CNCs) or poly(ethylene glycol) (PEG) via covalent bonds were prepared and exhibited exceedingly photoinitiation ability to hydrogel fabrication.^{25, 26} Although the solubility modification strategies expanded the scope of water-compatible photoinitiators, and the abovementioned water-dispersible photoinitiators substantially exhibited efficient photoinitiation abilities, these approaches can induce the steric effect adversely affecting the photoinitiation efficiency of the encapsulated or grafted hydrophobic photoinitiators dispersed in the prepolymers.²⁴ Considering the above limitation, water-soluble photoinitiators are more favorable. The commonly used hydrophilic photoinitiators are 2-hydroxy-4'--(2-hydroxyethoxy)-2-methylpropiophenone (Irgacure 2959) and lithium phenyl-2,4,6-trimethylbenzoylphosphinate (LAP).^{6, 18, 25-29} Despite the excellent photoinitiation ability, Irgacure 2959 and LAP are commonly used under the irradiation of ultraviolet (UV) irradiation (~365 nm) for photopolymerization,^{6, 27, 28} which can cause human health and environmental issues.³⁰⁻³³ Therefore, it is desirable to develop visible-light sensitive waterborne photoinitiators due to the safety and environment concerns.³⁴ Specifically, several salts, inspired by LAP, of commonly used hydrophobic photoinitiators were produced. For instance, the metal salts of BAPO and 2-benzyl-2-(dimethylamino)1-(4-morpholinophenyl)-1-butanone (BDMB), and the ammonium salts of TPO were designed and developed, which exhibited the absorption around the violet light range (~440 nm).^{19, 25, 29, 35-37} Despite the exceptional water solubility of the metal salts, the cytotoxicity has been insufficiently investigated. Only few literature²⁹ explicitly stated the low-cytotoxicity of water-soluble photoinitiator salts (i.e., the developed ammonium salts of BAPO). Concerning the favorable visible light absorption and cytocompatibility, a cell staining dye, eosin Y and a food content/dietary supplement, riboflavin, were well-investigated,³⁸⁻⁴¹ and they display light absorption in the blue-green light range,^{27, 36, 37, 40} with which the thiol-ene hydrogelation was successfully achieved under the blue light irradiation.^{38, 41} Moreover, several planar and simple structures (e.g., planar sheets, rectangles, letters, planar honeycombs, etc.) have been fabricated via 3D printing technology with eosin Y- and riboflavin-based photoinitiating systems.⁴²⁻⁴⁸ However, considering the advanced applications (e.g., implantation with neural regeneration devices) of 3D printing, the printing complexity and shape-fidelity are indispensable.⁴⁹

To address the abovementioned challenges, the exploration and development of water-soluble, visible-light-sensitive, and low-toxic photoinitiators capable of performing rapid and

high-fidelity 3D printing are highly demanded. Here, we explored a promising dye, indigo carmine (IDGCM), which is originally discovered in plants of the genus *Indigofera*,^{1, 50} playing a role as a food colorant.⁵¹ The blue appearance and the sodium salt form are indicative of visible light absorption (400 nm – 700 nm in neutral solution) and water-soluble properties, respectively. Besides, the safe threshold of IDGCM for cats/dogs and rats is 250 mg/kg body weight and 8259 mg/kg body weight/day, respectively.^{52, 53} For humans, there is no eye or skin irritant effect of IDGCM, and the average daily intake of 5 mg/kg body weight/day was established by European Food Safety Authority.^{2, 50, 53} Furthermore, IDGCM is a commercially available pH indicator (pH 11.4 – 13.0), and its light absorption can be mediated by basicity.⁵⁴ On the basis of pH-mediated photophysical properties reported previously,⁵⁵⁻⁶⁰ IDGCM demonstrates potential interest in pH-mediated photopolymerization. However, pH-mediated photopolymerization was scarcely investigated with few examples.⁶¹ Specifically, the *N*-phenyl-*p*-phenylenediamine (PPD) was a coinitiator in a ruthenium-complex-based photoinitiating system whose photoinitiation ability was dominated by the pH-mediated reversible electrochemical reaction (protonation-deprotonation reaction) of PPD.⁶¹

The photoinitiation ability of IDGCM mediated by basicity under visible light was investigated using the real-time Fourier-transform infrared spectroscopy (RT-FTIR), and the relevant photochemical mechanism of IDGCM-based photoinitiating systems in alkaline and the neutral salted solution was investigated using ultraviolet-visible (UV-vis) spectrophotometer and electron paramagnetic resonance (EPR) technique. As with the knowledge of the rapid photopolymerization of the poly(ethylene glycol) diacrylate M_n 700 (PEGDA 700)/water blend (25 mM NaOH) upon exposure to 400 nm (6.4 mW cm^{-2}), we also demonstrated the 3D printing settings using a planar cat coin model for the further sophisticated structure. Ascribed to the dual role of IDGCM (photoinitiator and photoabsorber), a topography with exceptional shape fidelity was successfully fabricated via 3D printing.^{62, 63} More interestingly, the reversible 2D-3D transition of a planar sheet produced by vat photopolymerization was stimulated by the presence and the absence of NaCl aqueous solution.

5.6 Experimental

5.6.1 Materials

Indigo Carmine (IDGCM), diphenyliodonium hexafluorophosphate (Iod), 2-hydroxy ethyl acrylate (HEA), and poly(ethylene glycol) diacrylate (PEGDA) M_n 700, 525, 200 were obtained from Sigma Aldrich and used as delivered. The chemical structures of mentioned compounds are summarized in Scheme 5.1.

5.6.6 Photorheology

Photorheological measurements were performed in parallel plate mode using an Anton Paar MCR 702 multidrive rheometer under the irradiation of one of the abovementioned LEDs. The sample was placed under the plate geometry (PP25) with a 25 mm diameter at the gap between the two plates set to 0.02 mm – 1.00 mm. The tests were conducted at a constant temperature (25 °C) and constant normal force of 0 N, under the constant shear strain of 0.1% and constant frequency of 1 Hz. The LED placed under the lower plate was turned on after 70 s upon stabilizing the system. Concomitant changes in the moduli and loss factor of investigated formulations during photopolymerization were measured as a function of exposure time.

5.6.7 3D printing

The 3D resin was prepared by adding the homogeneous aqueous solution of IDGCM and NaOH into the transparent solution of Iod in PEGDA 700 dropwise. The resultant mixture was stirred at ambient temperature until thoroughly mixed and then used for 3D printing. The 3D printing was performed layer-by-layer (thickness: 0.020 mm) using a Digital Light Processing (DLP) 3D printer (MAKEX) which is equipped with a LED@405 nm (3 mW cm⁻²).

5.7 Results and discussion

5.7.1 Light absorption properties of IDGCM

The UV-vis spectra of IDGCM in different solutions demonstrated its light absorption properties in the visible range (Figure 5.1). The light absorption maxima (λ_{max}), extinction coefficients at the maximum absorption (ϵ_{max}) and used LEDs (ϵ_{400} , ϵ_{410} and ϵ_{530}) are summarized in Table 5.1. The maximum absorptions of IDGCM in the different aqueous solutions were all located at 610 nm (Figure 5.1). Specifically, to determine the effect of ionic strength and/or basicity on light absorption of IDGCM, NaCl (25 mM) and NaOH (25 mM) were introduced to the solution of IDGCM in DI water. The ionic strength exhibited a bare effect on the light absorption profile of IDGCM in neutral aqueous solution according to the substantially overlapped light absorption profiles of IDGCM in DI water and aq. NaCl (25 mM) (Figure 5.1). In contrast with NaCl, the introduction of NaOH sharply altered the light absorption profile of IDGCM (Figure 5.1), especially the extinction coefficients. Interestingly, the alkaline milieu compromised the green light absorption (505 nm - 650 nm) and improved the blue light absorption (400 nm - 500 nm) and red-light absorption (675 nm – 800 nm) of IDGCM (Figure 5.1). The rising peaks centered at 440 nm and 760 nm can be assigned to the leuco form of IDGCM⁶⁶⁻⁶⁸ and the

anion species formed via deprotonation of N-H⁵⁴ (Scheme S5.1). The IDGCM-leuco allows the rotation of the central C-C bond and subsequently the production of emissive species.⁶⁶

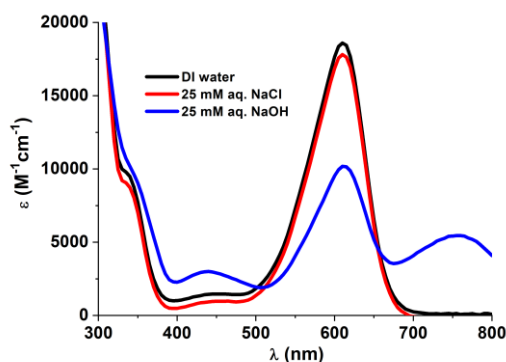


Figure 5.1. UV-vis absorption of IDGCM in water (black), 25 mM aq. NaCl (red), and 25 mM aq. NaOH (blue).

Table 5.1. The extinction coefficients of IDGCM in neutral and alkaline solution at their absorption maxim, 410 nm, and 530 nm.

	λ_{\max}	ϵ_{\max} ($M^{-1} \text{ cm}^{-1}$)	ϵ_{400} ($M^{-1} \text{ cm}^{-1}$)	ϵ_{410} ($M^{-1} \text{ cm}^{-1}$)	ϵ_{530} ($M^{-1} \text{ cm}^{-1}$)
IDGCM in aq. NaOH	610 nm	10,200	2300	2500	2500
IDGCM in aq. NaCl	610 nm	17,800	500	600	3600
IDGCM in DI water	610 nm	18,600	1000	1100	4100

To investigate the effect of ionic strength and/or basicity on photochemical reactions between IDGCM and the coinitiator (Iod) in detail, the steady-state photolysis experiments of IDGCM in the aforementioned aqueous solutions were carried out under the irradiation of LED@410 nm. Upon the irradiation (Reaction 5.1) and with the introduction of Iod, the steady state photolysis of IDGCM was slow in the absence of electrolytes (Figure S5.1a). The addition of electrolytes enhanced the photolysis rate of IDGCM (Figure S5.1b-c). Specifically, as the electrolytes differed in basicity and anion sizes, the effect of electrolytes (i.e., NaOH and NaCl) on the rate of photolysis varied.⁶⁹⁻⁷² With the inherent basicity and the large anion size, OH⁻ can improve the solubility of IDGCM and provide spacious room for IDGCM to approach Iod, hence accelerating the electron transfer process (Reaction 5.2).^{71, 73, 74} The free radicals produced during photolysis via photoinduced electron transfer (Reaction 5.2) were subsequently characterized using EPR-ST technique and were determined as phenyl radicals (Figure 5.2). Notably, besides LED@410 nm, a blue LED with lower intensity (LED@400 nm, 6.4 mW cm⁻²) and green LED (LED@530 nm, 25 mW cm⁻²) can also induce fast photolysis (Figure S5.2). Subsequently, the active species, phenyl radicals, could initiate polymerizations following by propagation (Reaction 5.3 - Reaction 5.5), which will be evaluated using real-time FTIR.

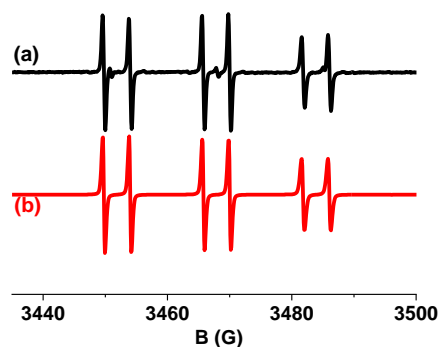
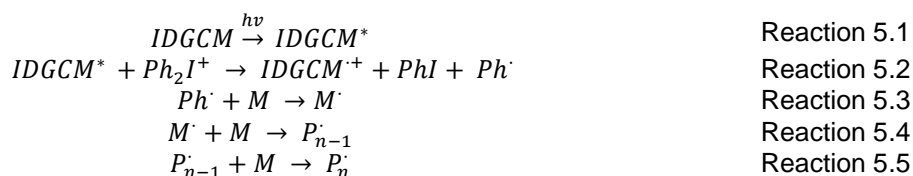


Figure 5.2. EPR spectra of the radicals generated in IDGCM/Iod combination upon exposure to LED@410 nm and trapped by PBN in the aqueous solution of 25 mM NaOH: PBN/phenyl radical adducts formed in IDGCM/Iod system: $a_N = 16$ G, $a_H = 4.23$ G.⁷⁵

5.7.2 The effect of the amount of NaOH, PEGDA, and IDGCM in formulation on photopolymerization of PEGDA

To preliminarily evaluate the effect of basicity on the photoinitiation ability of IDGCM, the photopolymerizations of PEGDA 700/DI water blends were carried out in laminate under LED@410 nm with the addition of diverse concentrations of NaOH in parallel (Figure 5.3). The increased concentration of NaOH facilitated the conversion of the final C=C double bond of acrylates and the maximum rate of polymerization of PEGDA 700 by means of the reduction of electrostatic repulsion⁶¹ until it plateaued and became constant (at 12.5 mM NaOH). In this case, at the higher concentration of OH⁻, the resultant high-density negative charge on IDGCM⁻ reduced the electrostatic repulsion and enhanced attraction between oppositely charged IDGCM⁻ and Iod⁺, which therefore facilitated the collision between IDGCM and Iod. In the same manner, the final C=C conversion and the maximum rate of photopolymerization of HEA reached a plateau at 125 mM NaOH (Figure S5.3). Nevertheless, the solubility of IDGCM was diminished by the overdose of NaOH, thereby reducing the conversion of the double bonds and the rate of polymerization (Figure S5.3), in light of the common-ion effect and basicity effect.^{76, 77} Meanwhile, the PEGDA 700 content in prepolymer dominated the photopolymerization except at boundary conditions. Specifically, the increased PEGDA 700/water ratio promoted the final C=C conversion of PEGDA 700 (Figure S5.4: 40% - 80% PEGDA 700). While at boundary conditions, the distribution of dissolved IDGCM in uncured monomer dominated. Specifically, the insufficient water content limited the dissolution of

IDGCM and NaOH, and subsequently reduced the polymerization of PEGDA 700 (Figure S5.4: 99% PEGDA 700) compared to that of 80% PEGDA 700. In contrast, the higher photoinitiating system distribution in the monomer, due to the lower content of PEGDA 700, drastically enhanced the polymerization of PEGDA 700 (Figure S5.4: 20% PEGDA 700).

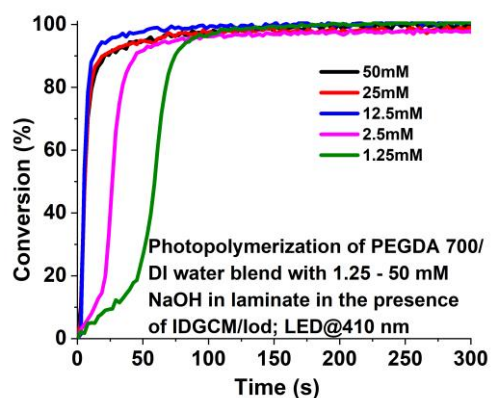


Figure 5.3. Photopolymerization profiles (double bond conversions vs time) of PEGDA 700/water (80%/20%, w/w) in laminate in the presence of IDGCM/Iod (0.5%/2%, wt) with 1.25 mM – 50 mM NaOH upon exposure to the LED@410 nm (110 mW cm^{-2}).

Besides the water content percentage, the concentration of IDGCM can tune the photopolymerization of PEGDA 700/DI water blends. Due to the aforementioned common-ion effect, the amount of IDGCM can also impact the polymerization activity. In detail, under the irradiation of LED@410 nm (110 mW cm^{-2}), the enhancement of conversion and polymerization rate of PEGDA 700 (Figure S5.5a and c: 0.05%-0.3%) was attributed to the increased concentration of IDGCM in formulations. In contrast, excess IDGCM (0.5%) was precipitated and induced $G' > G''$ for the uncured resin at a low thickness of 0.02 mm before irradiation (Figure S5.6: $t = 0 \text{ s}$). Furthermore, the suspended IDGCM problematically impeded light penetration and substantially reduced the conversion and the rate of polymerization of PEGDA 700 (Figure S5.5a and c). A similar result was achieved using the parallel formulations under the irradiation of the blue light with lower intensity (LED@400 nm, 6.4 mW cm^{-2}) (Figure S5.5b and d). In this case, it induced a longer duration of the electron transfer process (Figure S5.2a), slowly consuming the dissolved IDGCM during photolysis. Nevertheless the slow photolysis offered adequate time to reestablish the dynamic equilibrium between the dissolved IDGCM and the excess IDGCM in uncured resins.⁷⁸ Therefore, although the 0.5 wt% IDGCM presented lower C=C conversion of PEGDA 700 than 0.3 wt% IDGCM due to compromised light penetration, it presented a higher rate of polymerization over 0.3 wt% IDGCM. Furthermore, the IDGCM was rapidly bleached over irradiation (Figure S5.7a) and the residual

IDGCM in the resulting polymer can be removed by immersion in DI water overnight (Figure S5.7b).

5.7.3 The effect of chain length of PEGDA, LED and electrolyte on photopolymerization of PEGDA

Besides the concentration and/or the content of components, the number average molecular weight (M_n) of PEGDA, irradiation source and the electrolyte also affect the photopolymerization of PEGDA. Specifically, the higher conversion (Figure 5.4: PEGDA 700 > PEGDA 575 > PEGDA 200) and the shorter induction time (Figure S5.6: PEGDA 700 < PEGDA 575) were observed in the polymerization of the PEGDA with higher M_n , ascribed to the relevant termination rate coefficients.⁷⁹ Typically, the formulation with the increased chain length decelerated the termination rate and hence indirectly elongated the propagation process and improved the final conversion PEGDA 700. In contrast, with a longer chain length, the resultant larger mesh size of polyPEGDA 700 occupied more aqueous solution of IDGCM, hence producing a softer hydrogel determined by loss factors of 0.063 which is physically indicative of damping of polymers,⁸⁰ compared to the loss factor (0.015) of polyPEGDA 575 (Figure S5.6).

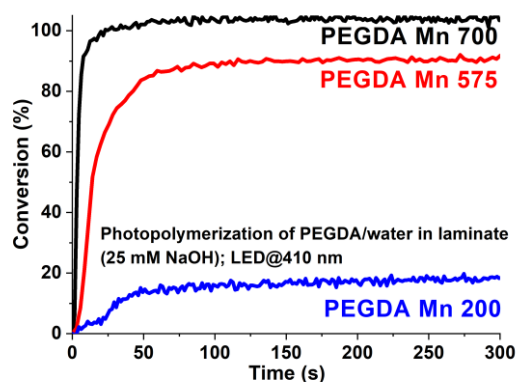


Figure 5.4. Photopolymerization profiles (double bond conversions vs time) of diverse PEGDA/water (80%/20%, wt) in laminate in the presence of IDGCM/Iod (0.5%/2%, wt) upon exposure to the LED@410 nm (110 mW cm^{-2}). (NaOH: 25 mM)

IDGCM demonstrated profound green light absorption at 530 nm (Figure 5.1 and Table 5.1). In this regard, the photorheology measurements were carried out to assess the photoinitiation ability of IDGCM to the PEGDA 700/water (80%/20%, wt) blend under green light (LED@530 nm). According to the gelation times, despite the identical extinction coefficients of IDGCM in alkaline medium at 410 nm and 530 nm (Table 5.1: $2500 \text{ M}^{-1} \text{ cm}^{-1}$), the gelation times (t_{gel}),

estimated by the crossovers of G' and G'' , under 530 nm illumination ($t_{gel530}(0.3 \text{ mm}) = 176 \text{ s}$) was over that under 410 nm illumination ($t_{gel410}(0.3 \text{ mm}) = 0.9 \text{ s}$) (Table 5.2), correlated to the photobleaching rate (Figure S5.1b and Figure S5.2b). Specifically, despite the light attenuation due to suspension of undissolved IDGCM (Figure S5.7a: $t = 0 \text{ s}$) and the increasing light scattering over polymerization independent of wavelength,⁸¹ the obstacles were significantly overcome through the photobleaching behavior of IDGCM (Figure S5.7a). The tremendously rapid photobleaching behavior took place under the irradiation of LED@410 nm, allowing further light penetration into the resin and accelerated overall polymerization of the PEGDA 700/water (80%/20%, wt) blend (Table 5.2). Contrary to LED@410 nm, the LED@530 nm induced a longer gelation time as the result of the slower photobleaching of IDGCM (Figure S5.2b) and the resultant light attenuation through samples (Table 5.2). Meanwhile the 1.0-mm thick sample further impeded the light penetration of LED@530 nm and compromised the photopolymerization of PEGDA 700 ($t_{gel} = 267 \text{ s}$). In comparison with the gelation time of the PEGDA 700/water (80%/20%, wt) blend upon exposure to LED@530 nm, that under the irradiation of LED@410 nm was scarcely dependent on the thickness in the range of 0.3 mm – 1.0 mm ($0.9 \text{ s} < t_{gel} < 2.2 \text{ s}$) (Table 5.2) attributed its rapid photobleaching behavior and photochemical process (Figure S5.1b and Figure S5.6a).

Table 5.2. Gel points of the photopolymerization of the blend of PEGDA 700/water (80%/20%, wt) at diverse thicknesses in the presence of IDGCM/Iod (0.5%/2%, wt) upon the exposure of LED@410 nm (110 mW cm^{-2}) and LED@530 nm (25 mW cm^{-2}). (25 mM NaOH)

LED	Thickness	0.3 mm	0.5 mm	1.0 mm
410 nm		$0.9 \pm 0.7 \text{ s}$	$1.6 \pm 0.1 \text{ s}$	$2.2 \pm 0.3 \text{ s}$
530 nm		$176 \pm 32 \text{ s}$	$194 \pm 1 \text{ s}$	$267 \pm 88 \text{ s}$

To explicitly determine the effect of electrolytes, different electrolytes with identical concentrations were used to offset the ionic strength effect. The gelation times of the PEGDA 700/water (80%/20%, wt) blend in the presence of 25 mM electrolyte (i.e., NaOH or NaCl) under LED@410 nm were complementary indicators to the aforementioned effect of salt on photolysis (Figure S5.1). In accordance with the discussed steady-state photolysis above, the gelation time of the PEGDA 700/water (80%/20%, wt) blend in NaOH media took place conspicuously rapid in the initial irradiation at 0.3 mm – 1.0 mm with the t_{gel} as low as 0.9 - 2.2 s (Table 5.3). The implementation of NaCl instead of NaOH impeded the gelation time of thick sample (0.5 mm: $t_{gel} = 71 \text{ s}$ and 1.0 mm: $t_{gel} = 132 \text{ s}$) 2 orders of magnitude longer than that with NaOH (Table 5.3) due to cage-escape reactions^{82, 83} Specifically, the in-cage back electron transfer between IDGCM and Iod significantly reduced the generation of phenyl radicals. However, the \cdot^- provide spacious pathways for caged Iod considering its larger ion

size compared to Cl⁻ (Scheme S5.2).^{73, 74} Meanwhile, the OH⁻ induced charged IDGCM, and the charged repulsion between IDGCM and Iod can enhance cage escape yields.⁸⁴ Consequently, the IDGCM in an alkaline medium presented better photoinitiation ability in terms of rate of polymerization, which was in line with the aforementioned results of steady-state photolysis (Figures S1b and S1c). In contrast, the thin thickness of 0.3 mm induced a gelation time of 17 s which was shorter than the thick samples (Table 5.3 and Figure S5.8). Even though the intensity of blue light scarcely impedes the conversion of the PEGDA 700/water (80%/20%, wt) blend in NaOH media (Figure S5.5), it predominantly manipulated the resin in NaCl media, determined by the significantly decelerated polymerization and the reduced conversion under LED@400 nm (6.4 mW cm⁻²) (Figure S5.9).

Table 5.3. Gel points of the photopolymerization of the blend of PEGDA 700/water (80%/20%, wt) with 25 mM NaCl or 25 mM NaOH at diverse thicknesses in the presence of IDGCM/Iod (0.5%/2%, wt) upon the exposure of LED@410 nm (110 mW cm⁻²).

Electrolyte	Thickness	0.3 mm	0.5 mm	1.0 mm
NaCl		17 ± 2 s	71 ± 11 s	132 ± 19 s
NaOH		0.9 ± 0.7 s	1.6 ± 0.1 s	2.2 ± 0.3 s

5.7.4 3D Printing

The excellent photoinitiation ability of IDGCM in NaOH media under blue light with limited intensity endowed the developed formulation (Table S5.1) with the high ability for 3D printing. As aforementioned impairment of conversion of the PEGDA 700/water (80%/20%, wt) blend due to excess IDGCM (Figure S5.5a-b), the undissolved IDGCM can otherwise play a role as a photo absorber due to its inherent blue appearance ensuring the favorable shape-fidelity over 3D printing.⁸⁵ To explicitly determine the layered exposure time and the layer thickness for rapid and high-fidelity 3D printing, a set of 3D printing was carried out in designed settings (Table S5.2). The thickness beyond the light penetration boundary and insufficient exposure time caused unevenly cured objects, while 4 seconds exposure/layer was appreciably adequate for edge sharpness on the basis of the layer thickness of 0.020 mm (Table S5.2). With the developed formulation and the optimum setting, a topography print with superior fidelity was successfully produced in 3.28 h using the 3D printer (Figure 5.5). As emphasized in the picture, a letter “N” (1 mm × 0.3 mm × 1 mm, L × W × H) on the tower was remarkably visualized with a sharp edge, exhibiting the excellent spatial resolution of the 3D printed topography.

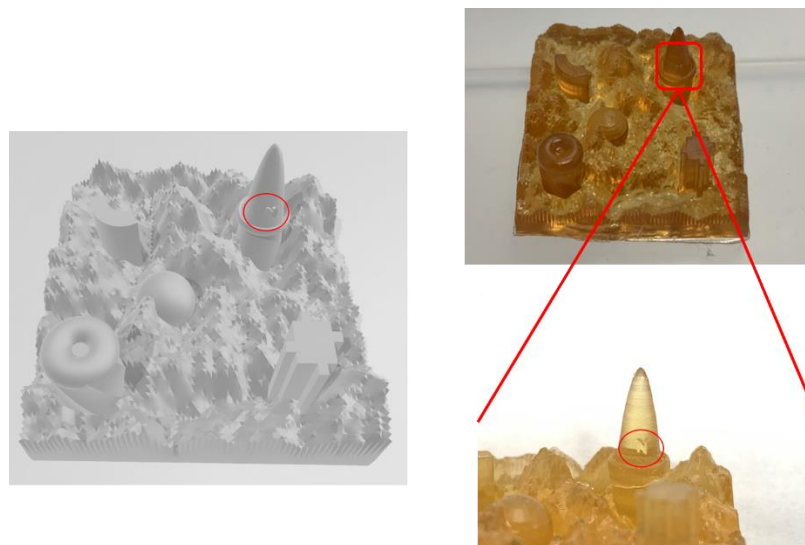


Figure 5.5. The top view of STL model file and the topography print cured using the PEGDA 700/water (80%/20%, wt) in the presence of IDGCM/Iod (0.5%/2%, wt) and 25 mM NaOH. (30 × 30 × 15 mm, L × W × H)

Interestingly, a shape memory behavior reversibly switched between 2D and 3D was disclosed.⁸⁶ A seashell was printed on the basis of the designed model (Figure 5.6a). Specifically, the a_1 and the a_2 were overlaid layer by layer, forming an 80-layer model a_3 . The layer thickness of 0.010 mm was applied to the seashell model intended for the overcuring to the preceding layer (a_1). To achieve the 2D-3D conversion, the curvature of the planar seashell should be induced by the change of water content.⁸⁶ Considering the excellent conversion of PEGDA 700 under the irradiation of LED@400 nm, the swelling induced enlarged dimensions can cause the fracture at high gel content,⁸⁷ therefore, we reduced the water content instead as the strategy to fabricate the curvature structure. As the abovementioned concern of fracture, the reversed 2D-3D conversion should also avoid overwhelming swelling. With the knowledge of ionic strength-driven hydrophobic intramolecular interactions,⁸⁸ the NaCl molecules swelled into the printed seashell without intensely changing the dimensions can efficiently avoid fracture due to overwhelming swelling. Therefore, the inherent water content in the printed planar seashell from the formulation was exchanged with 2% aqueous NaCl solution driven by osmotic pressure (Figure 5.6b).⁸⁹ Eventually, the uneven crosslinking density induced correlated asymmetrical swelling ratio⁹⁰ endowed the seashell with uneven curvature level by loss of water content under air (Figure 5.6b), and the reversible 3D-2D conversion was successfully achieved via re-swelling in 2% aqueous NaCl solution.

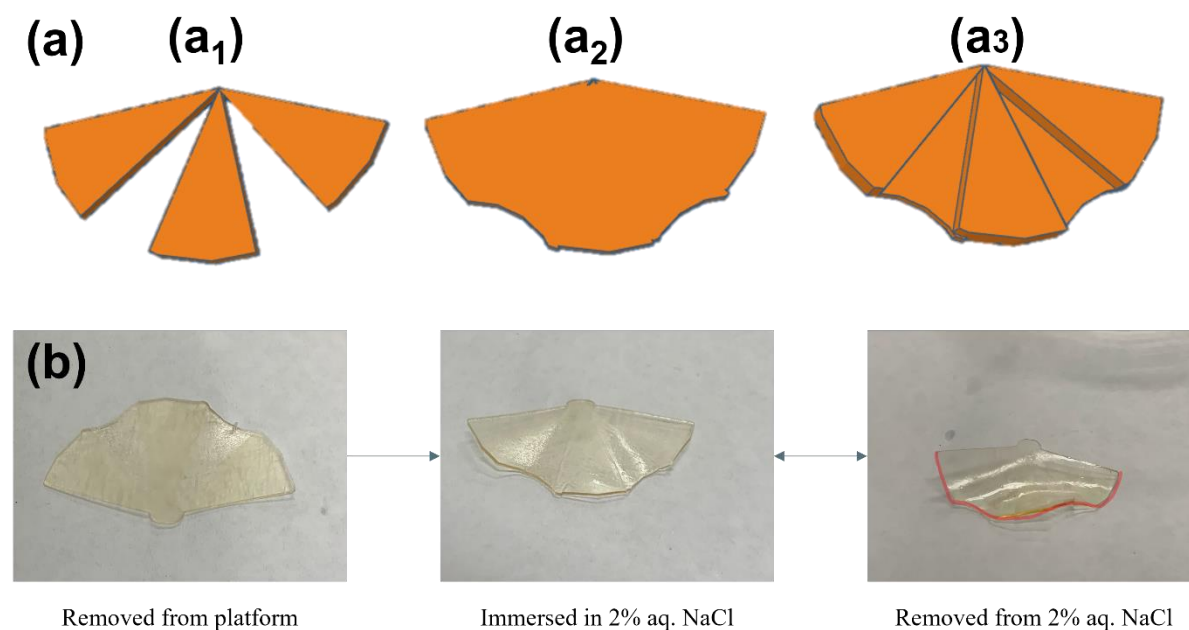


Figure 5.6. (a) The design of the seashell and (b) the transition of the seashell print cured using the PEGDA 700/water (80%/20%, wt) in the presence of IDGCM/Iod (0.5%/2%, wt) and 25 mM NaOH. ($38 \times 20 \times 0.6$ mm, L \times W \times H)

5.8 Conclusion and outlook

We have demonstrated that the photoinitiation ability of IDGCM can be mediated by either the concentration of each component in formulations, chain length of PEGDA, or different LEDs (i.e., emission wavelength and intensity). The underlying effect of the concentration of the investigated components was on the basis of the solubility of IDGCM except under some extreme conditions. With the increased solubility of IDGCM in the formulations, the photopolymerization efficiency of PEGDA was enhanced in terms of rate of photopolymerization under the irradiation of LED@410 nm. Besides, the PEGDA with a longer chain can improve the photopolymerization of PEGDA in terms of final C=C double bond. Interestingly, the IDGCM-based photoinitiating system also behaved efficiently under green LED and blue LED with low intensity (6.4 mW cm^{-2}). With the guidance of the studies of the resin composition and relative concentration, IDGCM/Iod (0.5%/2%, wt) in the presence of 25 mM NaOH was used in the 3D printing of PEGDA 700/DI water (80%/20%, wt). The dual role of IDGCM acting as both the photoinitiator and the light absorber can lead to rapid and high-fidelity 3D printing and allow for the fabrication of sophisticated objects. Moreover, a printed planar seashell with stimuli-responsive function via swelling and evaporation using the developed formulation allowed reversibly switching.

5.9 References

- (1) Villaño, D.; García-Viguera, C.; Mena, P. Colors: Health Effects. In *Encyclopedia of Food and Health*, Caballero, B., Finglas, P. M., Toldrá, F. Eds.; Elsevier B.V., 2016; pp 265-272.
- (2) Scientific Opinion on the re-evaluation of Indigo Carmine (E 132) as a food additive. *EFSA J.* **2014**, *12* (7), 3768.
- (3) Zhu, D.; Peng, X.; Xiao, P. Indigo Carmine: A Base and Neutral Electrolyte-mediated Photoinitiator for 3D Printing in High Fidelity. *Addit. Manuf.* **2022**, *59*, 103154.
- (4) Ligon, S. C.; Liska, R.; Stampfl, J.; Gurr, M.; Mulhaupt, R. Polymers for 3D Printing and Customized Additive Manufacturing. *Chem. Rev.* **2017**, *117* (15), 10212-10290.
- (5) Chua, C. K.; Leong, K. F. *3D Printing and Additive Manufacturing*; World Scientific, 2017.
- (6) Yu, C.; Schimelman, J.; Wang, P.; Miller, K. L.; Ma, X.; You, S.; Guan, J.; Sun, B.; Zhu, W.; Chen, S. Photopolymerizable Biomaterials and Light-Based 3D Printing Strategies for Biomedical Applications. *Chem. Rev.* **2020**, *120* (19), 10695-10743.
- (7) Chen, G.; Xu, Y.; Chi Lip Kwok, P.; Kang, L. Pharmaceutical Applications of 3D Printing. *Addit. Manuf.* **2020**, *34*, 101209.
- (8) Browne, M. P.; Redondo, E.; Pumera, M. 3D Printing for Electrochemical Energy Applications. *Chem. Rev.* **2020**, *120* (5), 2783-2810.
- (9) Lee, C.-Y.; Taylor, A. C.; Nattestad, A.; Beirne, S.; Wallace, G. G. 3D Printing for Electrocatalytic Applications. *Joule* **2019**, *3* (8), 1835-1849.
- (10) Economidou, S. N.; Lamprou, D. A.; Douroumis, D. 3D printing applications for transdermal drug delivery. *Int. J. Pharm.* **2018**, *544* (2), 415-424.
- (11) Pekkanen, A. M.; Mondschein, R. J.; Williams, C. B.; Long, T. E. 3D Printing Polymers with Supramolecular Functionality for Biological Applications. *Biomacromolecules* **2017**, *18* (9), 2669-2687.
- (12) Liaw, C. Y.; Guvendiren, M. Current and emerging applications of 3D printing in medicine. *Biofabrication* **2017**, *9* (2), 024102.
- (13) Giannopoulos, A. A.; Mitsouras, D.; Yoo, S. J.; Liu, P. P.; Chatzizisis, Y. S.; Rybicki, F. J. Applications of 3D printing in cardiovascular diseases. *Nat. Rev. Cardiol.* **2016**, *13* (12), 701-718.
- (14) Do, A. V.; Khorsand, B.; Geary, S. M.; Salem, A. K. 3D Printing of Scaffolds for Tissue Regeneration Applications. *Adv. Healthcare Mater.* **2015**, *4* (12), 1742-1762.
- (15) Bao, Y.; Paunović, N.; Leroux, J. C. Challenges and Opportunities in 3D Printing of Biodegradable Medical Devices by Emerging Photopolymerization Techniques. *Adv. Funct. Mater.* **2022**, *32* (15), 2109864.
- (16) Zhu, D.; Zhang, J.; Lalevée, J.; Xiao, P. Chapter 1 Novel Photoinitiating Systems for 3D Printing. In *3D Printing with Light*, Xiao, P., Zhang, J. Eds.; De Gruyter, 2021; pp 1-48.
- (17) Xu, X.; Awad, A.; Robles-Martinez, P.; Gaisford, S.; Goyanes, A.; Basit, A. W. Vat Photopolymerization 3D Printing for Advanced Drug Delivery and Medical Device Applications. *J. Controlled Release* **2021**, *329*, 743-757.
- (18) Kim, S. H.; Hong, H.; Ajiteru, O.; Sultan, M. T.; Lee, Y. J.; Lee, J. S.; Lee, O. J.; Lee, H.; Park, H. S.; Choi, K. Y.; et al. 3D bioprinted silk fibroin hydrogels for tissue engineering. *Nat. Protoc.* **2021**, *16* (12), 5484-5532.
- (19) Lee, M.; Rizzo, R.; Surman, F.; Zenobi-Wong, M. Guiding Lights: Tissue Bioprinting Using Photoactivated Materials. *Chem. Rev.* **2020**, *120* (19), 10950-11027.
- (20) Zhou, Y.; Ma, G.; Shi, S.; Yang, D.; Nie, J. Photopolymerized water-soluble chitosan-based hydrogel as potential use in tissue engineering. *Int. J. Biol. Macromol.* **2011**, *48* (3), 408-413.
- (21) Klymenko, A.; Nicolai, T.; Chassenieux, C.; Colombani, O.; Nicol, E. Formation of porous hydrogels by self-assembly of photo-cross-linkable triblock copolymers in the presence of homopolymers. *Polymer* **2016**, *106*, 152-158.

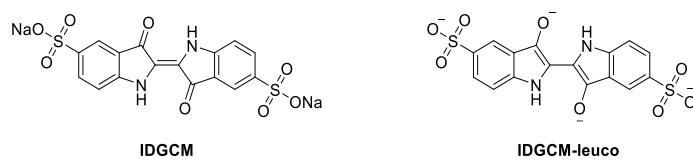
- (22) Pawar, A. A.; Saada, G.; Cooperstein, I.; Larush, L.; Jackman, J. A.; Tabaei, S. R.; Cho, N.-J.; Magdassi, S. High-performance 3D printing of hydrogels by water-dispersible photoinitiator nanoparticles. *Sci. Adv.* **2016**, *2* (4), e1501381.
- (23) Alupei, I. C.; Alupei, V.; Ritter, H. Cyclodextrins in Polymer Synthesis: Photoinitiated Free-Radical Polymerization of N-Isopropylacrylamide in Water Initiated by a Methylated β -Cyclodextrin/2-Hydroxy-2-methyl-1-phenylpropan-1-one Host/Guest Complex. *Macromol. Rapid Commun.* **2002**, *23* (1), 55-58.
- (24) Zhang, J.; Dumur, F.; Xiao, P.; Graff, B.; Bardelang, D.; Gignes, D.; Fouassier, J. P.; Lalevée, J. Structure Design of Naphthalimide Derivatives: Toward Versatile Photoinitiators for Near-UV/Visible LEDs, 3D Printing, and Water-Soluble Photoinitiating Systems. *Macromolecules* **2015**, *48* (7), 2054-2063.
- (25) Wang, J.; Stanic, S.; Altun, A. A.; Schwentenwein, M.; Dietliker, K.; Jin, L.; Stampfl, J.; Baudis, S.; Liska, R.; Grutzmacher, H. A highly efficient waterborne photoinitiator for visible-light-induced three-dimensional printing of hydrogels. *Chem. Commun.* **2018**, *54* (8), 920-923.
- (26) Wang, J.; Chiappone, A.; Roppolo, I.; Shao, F.; Fantino, E.; Lorusso, M.; Rentsch, D.; Dietliker, K.; Pirri, C. F.; Grutzmacher, H. All-in-One Cellulose Nanocrystals for 3D Printing of Nanocomposite Hydrogels. *Angew. Chem., Int. Ed.* **2018**, *57* (9), 2353-2356.
- (27) Nicol, E. Photopolymerized Porous Hydrogels. *Biomacromolecules* **2021**, *22* (4), 1325-1345.
- (28) Liu, Y.; Huang, X.; Han, K.; Dai, Y.; Zhang, X.; Zhao, Y. High-Performance Lignin-Based Water-Soluble Macromolecular Photoinitiator for the Fabrication of Hybrid Hydrogel. *ACS Sustainable Chem. Eng.* **2019**, *7* (4), 4004-4011.
- (29) Le, C. M. Q.; Petitoy, T.; Wu, X.; Spangenberg, A.; Ortyl, J.; Galek, M.; Infante, L.; Thérien - Aubin, H.; Chemtob, A. Water - Soluble Photoinitiators from Dimethylamino - Substituted Monoacylphosphine Oxide for Hydrogel and Latex Preparation. *Macromol. Chem. Phys.* **2021**, *222* (19).
- (30) Nishigori, C. UV-induced DNA damage in carcinogenesis and its repair. *J. Dermatol. Sci.* **2000**, *23* (1), S41-S44.
- (31) Ichihashi, M.; Ueda, M.; Budiyanto, A.; Bito, T.; Oka, M.; Fukunaga, M.; Tsuru, K.; Horikawa, T. UV-induced skin damage. *Toxicology* **2003**, *189* (1-2), 21-39.
- (32) Grujil, F. R.; Kranen, H. J.; Mullenders, L. H. F. UV-induced DNA damage, repair, mutations and oncogenic pathways in skin cancer. *J. Photochem. Photobiol., B* **2001**, *63* (1-3), 19-27.
- (33) Brash, D. E. UV signature mutations. *Photochem. Photobiol.* **2015**, *91* (1), 15-26.
- (34) Shao, J.; Huang, Y.; Fan, Q. Visible light initiating systems for photopolymerization: status, development and challenges. *Polym. Chem.* **2014**, *5* (14), 4195-4210.
- (35) Kojima, K.; Ito, M.; Morishita, H.; Hayashi, N. A Novel Water-Soluble Photoinitiator for the Acrylic Photopolymerization Type Resist System. *Chem. Mater.* **1998**, *10* (11), 3429-3433.
- (36) Thompson, S. P. *Light Visible and Invisible: A Series of Lectures Delivered at the Royal Institution of Great Britain, at Christmas, 1896*; Macmillan, 1897.
- (37) Bisi, O. *Visible and Invisible: The Wonders of Light Phenomena*; Springer Cham, 2015.
- (38) Batchelor, R. R.; Kwandou, G.; Spicer, P. T.; Stenzel, M. H. (-)-Riboflavin (vitamin B2) and flavin mononucleotide as visible light photo initiators in the thiol-ene polymerisation of PEG-based hydrogels. *Polym. Chem.* **2017**, *8* (6), 980-984.
- (39) Applegate, M. B.; Partlow, B. P.; Coburn, J.; Marelli, B.; Pirie, C.; Pineda, R.; Kaplan, D. L.; Omenetto, F. G. Photocrosslinking of Silk Fibroin Using Riboflavin for Ocular Prostheses. *Adv. Mater.* **2016**, *28* (12), 2417-2420.
- (40) Kim, S.-h.; Chu, C.-C. Visible light induced dextran-methacrylate hydrogel formation using (-)-riboflavin vitamin B2 as a photoinitiator and L-arginine as a co-initiator. *Fibers Polym.* **2009**, *10* (1), 14-20.
- (41) Shih, H.; Lin, C. C. Visible-light-mediated thiol-ene hydrogelation using eosin-Y as the only photoinitiator. *Macromol. Rapid Commun.* **2013**, *34* (3), 269-273.

- (42) Shin, J. Y.; Yeo, Y. H.; Jeong, J. E.; Park, S. A.; Park, W. H. Dual-crosslinked methylcellulose hydrogels for 3D bioprinting applications. *Carbohydr. Polym.* **2020**, *238*, 116192.
- (43) Lee, H.; Shin, D.; Shin, S.; Hyun, J. Effect of gelatin on dimensional stability of silk fibroin hydrogel structures fabricated by digital light processing 3D printing. *J. Ind. Eng. Chem.* **2020**, *89*, 119-127.
- (44) Karakurt, I.; Aydogdu, A.; Cikrikci, S.; Orozco, J.; Lin, L. Stereolithography (SLA) 3D printing of ascorbic acid loaded hydrogels: A controlled release study. *Int. J. Pharm.* **2020**, *584*, 119428.
- (45) Bagheri, A.; Bainbridge, C. W. A.; Engel, K. E.; Qiao, G. G.; Xu, J.; Boyer, C.; Jin, J. Oxygen Tolerant PET-RAFT Facilitated 3D Printing of Polymeric Materials under Visible LEDs. *ACS Appl. Polym. Mater.* **2020**, *2* (2), 782-790.
- (46) Ndefru, B. G.; Ringstrand, B. S.; Diouf, S. I. Y.; Seifert, S.; Leal, J. H.; Semelsberger, T. A.; Dreier, T. A.; Firestone, M. A. Multiscale additive manufacturing of polymers using 3D photo-printable self-assembling ionic liquid monomers. *Mol. Syst. Des. Eng.* **2019**, *4* (3), 580-585.
- (47) Wang, Z.; Kumar, H.; Tian, Z.; Jin, X.; Holzman, J. F.; Menard, F.; Kim, K. Visible Light Photoinitiation of Cell-Adhesive Gelatin Methacryloyl Hydrogels for Stereolithography 3D Bioprinting. *ACS Appl. Mater. Interfaces* **2018**, *10* (32), 26859-26869.
- (48) Acosta-Velez, G. F.; Zhu, T. Z.; Linsley, C. S.; Wu, B. M. Photocurable poly(ethylene glycol) as a bioink for the inkjet 3D pharming of hydrophobic drugs. *Int. J. Pharm.* **2018**, *546* (1-2), 145-153.
- (49) Joung, D.; Lavoie, N. S.; Guo, S. Z.; Park, S. H.; Parr, A. M.; McAlpine, M. C. 3D Printed Neural Regeneration Devices. *Adv. Funct. Mater.* **2020**, *30* (1), 1906237.
- (50) Merinas-Amo, R.; Martinez-Jurado, M.; Jurado-Gueto, S.; Alonso-Moraga, A.; Merinas-Amo, T. Biological Effects of Food Coloring in In Vivo and In Vitro Model Systems. *Foods* **2019**, *8* (5), 176.
- (51) König, J. Food colour additives of synthetic origin. In *Colour Additives for Foods and Beverages*, Elsevier Ltd., 2015; pp 35-60.
- (52) Borzelleca, J. F.; Hogan, G. K. Chronic toxicity/carcinogenicity study of FD & C Blue No. 2 in mice. *Food Chem. Toxicol.* **1985**, *23* (8), 719-722.
- (53) Scientific Opinion on the safety and efficacy of indigo carmine (E 132) for cats and dogs and ornamental fish. *EFSA J.* **2015**, *13* (5).
- (54) Roberts, E. L.; Burguieres, S.; Warner, I. M. Spectroscopic Studies of Indigo Carmine Dye in Organized Media. *Appl. Spectrosc.* **1998**, *52* (10), 1305-1313.
- (55) Hua, C.-j.; Zhang, K.; Xin, M.; Ying, T.; Gao, J.-r.; Jia, J.-h.; Li, Y.-j. High quantum yield and pH sensitive fluorescence dyes based on coumarin derivatives: fluorescence characteristics and theoretical study. *RSC Adv.* **2016**, *6* (54), 49221-49227.
- (56) Qin, Y.; Qin, J.; Zhou, X.; Yang, Y.; Chen, R.; Tan, J.; Xiao, K.; Wang, X. Effects of pH on light absorption properties of water-soluble organic compounds in particulate matter emitted from typical emission sources. *J. Hazard. Mater.* **2022**, *424* (Pt C), 127688.
- (57) Voicescu, M.; Ionescu, S.; Gatea, F. Effect of pH on the fluorescence characteristics of some flavones probes. *Spectrochim. Acta, Part A* **2014**, *123*, 303-308.
- (58) Pace, M. L.; Reche, I.; Cole, J. J.; Fernández-Barbero, A.; Mazuecos, I. P.; Prairie, Y. T. pH change induces shifts in the size and light absorption of dissolved organic matter. *Biogeochemistry* **2011**, *108* (1-3), 109-118.
- (59) Wolfbeis, O. S.; Knierzinger, A.; Schipfer, R. pH-dependent fluorescence spectroscopy XVII: First excited singlet state dissociation constants, photoautomerism and dual fluorescence of flavonol. *J. Photochem.* **1983**, *21* (1), 67-79.
- (60) Schulman, S. G.; Capomacchia, A. C. Variations of fluorescence quantum yields with pH or Hammett acidity. Near equilibrium vs nonequilibrium excited state proton exchange. *J. Phys. Chem.* **1975**, *79* (14), 1337-1343.

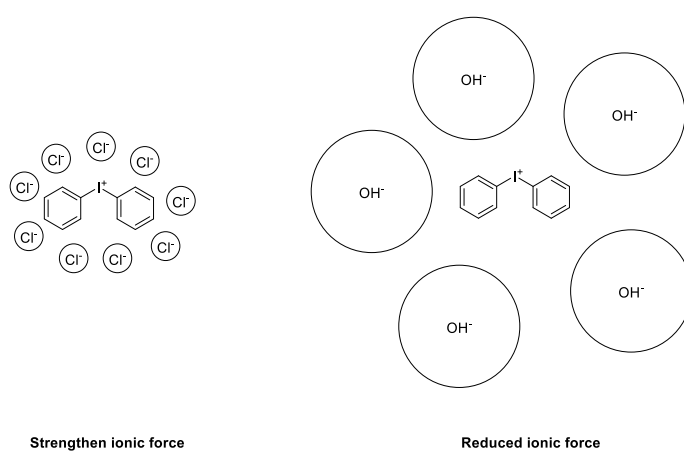
- (61) Teshima, K.; Uemura, S.; Kobayashi, N.; Hirohashi, R. Effect of pH on Photopolymerization Reaction of Aniline Derivatives with the Tris(2,2'-bipyridyl)ruthenium Complex and the Methylviologen System. *Macromolecules* **1998**, *31* (20), 6783-6788.
- (62) Fantino, E.; Chiappone, A.; Roppolo, I.; Manfredi, D.; Bongiovanni, R.; Pirri, C. F.; Calignano, F. 3D Printing of Conductive Complex Structures with In Situ Generation of Silver Nanoparticles. *Adv. Mater.* **2016**, *28* (19), 3712-3717.
- (63) Lim, K. S.; Galarraga, J. H.; Cui, X.; Lindberg, G. C. J.; Burdick, J. A.; Woodfield, T. B. F. Fundamentals and Applications of Photo-Cross-Linking in Bioprinting. *Chem. Rev.* **2020**, *120* (19), 10662-10694.
- (64) Witte, R. P.; Blake, A. J.; Palmer, C.; Kao, W. J. Analysis of poly(ethylene glycol)-diacrylate macromer polymerization within a multicomponent semi-interpenetrating polymer network system. *J. Biomed. Mater. Res., Part A* **2004**, *71* (3), 508-518.
- (65) Silverstein, R. M.; Webster, F. X.; Kiemle, D. J.; Bryce, D. L. *Spectrometric Identification of Organic Compounds*; Wiley, 2014.
- (66) Seixas de Melo, J.; Rondao, R.; Burrows, H. D.; Melo, M. J.; Navaratnam, S.; Edge, R.; Voss, G. Photophysics of an indigo derivative (keto and leuco structures) with singular properties. *J. Phys. Chem. A* **2006**, *110* (51), 13653-13661.
- (67) Seixas de Melo, J.; Moura, A. P.; Melo, M. J. Photophysical and Spectroscopic Studies of Indigo Derivatives in Their Keto and Leuco Forms. *J. Phys. Chem. A* **2004**, *108* (34), 6975-6981.
- (68) Rondao, R.; Seixas de Melo, J.; Melo, M. J.; Parola, A. J. Excited-state isomerization of leuco indigo. *J. Phys. Chem. A* **2012**, *116* (11), 2826-2832.
- (69) Mihas, O.; Kalogerakis, N.; Psillakis, E. Photolysis of 2,4-dinitrotoluene in various water solutions: effect of dissolved species. *J. Hazard. Mater.* **2007**, *146* (3), 535-539.
- (70) Izumrudov, V. A.; Savitskii, A. P.; Bakeev, K. N.; Zezin, A. B.; Kabanov, V. A. A fluorescence quenching study of interpolyelectrolyte reactions. *Macromol. Rapid Commun.* **1984**, *5* (11), 709-714.
- (71) Kurian, A.; George, S. D.; Bindhu, C. V.; Nampoore, V. P.; Vallabhan, C. P. Thermal lens technique to study the effect of pH on electronic energy transfer in organic dye mixtures. *Spectrochim. Acta, Part A* **2007**, *67* (3-4), 678-682.
- (72) Ahmad, I.; Anwar, Z.; Ali, S. A.; Hasan, K. A.; Sheraz, M. A.; Ahmed, S. Ionic strength effects on the photodegradation reactions of riboflavin in aqueous solution. *J. Photochem. Photobiol., B* **2016**, *157*, 113-119.
- (73) Ohtsuka, T.; Yamamoto, Y.; Hayashi, K. Salt effect on photoinduced cationic polymerization of isobutyl vinyl ether by butyl iodide. *J. Polym. Sci., Part C: Polym. Lett.* **1989**, *27* (10), 399-402.
- (74) Gieselmann, M. J.; Anderson, M. A. Effect of Ionic Strength on Boehmite Hydrogel Formation. *J. Am. Ceram. Soc.* **1989**, *72* (6), 980-985.
- (75) Janzen, E. G. Electron spin resonance study of the hyperfine splitting constants of naturally abundant carbon-13 and nitrogen-15 in diphenylmethyl tert-butyl aminoxyl (nitroxide). Solvent and temperature effects. *Can. J. Chem.* **1984**, *62* (8), 1653-1657.
- (76) Butler, J. N. *Ionic Equilibrium: Solubility and pH Calculations*; Wiley, 1998.
- (77) Petrucci, R. H.; Herring, F. G.; Madura, J. D.; Bissonette, C. *General Chemistry: Principles and Modern Applications*; Pearson Education, 2017.
- (78) Scholz, F.; Kahlert, H. *Chemical Equilibria in Analytical Chemistry: The Theory of Acid-Base, Complex, Precipitation and Redox Equilibria*; Springer Cham, 2019.
- (79) Barth, J.; Buback, M.; Russell, G. T.; Smolne, S. Chain-Length-Dependent Termination in Radical Polymerization of Acrylates. *Macromol. Chem. Phys.* **2011**, *212* (13), 1366-1378.
- (80) Lee, I.-B.; Son, H.-H.; Um, C.-M. Rheologic properties of flowable, conventional hybrid, and condensable composite resins. *Dent. Mater.* **2003**, *19* (4), 298-307.
- (81) You, S.; Wang, P.; Schimelman, J.; Hwang, H. H.; Chen, S. High-fidelity 3D Printing using Flashing Photopolymerization. *Addit. Manuf.* **2019**, *30*, 100834.

-
- (82) Fouassier, J. P. *Photoinitiation, Photopolymerization, and Photocuring: Fundamentals and Applications*; Carl Hanser Verlag GmbH & Co, 1995.
- (83) Clark, C. D.; Hoffman, M. Z. Ion-Pairing Control of Excited-State Electron-Transfer Reactions. Quenching, Charge Recombination, and Back Electron Transfer. *J. Phys. Chem.* **1996**, *100* (18), 7526-7532.
- (84) Olmsted, J.; Meyer, T. J. Factors affecting cage escape yields following electron-transfer quenching. *J. Phys. Chem.* **1987**, *91* (6), 1649-1655.
- (85) Schwab, A.; Levato, R.; D'Este, M.; Piluso, S.; Eglin, D.; Malda, J. Printability and Shape Fidelity of Bioinks in 3D Bioprinting. *Chem. Rev.* **2020**, *120* (19), 11028-11055.
- (86) Nojoomi, A.; Jeon, J.; Yum, K. 2D material programming for 3D shaping. *Nat. Commun.* **2021**, *12* (1), 603.
- (87) Khan, F.; Kwek, D.; Kronfli, E.; Ahmad, S. R. Laser-Induced Crosslinking of Ultra-Low- and High-Density Polyethylene. *Macromol. Rapid Commun.* **2007**, *28* (2), 158-163.
- (88) Ozbas, B.; Kretsinger, J.; Rajagopal, K.; Schneider, J. P.; Pochan, D. J. Salt-Triggered Peptide Folding and Consequent Self-Assembly into Hydrogels with Tunable Modulus. *Macromolecules* **2004**, *37* (19), 7331-7337.
- (89) Kim, S. H.; Seo, Y. B.; Yeon, Y. K.; Lee, Y. J.; Park, H. S.; Sultan, M. T.; Lee, J. M.; Lee, J. S.; Lee, O. J.; Hong, H.; et al. 4D-bioprinted silk hydrogels for tissue engineering. *Biomaterials* **2020**, *260*, 120281.
- (90) Canal, T.; Peppas, N. A. Correlation between mesh size and equilibrium degree of swelling of polymeric networks. *J. Biomed. Mater. Res.* **1989**, *23* (10), 1183-1193.

5.10 Supporting Information



Scheme S5.1. The chemical structures of different forms of IDGCM.



Scheme S5.2. The schematic diagram for anion distribution surrounding Iod in formulation.

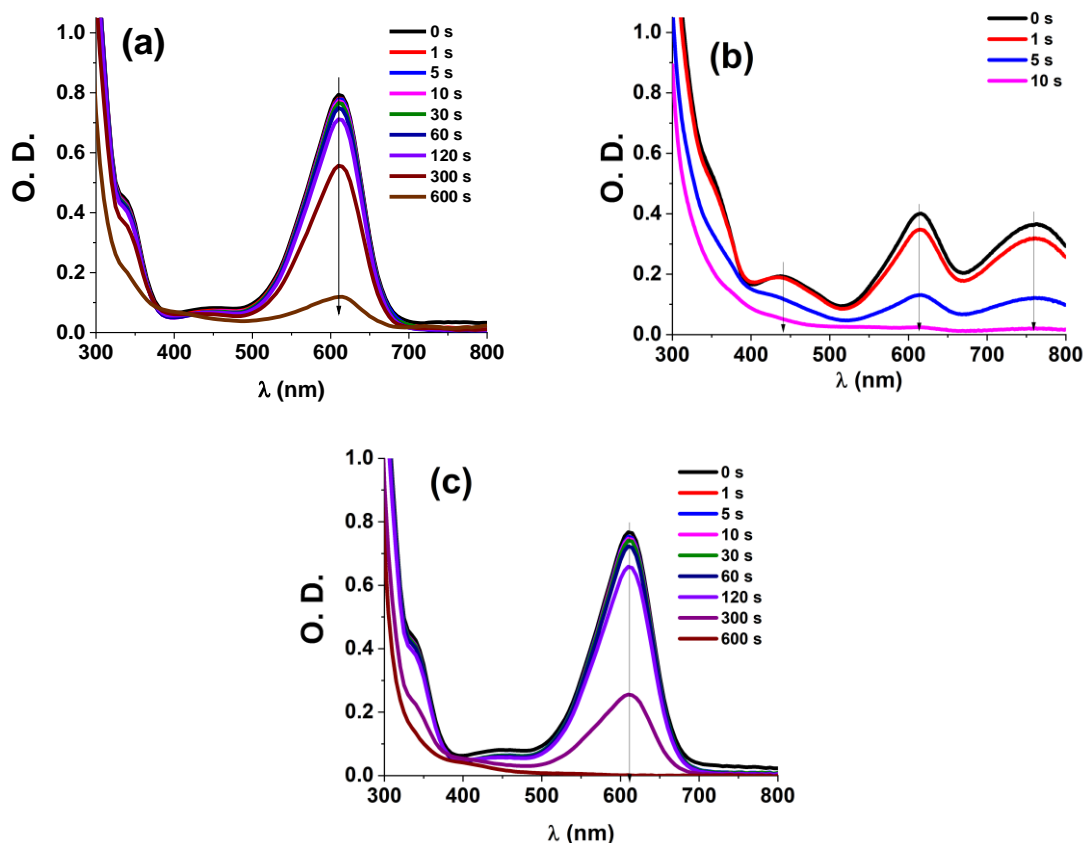


Figure S5.1. Steady-state photolysis of IDGCM/Iod in (a) water, (b) the presence of 25 mM aq. NaOH ($[\text{Iod}] = 3.86$ mM), and (c) the presence of 25 mM aq. NaCl upon exposure to LED@410 nm ($[\text{Iod}] = 3.86$ mM); UV-vis spectra recorded at different irradiation time.

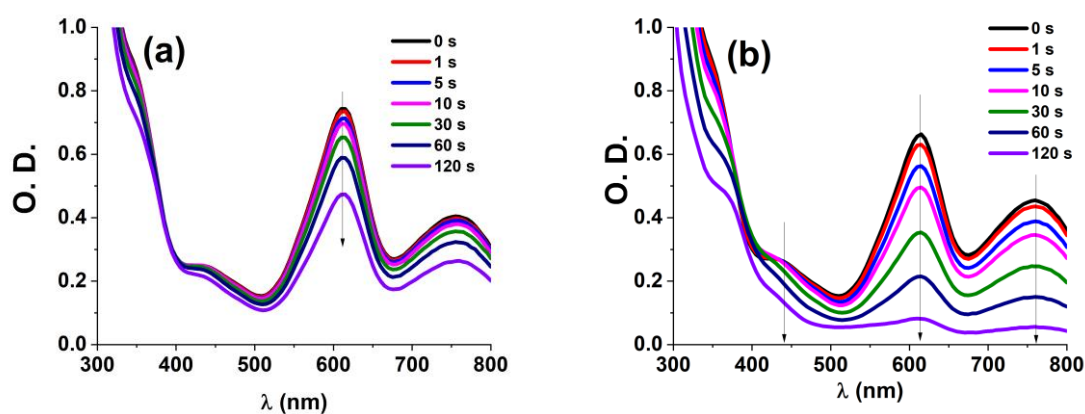


Figure S5.2. Steady-state photolysis of IDGCM/Iod in water in the presence of 25 mM aq. NaOH ($[\text{Iod}] = 3.86$ mM) upon exposure to (a) LED@400 nm (6.4 mW cm^{-2}) and (b) LED@530 nm (25 mW cm^{-2}); UV-vis spectra recorded at different irradiation time.

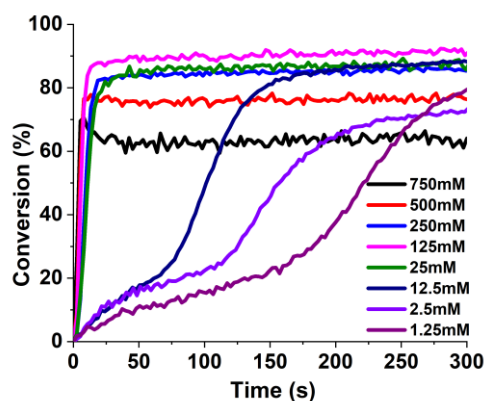


Figure S5.3. Photopolymerization profiles (double bond conversions vs time) of HEA/water (50%/50%, w/w) in laminate in the presence of IDGCM/Iod (0.5%/2%, wt) with 1.25 mM – 750 mM NaOH upon exposure to the LED@410 nm (110 mW cm^{-2}).

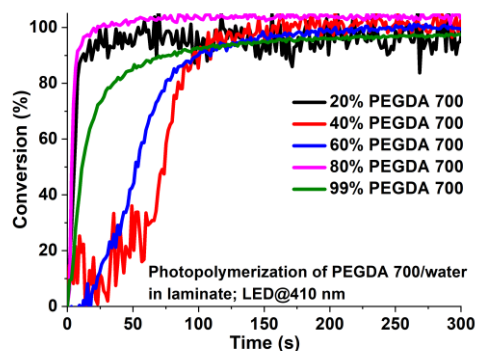
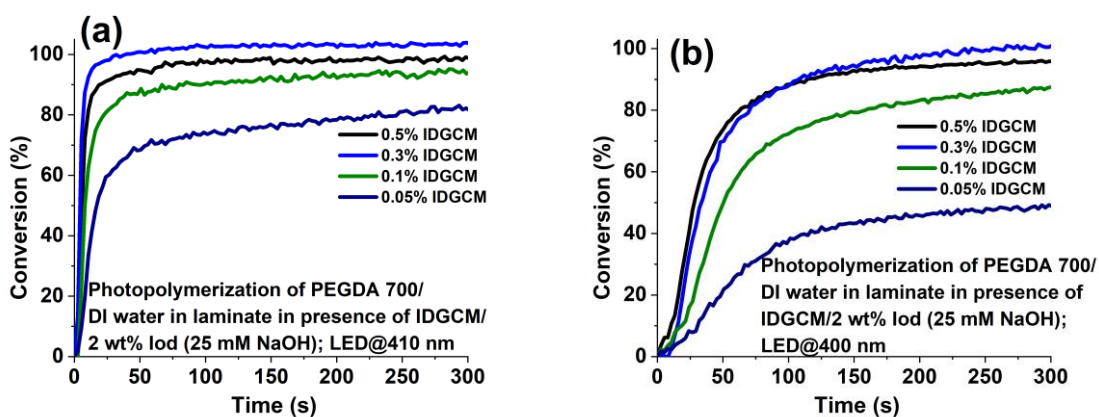


Figure S5.4. Photopolymerization profiles (double bond conversions vs time) of PEGDA 700/water in diverse ratios in laminate in the presence of IDGCM/Iod (0.5%/2%, wt) upon exposure to the LED@410 nm (110 mW cm^{-2}). (NaOH: 25 mM)



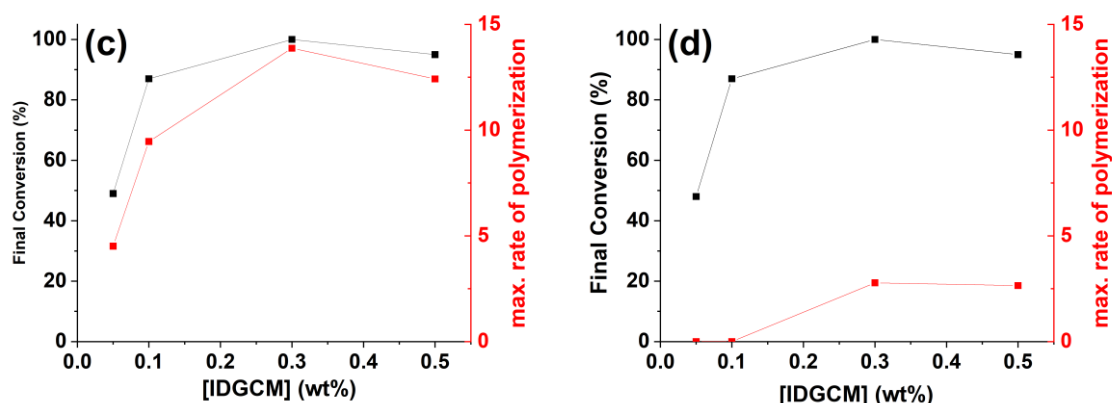


Figure S5.5. Photopolymerization profiles (double bond conversions vs time) of PEGDA 700/water (80%/20%, w/w) in laminate in the presence of IDGCM/Iod (0.05-0.5%/2%, wt) and 25 mM NaOH upon exposure to the (a) LED@410 nm (110 mW cm⁻²) and (b) LED@400 nm (6.4 mW cm⁻²); (c) and (d) final bond conversion of PEGDA 700/water blend and $R_{p,max}$ as a function of IDGCM weight percentage.

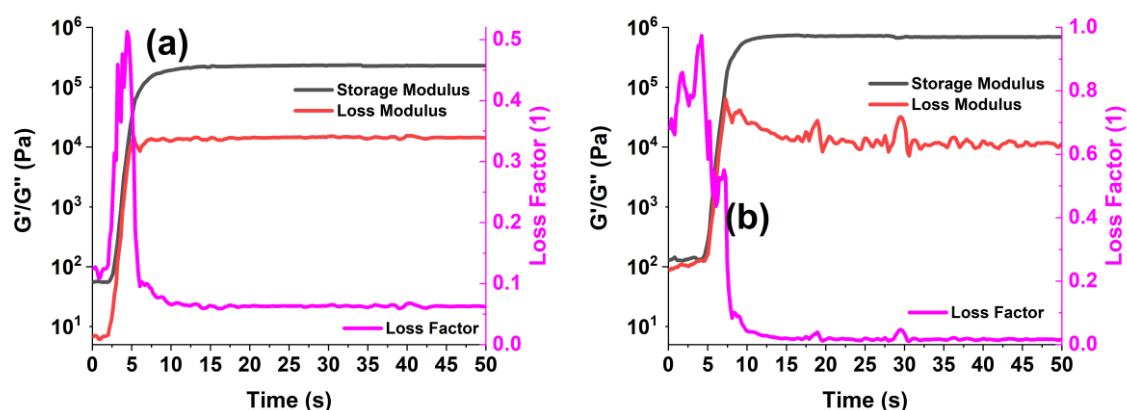


Figure S5.6. Photorheology profiles (storage moduli (G'), loss moduli (G'') and loss factors vs time) of photopolymerization of (a) PEGDA 700/water blend (80%/20%, wt) and (b) PEGDA 575/water blend (80%/20%, wt) in the presence of IDGCM/Iod (0.5%/2%, wt) upon exposure to LED@410 nm (110 mW cm⁻²). (25 mM NaOH)

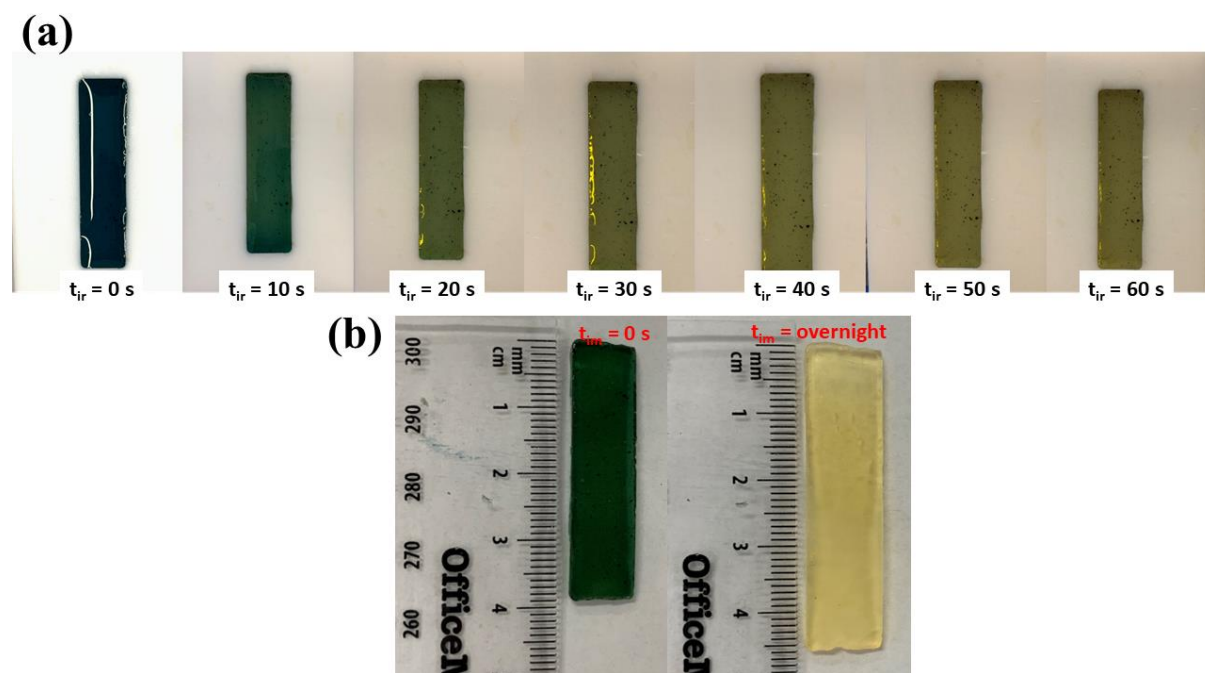


Figure S5.7. (a) Photobleaching of photopolymerization of PEGDA 700/water (80%/20%, wt) in presence of IDGCM/Iod (0.2%/2%, wt) upon exposure to LED@410 nm (110 mw cm^{-2}), recorded at different irradiation time (t_{ir}) and (b) photoinitiator leakage via immersion of cured rectangle at $t_{ir} = 10 \text{ s}$ in water (at immersion time, t_{im}). (25 mM NaOH)

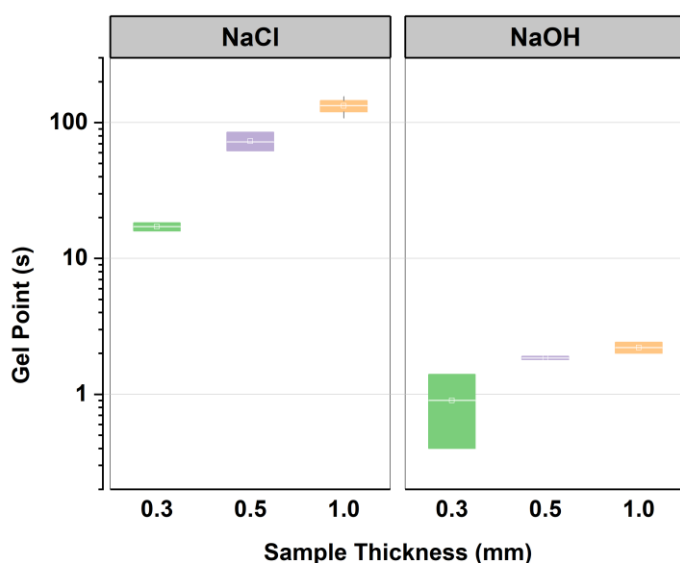


Figure S5.8. Gel points of the photopolymerization of the blend of PEGDA 700/water (80%/20%, wt) at diverse thicknesses in the presence of IDGCM/Iod (0.5%/2%, wt) upon the exposure of LED@410 nm (110 mW cm^{-2}). (25 mM NaCl or 25 mM NaOH)

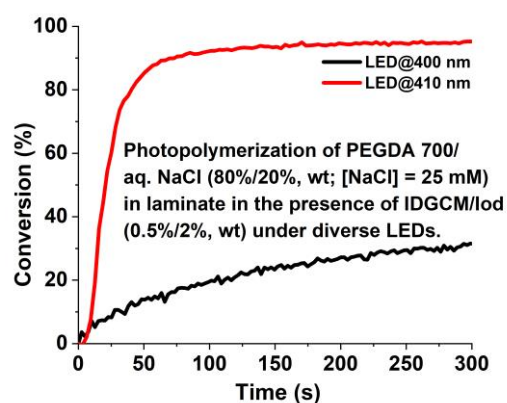


Figure S5.9. Photopolymerization profiles (double bond conversions vs time) of the PEGDA 700/water (80%/20%, wt) blend in laminate in the presence of IDGCM/Iod (0.5%/2%, wt) upon exposure to the LED@400 nm (6.4 mW cm⁻²) and LED@410 nm (110 mW cm⁻²). (25 mM NaCl)







Table S5.1. Summary of sample composition for 3D printing.

	Resin blend ¹		Photoinitiating system ²		
	PEGDA 700 (wt%)	DI water (wt%)	IDGCM (wt%)	Iod (wt%)	NaOH (mM)
Concentration	80	20	0.5	2	25

¹ Weight percentage (wt%) mixing ratios of PEGDA 700 and DI water used to formulate resin blend;

² The contents of the photoinitiating system were calculated in weight with respect to the resin blend.

Table S5.2. Cat coin (39 × 39 × 2 mm, L × W × H) print cured using the PEGDA 700/water (80%/20%, wt) in the presence of IDGCM/Iod (0.5%/2%, wt) and 25 mM NaOH under diverse settings.

Entry	Exposure time	Result	
		0.020 mm/layer	0.030 mm/layer
1	4.0 s		
2	2.5 s		
3	2.0 s		

Conclusions

In this thesis, , one literature review (Chapter 1) and four research chapters were included, and five natural dyes have been investigated as efficient photoinitiators for either hydrophobic or hydrophilic light-sensitive resins. Their photoinitiation abilities were well investigated, and further applications were presented.

Two natural flavone derivatives, morin and quercetin, were obtained from commercial vendors and investigated as effective photoinitiators for hydrophobic formulations in Chapter 2. In the presence of coinitiators (i.e., Iod, EDB, NPG) flavones demonstrated their versatilities under violet-blue light in diverse monomer systems, including free radical polymerization of Bis-GMA/TEGDMA blend and TMPTA, cationic polymerization of DVE-3, and thiol-ene polymerization of DVE-3/Trithiol and DVE-3/Trione blends. Generally, quercetin exhibited better photoinitiation performance compared to morin.

Upon the introduction of NaOH, the polyphenol compounds under investigation were transformed into salt form, resulting in an improvement in their water solubility. In Chapter 3, we investigated the use of citrus-extracted naringin as an excellent water-soluble photoinitiator with the assistance of NaOH. The concentration of NaOH was used to mediate the photopolymerization of the photocurable polymer, PEGDA 700, resulting in different mesh sizes of the cured polymer. This manipulation affected the swelling behavior of the resultant materials. Additionally, under mild light, 0.5 wt% naringin provided the best photopolymerization of PEGDA 700. Reasonable reduction of water content improved the photoinitiation ability of naringin, as long as the introduced naringin can be fully dissolved. With the optimization of 3D resins, naringin-involved formula achieved advanced applications. An actuator was successfully fabricated. With the help of the introduced conductive component (sodium acrylate) and an applied electric field, the 3D-printed actuator exhibited its actuation behavior. The transformation of the 3D printed hook-like actuator facilitates easing the storage shortage.

In Chapter 4, a similar result was observed. The pomegranate-extracted ellagic acid demonstrated its excellent water solubilities in the presence of NaOH and photoinitiation abilities in water-existed formulations under mild visible light irradiation. However, due to its dark appearance, 0.3 wt% rather than 0.5 wt% was the best concentration of ellagic acid for photopolymerization of PEGDA 700. The dark appearance of concentrated ellagic acid would prevent light penetration in gradient. With reduced concentration, the ellagic acid endowed the

resin with printability. A Gandalf figurine was successfully 3D printed with detailed facial texture. Meanwhile, a bilayer hydrogel (PEGDA 700 and PEGDA 575) was fabricated via a multi-material 3D printing technique in the presence of ellagic acid-based 3D resin. With the knowledge of mesh size manipulated swelling behavior, the 3D-printed bilayer hydrogel demonstrated curling behavior in a programmed direction. Thanks to the programmable behavior, a smart switch was produced specifically for an origami room. Once water leaks, the smart switch can automatically open or close depending on the installation direction.

Besides, an *Indigofera* extracted indigo carmine is a natural sodium salt. Considering its inherent ionic salt form, the amount of NaOH was considerably reduced in the formula of 3D resin due to common ion effect. As a result, a significantly reduced amount of NaOH (25 mM) was used in the indigo carmine-based 3D resin. Furthermore, the chain length of PEGDA was found to impact photopolymerization, with longer chain lengths resulting in higher functional group conversion of PEGDA. The optimized indigo carmine-based formula was used in 3D printing, resulting in the successful creation of a complex object with a well-defined surface texture. Indigo carmine's inherent dark blue color and excellent photobleaching property under blue irradiation allowed it to serve as both a photoinitiator and photoabsorber, resulting in high fidelity and precision in the 3D printing process. In addition, with the designed structure acquired via 3D printing with indigo carmine-involved 3D resin, 3D-2D reversible transformation was achieved upon water immersion and under airdrying.

The findings mentioned above have broadened the scope of efficient photoinitiators due to the abundant availability of natural dyes in nature. Natural photoinitiators are considerably more sustainable than synthetic ones. They hold substantial potential across diverse applications, particularly in biomedical or environmental protection fields. However, a few challenges remain to allow them applicable in industry. For instance, there is stability issue of them in 3D resins, and the employment of synthetic coinitiator (e.g., Iod) remains environmental problem during their synthesis process.

To address these issues, the following strategies could be considered. First, the development of a complex releasing photoinitiators upon a specific stimulus can improve the stability of photocurable resin even under daylight irradiation. Typically, without external stimulus, the photoinitiator could be stabilized by complex, and it could be activated by releasing itself from complex upon intentional stimulus. Second, the development of type I naturally derived photoinitiators could inherently resolve the pollution caused by the synthesis process of coinitiators. Specifically, type I photoinitiator works without coinitiators by homocleavage of chemical bond producing free radicals. For example, riboflavin in some contexts played the

role of one-component photoinitiating system.¹ Considering its low photoinitiation ability determining intense light to initiate polymerization, further development of type I natural photoinitiators still holds great promise. A deeper structural insight into the photoinitiation behavior of natural photoinitiators can assist the exploration and the development of type I natural photoinitiators. Another strategy is to develop natural coinitiators such as cyclic acetals. However, the developed cyclic acetals demonstrated limited photoinitiation efficacy with camphorquinone. Therefore, the improvement of cyclic acetals or the development of new natural coinitiators are beneficial for environmental concerns. Their natural existence ensures sustainability inherently. All those strategies can facilitate environmental sustainability, eventually achieving the overarching goal of fostering environmentally friendly and ecologically responsible practices in the fields of materials science and technology.

References

(1) Shin, D.; Hyun, J. Silk fibroin microneedles fabricated by digital light processing 3D printing. *J. Ind. Eng. Chem.* **2021**, *95*, 126-133.